Machine Learning Techniques for Autonomous Multi-Sensor Long-Range Environmental Perception System

Muhammad Abdul Haseeb

Universität Bremen 2020

Machine Learning Techniques for Autonomous Multi-Sensor Long-Range Environmental Perception System

Vom Fachbereich für Physik und Elektrotechnik
der Universität Bremen

zur Erlangung des akademischen Grades

Doktor–Ingenieur (Dr.-Ing.)

genehmigte Dissertation

von

M.Sc. Muhammad Abdul Haseeb

aus Pakistan

Referent:	Prof. Dr.-Ing. Axel Gräser
Korreferent:	Prof. Dr.-Ing. Udo Frese

Eingereicht am: 04.09.2020

Tag des Promotionskolloquiums: 28.01.2021

Acknowledgements

First of all, I would like to express my gratitude to my supervisor Prof. Dr.-Ing. Axel Gräser for offering me a Ph.D. position at the Institute of Automation (IAT) and for his valuable guidance, expert advice, and support throughout my research work. I would like to thank Prof. Dr.-Ing. Udo Frese for accepting to be the second reviewer of this thesis as well as Prof. Dr.-Ing. Alberto Garcia-Ortiz and Prof. Dr.-Ing. Walter Lang for accepting to be examiners of this thesis.

I would like to express my gratitude to my colleague Dr. Danijela Ristic-Durrant for extended discussions and valuable suggestions which have significantly contributed to the improvement of the thesis. Additionally, I would like to thank my former colleague Dr.-Ing. Maria Kyrarini for her encouragement and support.

Special thanks to the University of Nis partners for making the arrangments and obtaining the permits to perform experiments on the Serbian railway's sites, which helps to collect data for the thesis. My gratitude goes as well to all the participants in my experiments. I would like to thank Mr. Michael Ehlen for his technical support. I also thank all students who during the work on their Master Theses and Master Projects contributed to this thesis.

I am very thankful to the Postgraduate International Programme (PIP) of Physics and Electrical Engineering faculty at the University of Bremen for partially funding my participation in conferences.

I am deeply thankful to my parents, sister, and brother, for their love and unconditional support. I am forever grateful to my parents for giving me the opportunities and experiences that have made me who I am. Their encouragement made me pursue my destiny and explore new directions in life. I dedicate this milestone to them.

My thesis acknowledgement would be incomplete without thanking my wife Zarmeen for always being there for me, without her, this thesis would never have written and my baby-daughter, Ayra, whose smiling face always made me happy and inspired me. Having her midway during my Ph.D. was certainly not easy for me, but she has made my life wonderful, better, and more fulfilled than I could have ever imagined.

Abstract

An environment perception system is one of the most critical components of an automated vehicle, which is defined as a vehicle where the driver does not require to monitor the vehicle's behaviour and its surroundings during driving. This thesis addresses some of the main challenges in the development of vision-based environment perception methods for automated driving, focusing on railway vehicles. The thesis aims at developing methods for detecting obstacles on the rail tracks in front of a moving train to reduce the number of collisions between trains and various obstacles, thus increasing the safety of rail transport.

In the field of autonomous obstacle detection for automated driving, besides recognising the objects on the way, the crucial information for collision avoidance is estimated distances between the vehicle and the recognised objects (e.g. cars, pedestrians, cyclists). With the limited capabilities of current state-of-the-art sensor-based environment perception approaches, it is unrealistic to detect distant objects and estimates the distance to them. Mid-to-long-range obstacle detection system is one of the fundamental requirements for heavy vehicles such as railway vehicle or trucks, due to required long braking distance. However, this problem is unaddressed in the computer vision community. The emphasis of this thesis is on the development of robust and reliable algorithms for real-time vision-based mid-to-long-range obstacle detection. In this thesis, the algorithms for obstacle detection from single cameras were developed and evaluated on images captured from RGB, Thermal and Night-Vision camera.

The developed algorithms are based on advanced machine/deep learning techniques. The development of machine-learning-based algorithms was supported by a novel mid-to-long-range obstacle detection dataset for railways that is proposed in the thesis, which compiles of annotated images with the object class, bounding box, and ground truth distance to the object.

The developed novel methods for autonomous long-range obstacle detection, tracking and distance estimation for railways were evaluated on real-world images, which were recorded in different illumination and weather conditions by the obstacle detection system mounted on a static test-bed set-up on the straight rail track and as well on a moving train. Although the focus is on railways, the developed algorithms are also capable to use for road vehicles, hence evaluated on the images of road-scene captured by a camera mounted on moving cars.

Kurzfassung

Ein System zur Wahrnehmung der Umgebung ist eine der kritischsten Komponenten eines automatisierten Fahrzeugs, der Definition nach also eines Fahrzeugs, bei dem der Fahrer das Verhalten des Fahrzeugs und seiner Umgebung während der Fahrt nicht überwachen muss. Diese Arbeit befasst sich mit einigen der wichtigsten Herausforderungen in der Entwicklung sensorgestützter Methoden zur Umgebungswahrnehmung im Kontext automatisierten Fahrens, wobei der Schwerpunkt auf Schienenfahrzeugen liegt. Ziel der Arbeit ist die Entwicklung von Methoden zur Erkennung von Hindernissen auf den Gleisen vor einem fahrenden Zug, um die Anzahl der Kollisionen zwischen Zügen und verschiedenen Hindernissen zu reduzieren und damit die Sicherheit des Schienenverkehrs zu erhöhen.

Im Bereich der autonomen Hinderniserkennung für automatisiertes Fahren sind neben der Erkennung der Objekte auf der Straße die für die Kollisionsvermeidung entscheidenden Informationen die geschätzten Abstände zwischen dem Fahrzeug und den erkannten Objekten (z.B. Autos, Fußgänger, Radfahrer). Mit den begrenzten Möglichkeiten der heutigen sensorbasierten Umgebungswahrnehmung ist es unrealistisch, entfernte Objekte zu erkennen und den Abstand zu ihnen abzuschätzen. Das System zur Erkennung von Hindernissen im mittleren bis langen Bereich ist aufgrund des erforderlichen langen Bremsweges eine der grundlegenden Anforderungen an schwere Fahrzeuge wie Schienenfahrzeuge oder Lastwagen. Dieses Problem wird jedoch in der Computer-Vision-Gemeinschaft nicht angegangen. Der Schwerpunkt dieser Arbeit liegt in der Entwicklung echtzeitfähiger, robuster und zuverlässiger Algorithmen für eine bildbasierende Hinderniserkennung im mittleren bis langen Bereich. In dieser Arbeit werden die Algorithmen zur Hinderniserkennung von Einzelkameras entwickelt und anhand von Bildern, die von RGB-, Wärme- und Nachtsichtkameras aufgenommen wurden, bewertet.

Die entwickelten Algorithmen basieren auf fortgeschrittenen machine/deep learning Techniken. Die Entwicklung der auf maschinellem Lernen basierenden Algorithmen wurde durch einen neuartigen Datensatz zur Hinderniserkennung im mittleren bis langen Bereich für Eisenbahnen unterstützt, der in der Arbeit vorgeschlagen wurde und der aus annotierten Bildern mit der Objektklasse, der Bounding Box und dem Abstand zum Objekt zusammengestellt wurde.

Die entwickelten neuartigen Methoden zur autonomen weiträumigen Hinderniserkennung, -verfolgung und -abschätzung für Eisenbahnen wurden an realen Bildern evaluiert, die unter verschiedenen Beleuchtungs- und Witterungsbedingungen durch das Hinderniserkennungssystem auf einem statischen Prüfstandsaufbau auf der geraden Schiene und auch auf einem fahrenden Zug aufgenommen wurden. Obwohl der Schwerpunkt auf Eisenbahnen liegt, wurden die entwickelten Algorithmen auch auf den Bildern der Straßenszene ausgewertet, die von einer auf einem fahrenden Wagen montierten Kamera aufgenommen wurden.

Table of Contents

1. Introduction

Autonomous environment perception is one of the fundamental elements of automated vehicles as well as of many other autonomous indoor and outdoor applications such as mobile robots [1], assistive robots [2], and industrial robots [3]. The purpose of environment perception systems is to provide crucial information on the autonomous system surroundings, including potential obstacles, their velocities and locations, and even prediction of their future states. The collected information helps the automated vehicle in many ways, such as to avoid collision with obstacles, localisation, and navigation [4].

As research in the field of autonomous systems has matured in the previous decades, outstanding work has been seen in the advancements of the environment perception systems. Environment perception for automated vehicles typically combines multiple sensing technologies (i.e., LiDAR, radar, ultrasound, and visual) to detect obstacles and to provide their physical position in the environment. The fusion of multiple sensing technologies helps to overcome the drawbacks and limitations of one sensor by utilising the benefits of others [4].

Though the accuracy of the active sensing technologies such as LiDAR, RADAR, and ultrasound sensors is high, it is quite computational power consuming and expensive. On the other side, cameras are considered as the most functioning perception sensor which provides rich visual information of the surrounding, with every possible detail in it, in the form of images [5]. Cameras work in the same way as the human eye; help to detect and classify objects, understand the situation, and estimate the depth. However, the depth estimation is a critical task using cameras. Stereo-vision is the most common approach to estimate depth. The images taken by two cameras are used to triangulate and estimate distances [6].

Although stereo-vision systems work well in many applications, they are fundamentally limited by the baseline, which is the distance between the two stereo cameras. The stereo-vision based depth estimates tend to be inaccurate when the distances measured are large as the baseline is long. The reason behind the inaccurate measurement for longer distance is that even very minor errors in triangulation estimation cause very large errors in distance measurement [7]. Additionally, stereo-vision tends to fail for textureless regions of images, in which it is difficult to find the corresponding regions reliably [8].

Monocular cameras-based vision detection systems have been proposed to overcome the limitations of stereo-vision. As traditional monocular vision is unable to provide accurate and robust distance measurement, most of the methods are machine learning-based solutions [9]. These monocular cameras based object detection approaches rely on the dataset with ground truth collected via LiDAR or stereo-vision [10].

1.1 Problem statement

Many approaches for autonomous environmental perception have been presented for different application fields and scenarios. Whereas other transport modes have been quick to automate certain operations, the rail runs the risk of lagging behind. One of the critical challenges, which has so far hindered the automation of rail systems, is the lack of a safe and reliable onboard obstacle detection system for trains within existing infrastructure [11]. In recent years, there is a tendency to use experience from obstacle detection both in the automotive and the aviation sector for the development of autonomous obstacle detection in railways [12] [13]. While the main principle of obstacle detection in front of a vehicle from the automotive sector can be applied to railway applications, there are also specific challenges. Since this topic is not much explored, there are countless challenges, and one of the primary challenges is Long-Range Obstacle Detection.

Long-range obstacle detection: Sensor technology in current land transport research can look some 200 m ahead [14]. The required rail obstacle detection interfacing with loco control should be able to look ahead up to 1000 m detecting objects on and near track which may potentially interfere with the clearance and ground profile. The trains are running with high speed due to which and the train size and weight, the braking distance is much longer than for road vehicles. Therefore, a long-range obstacle detection system for railway vehicles is crucial. It is a very challenging task to detect objects in real-time which are at far distance and project in a couple of pixels on an image plane [15].

1.2 Thesis Contributions

The focus of this thesis is on long-range autonomous environmental perception. Therefore the novel algorithms for object detection, distance estimation, multiple object tracking, and sensor fusion are presented. The long-range perception is required and needed in many areas such as long-range obstacle detection system for autonomous trains or other heavy vehicles. The methods for long-range obstacle detection presented in this thesis are developed with the main goal of providing a solution to railways. However, the same methods can be used for self-driving cars as well; hence the evaluation of the developed was also performed on images of road scenes taken from a camera mounted on a moving passenger car.

The developed methods for railway scenarios were evaluated on the images taken by cameras of a prototype autonomous Obstacle Detection System (ODS) developed within the H2020 Shift2Rail project SMART-Smart Automation of Rail Transport [11] [16].

The major contributions of this thesis are listed below:

1. *Long-range object detection and distance estimation dataset (LRODD)*
   There are object detection datasets available that contain labeled objects and distance information however the size of objects in images is relatively large due to the ground truth distance up to nearly 150 meters. There are no datasets available which provide annotated bounding boxes of distant objects at more than 150 meters with the ground truth distance information which indeed required to build long-range obstacle detection system. A novel dataset for long-range object detection is presented in this thesis. The dataset is built on the images acquired from three RGB cameras set up at different zooming factors to cover short, mid to long-distance range, a thermal camera, a night vision camera, a LiDAR sensor for short-range ground truth distance measurement, and a GPS (Global Positioning System) sensor for positioning.

The dataset contains the images of rail scenes that occurred during the data recording experiments taking place in the lifetime of H2020 Shift2Rail Project SMART. Although containing images of rail scenes, the dataset can be used in many other applications for long-range obstacle detection, distance estimation, and tracking, such as automotive and robotics applications. The dataset ranges from 0 to 1000 meters and contains several object classes.

2. *A single camera-based distance estimation to a detected object in an image (DisNet)*

   Distance estimation to the detected object using a vision sensor either with the monocular camera or stereo cameras is one of the critical tasks in computer vision. In this thesis, a novel method for long-range distance estimation using a single camera is presented. The proposed method is able to work with any type of monocular camera, such as thermal or RGB camera, and can estimate the distance to the object from short to long-range depending on the resolution of the image. The method can be used in various applications where distance estimation is required for short to long-range using a monocular camera. Moreover, the method does not require any prior calibration of the camera.

3. *Distant object detection and distance estimation (YOLO-D)*

   Current state-of-the-art object detection methods are designed to localise and classify the objects in an image. However, they do not estimate object distance. In this thesis, the existing state-of-the-art machine learning-based method YOLO (You Only Look Once) for object detection was modified to estimate the distance to the detected objects and so-called end-to-end learning was enabled.

4. *Sensor fusion of multiple cameras for distance estimation (Multi-DisNet)*

   A novel machine learning-based sensor fusion method for distance estimation is presented in this thesis. The method based on the fusion of object detection results from thermal and RGB camera estimates the distance to the detected object. The method helps to provide reliable distance estimation to the obstacle in adverse weather and illumination condition or in the case where one of the sensors fails to detect the object.

5. *Multiple object tracking (DisNet-RNN Tracker)*

A machine learning-based method for multiple object tracking is also investigated in the thesis as a method for improving reliability of object detection and distance estimation. The method helps to track objects in cases where the object detection module fails to detect or produces unreliable object detection. It further helps to estimate the distance to the undetected object based on the tracked information.

6. *Evaluation of developed algorithms in real-world scenarios*
   The machine learning based algorithms developed in this thesis were tested on real-world scenarios in railways. The algorithms were developed to meet the requirements of real-time performance.

1.3 Thesis Overview

This thesis is organized in the following chapters:

- Chapter 2 introduces the application of machine learning in computer vision. As first, an introduction to machine learning is given, following with the state-of-the-art machine learning-based computer vision algorithms and their applications.
- Chapter 3 describes the novel dataset for long-range object detection and distance estimation LRODD.
- Chapter 4 presents the two novel machine learning-based methods for distance estimation using a single camera, namely DisNet and YOLO-D. The performance evaluation of each method is presented within the chapter.
- Chapter 5 describes the machine learning-based sensor-fusion method for distance estimation from multiple cameras Multi-DisNet. The evaluation results are discussed in the chapter.
- Chapter 6 presents the methods for multiple objects tracking DisNet-RNN Tracker and the results achieved.
- Chapter 7 presents the real-time implementation and requirements analysis of developed methods.
- Chapter 8 summarises the conclusions from all the chapters and discusses the outlook.

2. Machine learning-based environmental perception for autonomous systems

The main aim of this chapter is to provide the necessary theoretical background of machine learning, its application in the field of computer vision and datasets to support the proposed methods described in the following chapters. Therefore, an introduction to machine learning and datasets is given followed by state-of-the-art particularly in vision-based object recognition, distance estimation, and object tracking.

2.1 Machine learning techniques

Computer Vision is defined as a field of study about how computers see and understand the content of digital images. Computer vision aims to develop methods that imitate human visual perception. With the great evolvement in the field of computer vision in the last couple of decades, still many problems remain unsolved. The main reason is due to the limited understanding of human vision and the human brain [17].

However, integration of machine learning and deep learning in computer vision brought significant advancement in high-level problems such as text understanding [18], 3D model building (photogrammetry) [19], medical imaging [20], human-computer interaction [21], automotive safety [22], surveillance [23], fingerprint recognition and biometrics [24], and others.

Machine learning (ML) is a subgroup of Artificial intelligence (AI). In the last few decades, several fields were revolutionized within the ML. Neural Network (NN) is a sub-field of ML, and Deep Learning (DL) lies within the NN [25]. Similar to machine learning algorithms, deep learning methods can also be classified as follows: supervised, semi-supervised, or partially supervised, and unsupervised. Additionally, there is another learning approach category called Reinforcement Learning (RL) or Deep RL (DRL) that is often discussed under semi-supervised or sometimes unsupervised approaches to learning [26].

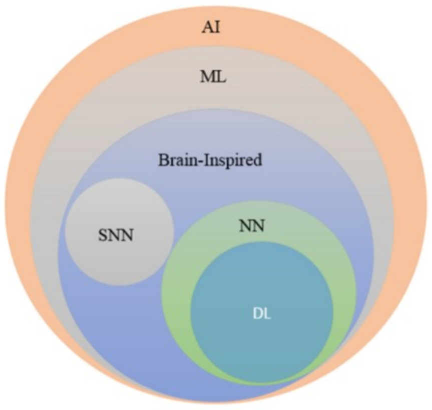

Figure 1. The grouping of AI and its sub-groups [25]

2.1.1 Supervised Learning

Supervised learning is a method of learning that use labelled data. In the case of supervised approaches, the environment has a set of inputs and corresponding outputs (x_i, y_i). For example, if for input x_u, the agent predicts $y_u^{/}= f(x_u),$ the agent will receive a loss value $L(y_u, y_u^{/})$. The agent will modify the network parameters iteratively until it achieved a better estimate of the desired outputs. After training, the agent will be able to predict the output close to the desired output on the given set of input from the environment [27].

Some popular supervised machine learning algorithms are linear regression for regression problems, random forest for classification and regression problems, Support vector machines (SVM) for classification problems. Likewise, several supervised learning approaches are involved in deep learning, including Deep Neural Networks (DNN), Convolutional Neural Networks (CNN), Recurrent Neural Networks (RNN), containing Long Short Term Memory (LSTM), and Gated Recurrent Units (GRU) [25].

Supervised learning can be split into two main types, that are classification and regression. Classification is used when the required output is categorical for example sorting of email into “spam” or “non-spam” class, diagnosis of a disease based on observation of the patient such as sex, blood pressure, or certain symptoms. On the other hand, regression is used when the output is continuous value; for example, the prediction of stock based on observation [28].

2.1.2 Unsupervised learning

The unsupervised learning method is based on unlabeled data. The data without the presence of labels is known as unlabeled data. In this case, the machine learning model understands the internal representation, pattern, or features to determine unknown relationships or mapping within the given unlabeled input data. Typically, clustering, generative, and dimensional reduction techniques come into unsupervised learning approaches. Most popular unsupervised machine learning algorithms are K-means for clustering and Apriori algorithm for association rule learning problems [29]. Generative Adversarial Networks (GAN), RNNs such as LSTM and RL are used for unsupervised deep learning methods as well [25].

Similar to supervised learning, unsupervised learning is also classified as two main types which are Clustering and Association. Clustering is used when it is needed to organise or group data based on similarities between them, for example, grouping customers based on their purchasing behaviour or interests. Whereas Association is used to correlate or find relations between variables in the data, for example, you find the rule if a person buys X also tend to buy Y.

2.1.3 Semi-supervised learning

Semi-supervised learning is another learning method that uses partially labelled datasets. Typically in this learning technique, a small labelled data together with large unlabeled data are used in training. Deep Reinforcement Learning (DRL) and Generative Adversarial Networks (GAN), RNN, including LSTM and GRU, are also used with semi-supervised learning [30].

2.1.4 Reinforcement learning

Reinforcement learning is another type of Machine Learning, where an agent learns how to act in a situation by performing actions and observing the results. The main idea behind RL is that an agent learns from the environment by interacting with it and by receiving rewards for the taken actions. For the right results, the positive reward is given to the action and similarly a negative reward in case of bad results. In this way, an agent learns the sequence of actions to be taken by interacting with the environment [25].

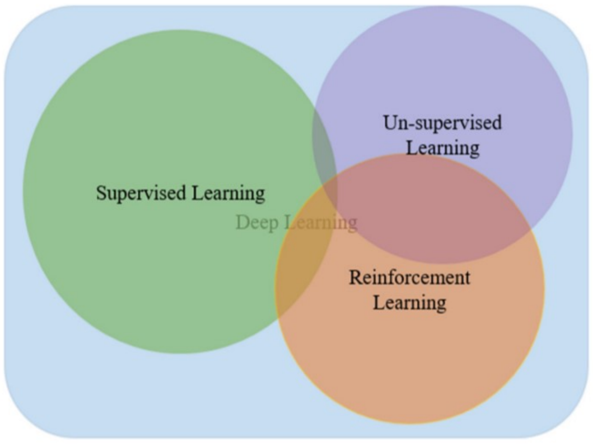

Figure 2. Category of Deep Learning approaches [25]

2.2 Artificial neural networks

As explained earlier Machine Learning is a super-set of Deep Learning. The main idea of deep learning was inspired by Artificial Neural Networks abbreviated as ANN, often called Neural Networks (NN). Firstly, it is essential to explain ANN and some important facts that described deep learning techniques. The ANN is inspired by human biological neural networks [31]. Figure 3 shows the basic NN architecture.

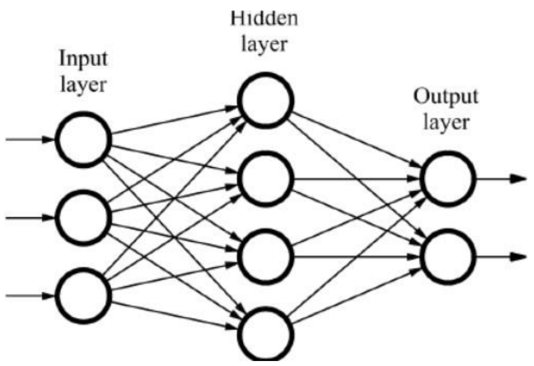

Figure 3. A basic artificial neural network architecture

Usually, the architecture of NN always consists of an input layer, hidden layers, and an output layer. It is also called as *Multi-Layer Perceptron (MLP)* [17]. The *input layer* is the very first layer of artificial neurons that bring the data into a network for further processing by subsequent frames; the input data can be pixels of the image or any computed feature. The *hidden layers* are layers between input and output layers where artificial neurons take weighted input and produce output through an activation function. The weights of artificial neurons are learned during the training process, whereas activation function defines the output of the neuron. The *output layer* is the final layer of NN that outputs the prediction result based on the input data feed into the neural network.

Briefly, the Neural Network can be defined as an approximation function of the any given problem in which learn parameters (*weights*) in hidden layers multiply with input and predict output close to desired output [28].

The basic computation unit in the neural network is known as a *neuron*, often called a node, perceptron, or unit, as shown in Figure 4. It receives input from previous nodes, or an external source, and computes output. Based on the relative importance of input to other inputs, each input is associated with a weight (w). The neuron determines a weighted sum of all its inputs. An additional parameter *Bias* is added to the weighted sum is a constant value which helps the model in a way that it can fit best for the given data. Further, it produces output by applying a function *g* on it, which is also known as *activation function* [32].

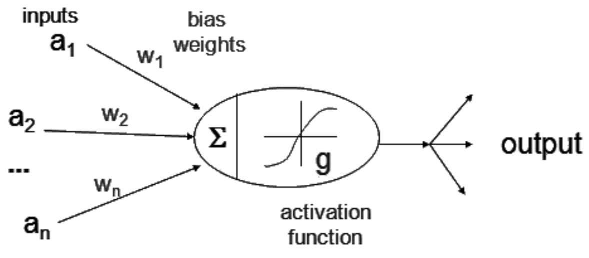

Figure 4. The architecture of basic computational unit in ANN

$$y = g\left(b + \sum_{i=1}^{n} w_i a_i\right) \tag{2-1}$$

2.2.1 Activation Function

The purpose of the activation function is to learn complex non-linear representations of data and introduce non-linearity into the output of the neuron. The neural network without an activation function would be a simple linear regression model with less power to learn complex nonlinear problems. Another essential characteristic of the activation function is that it should be differentiable. It is required to be differentiable so as to compute gradients of Error (Loss) with respect to weights while performing backpropagation optimisation to fine-tune the weights using optimisation techniques to reduce error. There are many activation functions, but the most popular one is sigmoid or logistic, Tanh - hyperbolic tangent, softmax, ReLu (Rectified Linear Unit), or identity functions [26].

- Sigmoid: Take an actual input and squash between 0 and 1.

$$\sigma(x) = \frac{1}{1+e^{-x}} \tag{2-2}$$

- Tanh — Hyperbolic tangent: it limits the output between -1 and 1

$$\tanh(x) = \frac{e^{x} - e^{-x}}{e^{x} + e^{-x}} \tag{2-3}$$

- ReLu -Rectified linear units: The formula is deceptively simple: max(0,x).

$$\mathrm{R}(x) = \begin{cases} x, & x > 0 \\ 0, & x \leq 0 \end{cases} \tag{2-4}$$

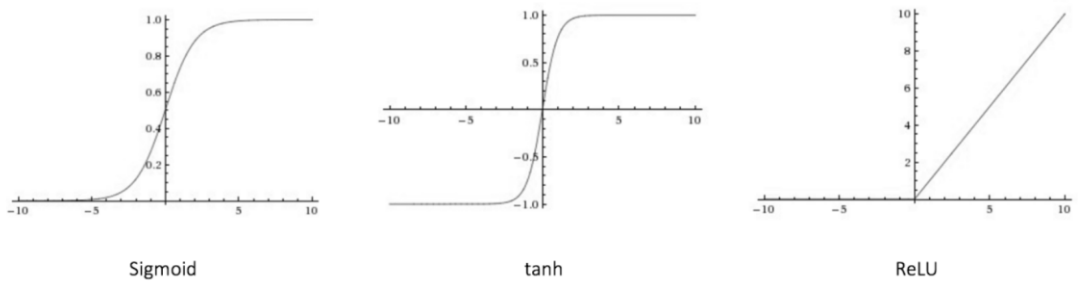

Figure 5. Three most common activation functions [33]

2.2.2 Training

In this section, the training process of NN will be explained. However, some important factors need to be described for training processes such as dataset, loss function, and optimisation techniques. The newly created neural network is like new-born babies: with their exposure, mistakes, and experiences, they learn new things. Similarly, NNs during the training phase learn something new through given data and improve the performance by their own mistakes *(Error)*. The knowledge of neural networks is captured in the form of parameters i.e. weights and bias. The input data propagate from the input layer via hidden layers to the final prediction layer. The prediction layer makes decision-based on a given input. At the beginning of the training phase, often the decision made by NN is wrong because the parameters through which data propagate are not optimally adjusted. Typically training process composed of multiple iterations or also known as epochs until the NN learns correctly and predicts output close to the desired output. For each epoch, the error is measured which is defined as *Loss function* and parameters of NN are adjusted in a way to reduce the error to make predictions close to the desired output. The error *J(w)* is the function of NN internal parameters, i.e. weights and bias. If the parameters change, the error changes as well [30] [25].

2.2.3 Optimisation algorithm

The parameters are adjusted using optimisation algorithms. A neural network propagates data from the input layer towards the output layer known as forward propagation. However, the changing of parameters is done in reverse order. During the parameter adjustments, the network back propagates to optimise parameters. The optimisation algorithms help to find the minimum of a loss function and adjust parameters accordingly.

$$\mathrm{w}^{k+1} = \mathrm{w}^{k} - \frac{\partial}{\partial w^{k}} J(w) \tag{2-5}$$

Usually, optimization functions measure the gradient, i.e. the partial derivative of the loss function with respect to weight, weights are adjusted in the opposite direction of the measured gradient. This process is repeated until a loss function minimizes [34].

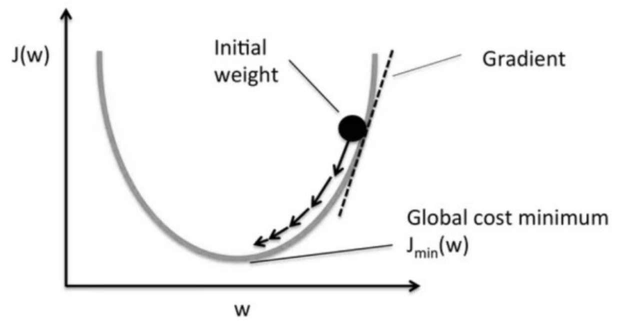

Figure 6. Gradient Descent [35]

2.2.4 Regularisation

The best choice of the number of training epochs cannot be measured, and with the inappropriate training epochs, the NN can lead to overfitting or underfitting problems.

The under the fitted model is neither performs on training data nor on new data. Whereas the overfitted model performs well on training data but not on evaluation data due to over learning of training data.

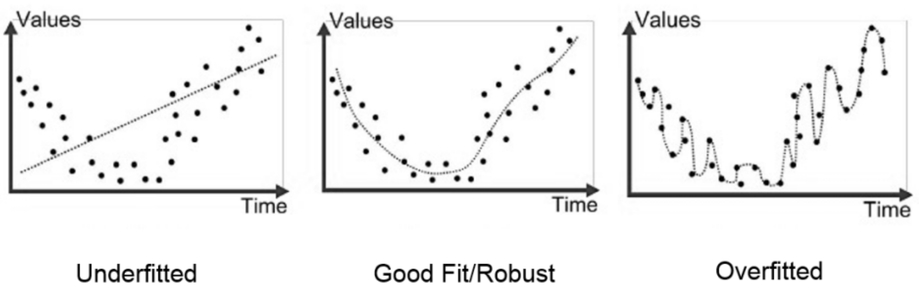

Figure 7. Regularisation [36]

Another important technique that needs to be highlighted is early-stopping. Early stopping is one of the classical regularization techniques used in the training process to stop the training once the model performance stops improving or in other words, loss function stops converging [28].

2.2.5 Error and Loss function

most commonly in many learning networks, the error is calculated as the difference between the desired output and the predicted output. The function that calculates error is known as loss function $l(w)$, often named as the objective function.

$$l(w) = y - \hat{y} \tag{2-6}$$

There is no single loss function that works with data of any kind. This depends on the factors including the existence of outliers, choice of the machine learning algorithm, gradient descent time efficiency, ease of finding derivatives, and prediction confidence. Loss functions can be categorized into two main types: Classification and Regression Loss. The regression model predicts the quantity while the classification model predicts the probability of class label.

- ***Classification loss functions*:** Log loss, Focal loss, Kullback–Leibler (KL) Divergence/ Relative Entropy, Exponential Loss, Hinge Loss.
- ***Regression loss functions*:** Mean Square Error/Quadratic Loss (L2), Mean Absolute Error (LI), Huber Loss/Smooth Mean Absolute Error, Log cosh loss, Quantile loss.

Below two very popular regression loss functions are described.

Mean Absolute Error (MAE) – L1 Loss: Another loss function used for regression models is Mean Absolute Error. It is defined as the sum of the absolute differences between our target and the variables predicted.

$$MAE = \frac{\sum_{i=1}^{n} |y_i - \widehat{y_i}|}{n} \tag{2-7}$$

Mean Square Error – L2 Loss: Mean Square Error is the most widely used regression loss function. It is defined as the total sum of squared distances between our target variable and predicted values.

$$MSE = \frac{\sum_{i=1}^{n} (y_i - \widehat{y_i})^2}{n} \tag{2-8}$$

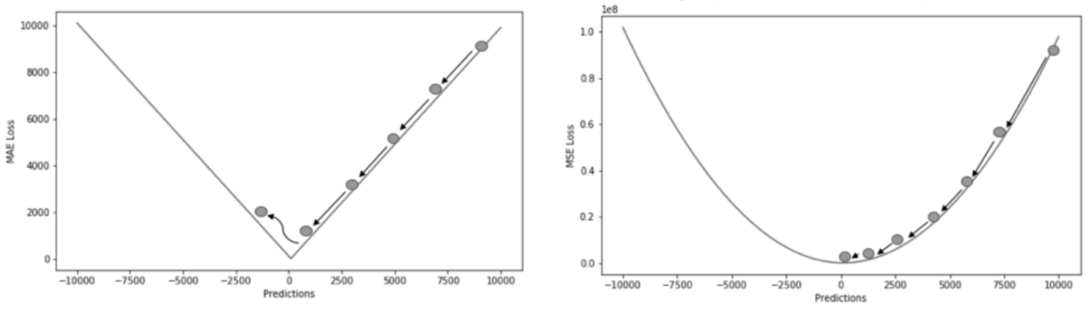

Figure 8. A plot of MAE and MSE Loss (Y-axis) vs Predictions (X-axis)

Both the MAE and MSE loss functions reach the minima when the predicted value exactly equal to the desired value. The selection of loss function depends on the task. The MSE is easier to solve to find gradients thus converge faster to minima. On the other side, MAE is more robust to outliers but more complicated to solve due to not continuous derivatives.

2.2.6 Hyperparameter

The components of a neural network model, i.e. the activation function, loss function, and optimisation algorithm play a crucial role in the effective and efficient training of a model and delivers accurate results. Specific tasks require a different set of such functions to deliver the best results possible. All of these components of the neural network, also known as hyperparameters.

The hyperparameters are set of variables that determine the network structure such as number of hidden layers, number of neurons, and the variables which determine in what way the network is trained such as weight initialisation, batch size, number of epochs, learning rate, activation function.

There is no pre-defined or specific way to select the hyperparameters for the construction and training of a neural network. The most common practice of tuning of hyperparameters or optimisation of hyperparameters to find the best configuration of parameters is the manual search method. There are hyperparameters selection methods such as RandomSearch [37] and GridSearch [38] which find the best parameters from the given set of parameters. Both methods are very similar; the best parameters are selected based on the training of network with all possible combinations of parameters. This method is suitable for simple models which take less time to train, but if the model takes longer time, almost all deep learning networks or the search space is big, this approach could not be the best option.

2.2.7 Training, testing and validation set

Usually, the labelled dataset is split into three sets training, validation, and test. The training set on which the model find optimal values of weights to fit the given set. The validation set is used during the training process to find optimal hyperparameters of neural networks, such as the number of hidden layers, stopping point of training, and others. The test set is used to estimate the performance of the final trained model. The test set does not have any impact on the training of the neural network. The splitting of the dataset depends on the size of the dataset. Most commonly, the dataset spits into 80% for the training set, 10% for validation, and 10% for testing [25] [26].

2.3 Deep Neural Networks

The procedure and techniques of feature extraction and learning are the key difference between traditional machine learning and deep learning [39]. Traditional machine learning used handcrafted engineering, several feature extraction methods extract features, and then the extracted features are provided to the learning model to predict the output. Additionally, often several pre-processing algorithms are involved in traditional machine learning. Whereas in deep learning, DL itself extract and learn features from raw data. DL minimises the human effort by extracting the features itself. Features are represented hierarchically in the multi-layer network. Similar to human brain biological neural networks, deep learning contains layered architecture where high-level features are extracted from the last layers, and low-level features are extracted by first layers. Table 1 shows the different learning methods based on the features with different learning steps [25].

Table 1. Different feature learning approaches

Approaches	**Learning Steps**				
Rule-based	Input	Hand-design features	Output		
Traditional Machine Learning	Input	Hand-design features	Mapping from features	Output	
Representation Learning	Input	Features	Mapping from features	Output	
Deep Learning	Input	Simple features	Complex Features	Mapping from features	Output

A basic structure of deep neural networks is the traditional ANN network with multiple hidden layers. The 'shallow' neural network has only one hidden layer is opposed to deep neural network contains more than one hidden layer, often of several types. There are many deep learning methods rooted in the initial ANNs, including supervised (DBNs, RNNs, CNNs), unsupervised (AE, DBNs, RBMs, GAN), semi-supervised (often GAN) and DRL. The deep neural networks learning techniques are similar to neural networks. However, some advancement is also made in the learning process to fasten the learning process of a large number of parameters.

Another significant difference between traditional ML and DL is the performance of ML and DL with respect to the amount of data. The study [40] shows that the ML approaches show better performance for a lesser amount of data. Whereas the amount of data increases beyond certain limits, the performance of ML does not show further improvements and becomes steady. on the other side, the performance of DL approaches increases with respect to the increase in the data value [41].

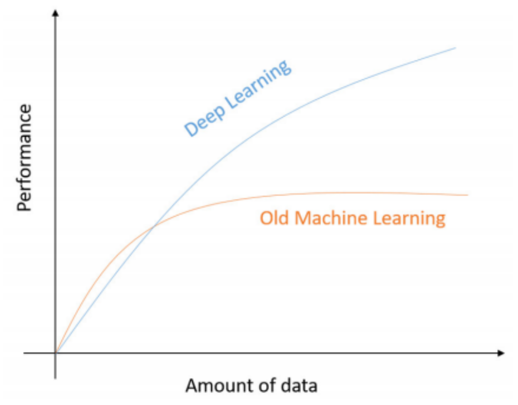

Figure 9. The deep learning efficiency with regard to the amount of data

2.3.1 Deep Learning for Computer vision

The deep learning often refers to universal learning because it can be used and applied in many application domains. With the many success stories of deep learning in almost every field, one of the well-known and evident applications of deep learning is in Computer Vision (CV). The DNN is widely used in CV and has excellent capabilities such as in image pattern recognition [39]. Convolution Neural Network (CNN) is the type of DNN most commonly applied in computer vision to analysing images in a similar way as human visual sense does. The first Convolution Neural Network (CNN) was introduced in 1988 however; it was not so popular back then due to limited sources of computational power to process and train the CNN network. In the 1990s, the authors [42] achieved excellent results for handwritten digits classification problems using a gradient-based learning algorithm to CNNs. After that, the drastic change has been noticed in the 2000s after the revolution of high-performance processing components such as GPUs [43] and computer platforms such as Nvidia Drive [44] that were explicitly designed to work for convolutional network and to work with high-dimensional data [43].

Mostly computer vision problems are surrounded by CNN architectures. Convolutional Neural Network (CNN) is a type of Deep Neural Networks (DNN) and is commonly used for image classification and segmentation. A convolutional neural network (CNN) is made up of an input layer, output layer as well as multiple hidden layers. In contrast, hidden layers are typically comprised of convolutional layers, pooling layers, and fully connected layers.

The main function of the convolutional layer is to extract the features from the input image or the previous layer, by using a fixed-sized convolutional kernel to do the convolution operation with the input in the form of sliding window, as shown in Figure 10 [45].

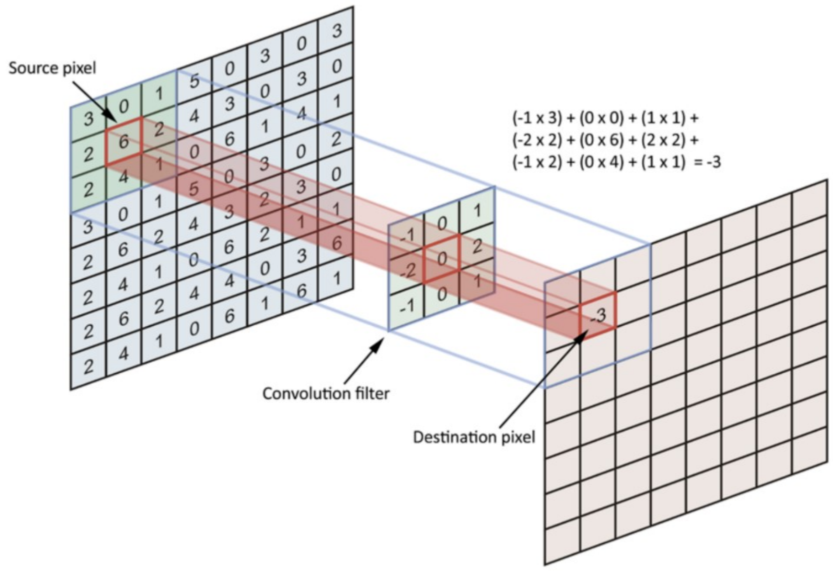
Source pixel
(-1 x 3) + (0 x 0) + (1 x 1) +
(-2 x 2) + (0 x 6) + (2 x 2) +
(-1 x 2) + (0 x 4) + (1 x 1) = -3
Convolution filter
Destination pixel

Figure 10. Example of convolution operation [46]

Each convolutional layer is made up of many feature maps, and each feature map is the convolution output between the current kernel and the feature maps of the former layer. The calculation of the convolutional layer can be represented as the following formula (2-9):

$$y_j^l = f(\sum_{i \epsilon M_j} y_i^{l-1} \otimes k_{ij}^l + b_j^l) \qquad (2\text{-}9)$$

Where k_{ij}^l is the convolutional kernel between the *i*-th feature map of the *l*-th layer and the *j*-th feature map of the *l*-th layer, M_j is one example of the input feature map, b_j^l is the bias of the *j*-th feature map of the *l*-th layer, and *f*() is the activation function, including Sigmoid, Tanh, ReLU(Rectified Linear Unit) function, etc.

Then, the pooling layer would reduce the dimensionality of each feature map from the forward layer while keeping valuable information [47]. There are mainly two kinds of pooling layer, max-pooling layer, and average-pooling layer. As the name implies, the max-pooling layer selects the most significant number of each given feature map, while the average-pooling layer takes the average number. After that, the fully connected layer transforms the feature map matrix of the previous layer into the form

of vector. Finally, the output layer outputs the class by using an activation function, which includes softmax regression or logistic regression, and classifies the images.
One of the toughest computer-vision problems encounter by CNN is object recognition. Object recognition is a task to classify the objects in an image into known objects labels. The revolutionary results have been seen in ImageNet-2012 Large Scale Visual Recognition Challenge (LSVRC) when DL networks outperformed the human accuracy of object recognition. ImageNet- LSVRC is a yearly competition focused on image classification. Various state-of-the-art CNN based object recognition methods including AlexNet [48], Clarifia [49], VGG-16 [50], GoogLeNet19 [51] and ResNet152 [52] were tested on ImageNet [53] dataset. Figure x shows the improvement of DL techniques overtime in ImageNet challenges since 2012. The ResNet152 has achieved a 3.57% error rate as opposed to humans with an error rate of 5%.

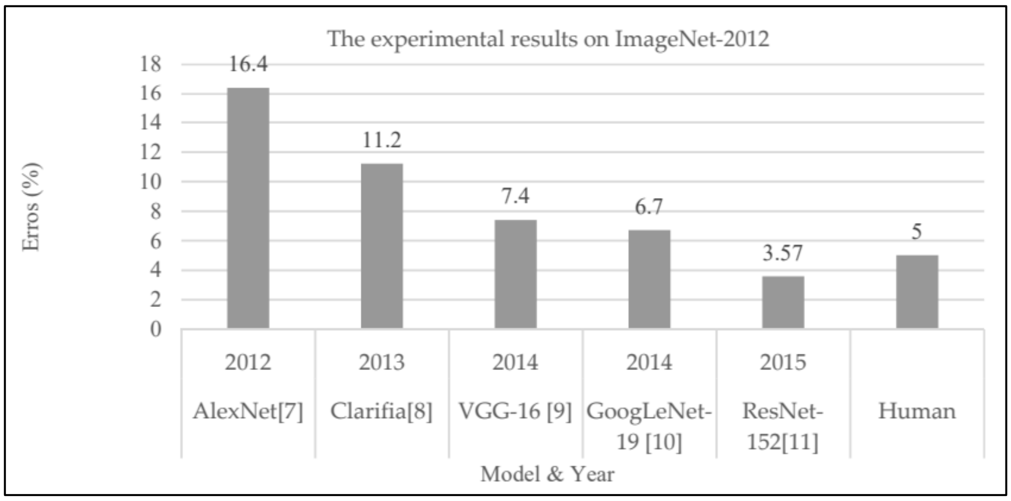

Figure 11. Accuracy of different DL models on ImageNet classification challenge [25]

The AlexNet recognised as one of the first deep networks that showed significant accuracy in ImageNet competition. It is designed by the SuperVision group from the University of Toronto. AlexNet consists of five convolutional layers followed by three fully connected layers much larger than the previously used CNN network LeNet [42] for computer vision tasks. The uniqueness of AlexNet architecture is that it uses the ReLu activation function instead of the tanh to add non-linearity, which also accelerates the speed of the training process by six times and improves accuracy. Further, it overlaps pooling layers to reduce the size of the network. Another problem this network solved was reducing the over-fitting by using dropout layers after every

FC layer. It has 60 million parameters and 650,000 neurons. In 2012 with limited hardware capabilities, it took 5 to 6 days to train Alexnet on two GTX 580 3GB GPUs.

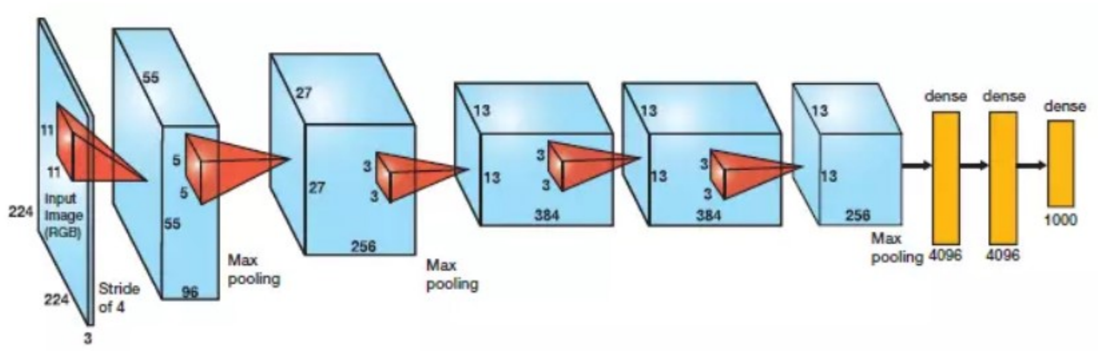

Figure 12. AlexNet architecture [54]

After the success of AlexNet, many models were proposed, and dramatically the performance of object recognition has been improved over time. Some of the state-of-the-art models for classification, segmentation, and detection task are listed as follows:

2.3.1.1. Classification

The input images are encoded in different steps with convolution and sub-sampling layers according to the classification models architecture, and eventually, the SoftMax method is used to determine class likelihood. Such models with a classification layer can, however, be used for segmentation and detection tasks as feature extraction. The list of some classification models are as follows: AlexNet [48], VGGNet [50] , GoogleNet [51], ResNet [52], DenseNet [55], FractalNet [56], CapsuleNet [57], IRCNN [58] , IRRCNN [59], DCRN [60] and so on. These classification models also refer to base feature extractors due to their role in object detection and object segmentation.

2.3.1.2. Segmentation

Several semantic segmentation models proposed during the last few years. The segmentation model is composed of two units: encoding and decoding. In the encoding unit, the convolution and subsampling operations are carried out to encrypt the latent space in the lower dimensions whereas the decoding unit decodes the image from latent space conducting deconvolution and upsampling process [25]. Fully

Convolutional Network (FCN) is the very first form of segmentation [61]. Later the improved version of this network which is called SegNet is introduced [62]. Recently, several new models have been introduced which include RefineNet [63], PSPNEt [64], and DeepLab [65].

2.3.1.3. Detection

The topic of detection is a bit different compared with classification and segmentation problems. The purpose of the model is to classify target categories with their respective positions. The model answers two questions: What is the object (classification problem)? and where the object (regression problem)? To achieve these goals, two losses are calculated for classification and regression unit at the top of the feature extraction module, and the model weights are updated with respect to both losses. For the very first time, Region-based CNN (RCNN) is proposed for object detection task [66]. Recently, there are some improved solutions to detection have been suggested, including focal loss for dense object detector [67] better detection approaches have been proposed, Later the different improved version of this network is proposed called fast RCNN [68]. mask R-CNN [69], You only look once (YOLO) [70] and SSD: Single Shot MultiBox Detector [71]. All these detection models use classification models as their base to make feature extraction.

In addition, the classical methods can be found back in the 1960s, and later, some of the widely used methods are Haar-like features [72], SIFT [73], SURF [74], GLOH [75] and HOG detectors [76].

2.3.2 You Only Look Once (YOLO)

In this section, YOLO object detection model is discussed to support the implementation and modifications in the next chapters.

Up till 2015, object detection systems were re-purposing existing classifiers to perform detection. This meant the use of a sliding window technique in looking at specific regions of the image one by one and making predictions accordingly based on that region. YOLO (You Only Look Once) identifies object detection as a regression problem, thereby spatially separating bounding boxes and their associated class probabilities. YOLO uses a single neural network to detect multiple objects directly from an RGB camera image and predict its bounding boxes with associated class probabilities [70]. Up to now, there are three YOLO version available: YOLO [70], YOLOv2 [77] and YOLOv3 [78]

2.3.2.1 YOLO

YOLO aims to perform object detection in real-time. Therefore, it does not use the sliding window technique traversing over the image region by region. Instead, it looks at the entire image once during training and testing to formulate contextual information about object appearance and class. This makes YOLO much faster than other detection algorithms. Competing detection algorithms of the time like Fast R-CNN [79] had better accuracy when compared to YOLO but was considerably slower with much more background noise [70].

YOLO is a CNN which uses 24 convolutional layers and two FC (fully connected) layers. The convolutional layers extract feature maps from the image and the two FC layers regress the network for bounding box parameters and class.

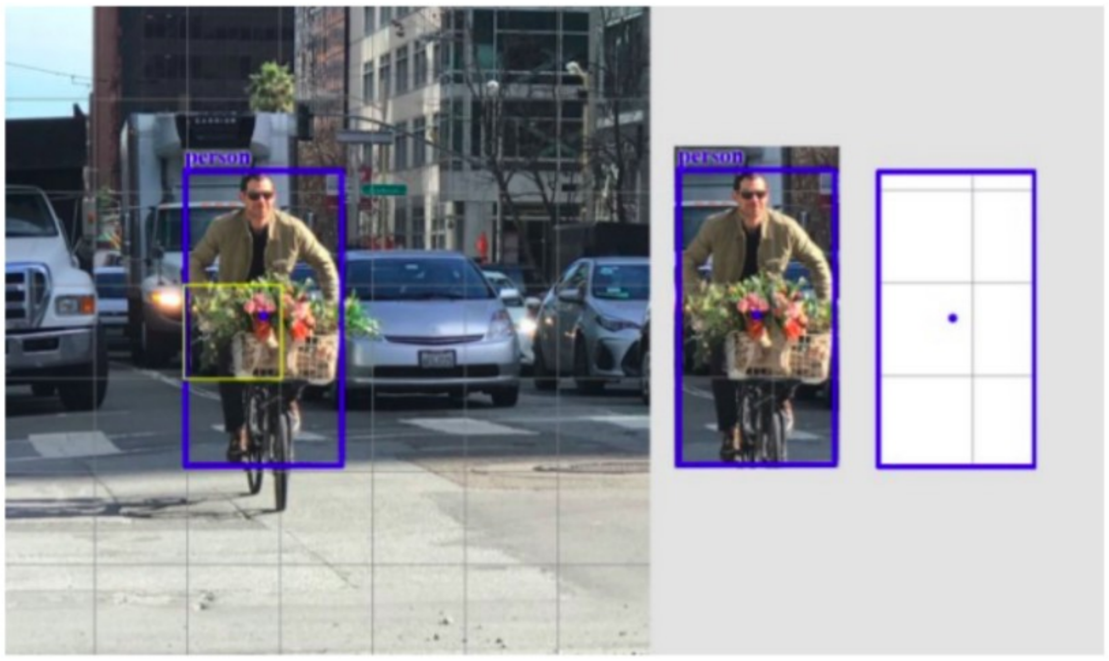

Figure 13. YOLO's Image Grid. Each grid cell detects only one object [80]

This section attempts to summarize YOLO's network architecture and its prediction methodology. YOLO divides the input image into S×S grid (Figure 13). Each grid cell is responsible of predicting one object. For example, in Figure 13, the yellow grid cell tries to predict the person class because its centre (blue dot) lies inside the grid cell [80]. Moreover, each grid cell also predicts a fixed number of bounding boxes. In

Figure 14, the yellow grid cell predicts two bounding boxes for the person object [80]. So for each grid cell, YOLO,

- predicts B bounding boxes with each box having a confidence score.
- detects one object only, irrespective of the number of bounding boxes detected.
- predicts C conditional class probabilities (one for every class in the training dataset).

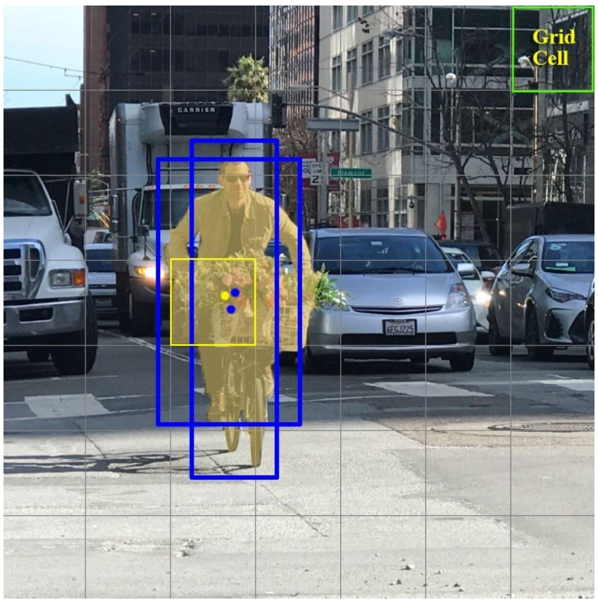

Figure 14. Each grid cell making a fixed number of bounding boxes for one object [80]

Figure 15 shows YOLO's prediction sequence for a $S \times S$ grid. Each bounding box has 5 constituents [80] as follows:

- center x-coordinate (x),
- center y-coordinate (y)
- box width (w)
- box height (h)
- box confidence score.

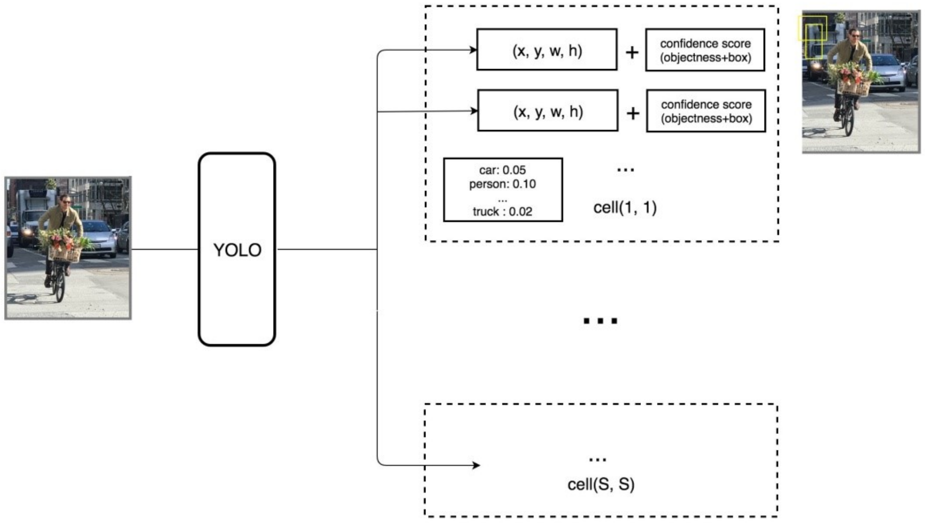

Figure 15. YOLO making S x S predictions with B bounding boxes [80]

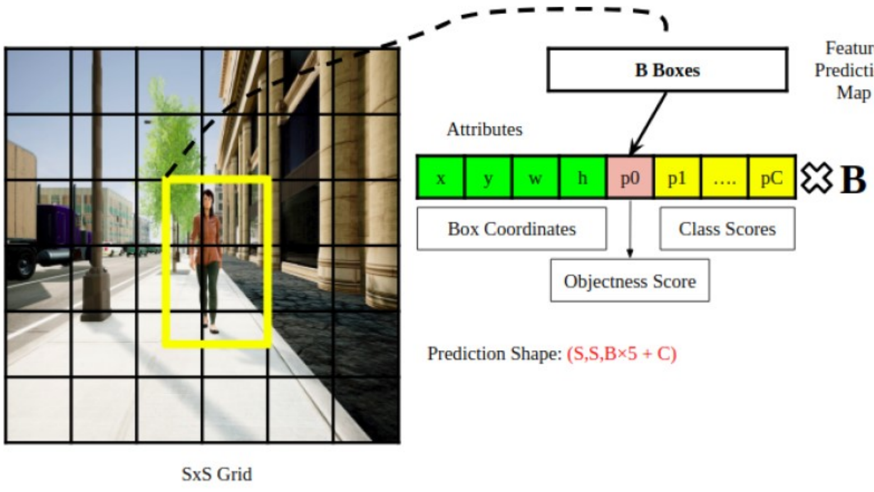

Figure 16. YOLO detecting B bounding boxes for a single image with S x S grid

The confidence score reflects the likelihood of an object present in the bounding box and also accuracy of the bounding box [80]. Each grid cell also predicts C conditional class probabilities for every bounding box detected, giving the class probability of each detected object where C is the number of classes in the training dataset. Therefore, YOLO's prediction shape for a single image is (S, S, B × 5 + C) [80]. Figure 16 shows YOLO predictions on a single image for a complete S × S gird.

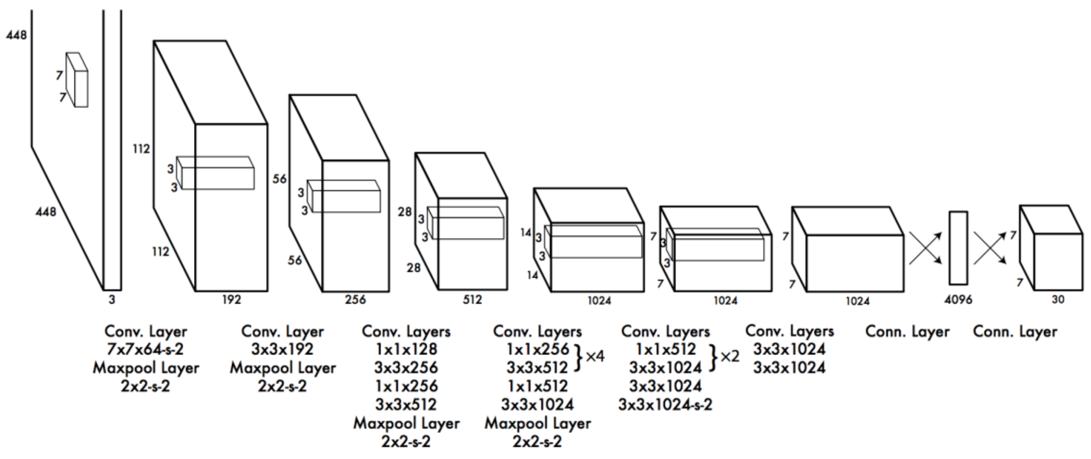

Figure 17. YOLO Network Architecture [70]

Figure 17 details out YOLO's network architecture. YOLO builds a CNN with 24 covolutional layers and two fully connected layers at the end. The convolutional layers extract visual features from the image and two FC layers at the end perform a linear regression to output bounding box parameters [80].

As explained in equation 2-10, YOLO's loss function is a sumsquared error between actual and predicted values [80]. To compute loss for true positives, YOLO only needs one bounding box for each object in the image. However, each grid cell can detect multiple bounding boxes. To eliminate this problem, YOLO selects the bounding box with the highest IoU (intersection over union) with the ground truth during training [80]. On the other hand, YOLO can also make multiple detections for the same object. To fix this, YOLO uses non-maximal suppression [81] to remove detections with lower confidence score. This technique works through sorting the predictions by their confidence score, and then starting from top, removing predictions if current prediction has the same class and an IoU > 0.5 than the previous prediction [80].

2.3.2.2 YOLOv2

Figure 18 shows YOLOv2's accuracy and speed as compared to other popular object detectors. Following is a list of design changes making YOLOv2 better than YOLO:

- Most state-of-art object detection classiers are pre-trained on ImageNet, which operate on smaller input images of 256x256. YOLOv2 is ne tuned with an image size of 448x448 on the entire ImageNet dataset for 10 epochs [77]. This makes YOLOv2 a high resolution classier and give almost a 4% mAP increase when compared to YOLO [77].

- Unlike YOLO that uses fully connected layers for final prediction, YOLOv2 uses anchor boxes on convolutional layers to make predictions. Anchor box is an estimate of a bounding box (width, height). YOLOv2's convolutional layers downsample the image by a factor of 32 therby reducing an input image of 416x416 to 13x13 feature map. Using convolutional layers with achors for prediction reduces mAP by 0.4 but also reduce computational cost by 33% [77].
- Anchor boxes are either provided randomly or calculated from the training dataset through clustering methods. Calculating anchor boxes using any clustering method like K-means clustering helps in increasing the training process [77]. Otherwise the network has to determine the actual anchor boxes by itself. Anchors help in increasing recall.
- YOLOv2 make detections on a 13x13 feature map, which is fine for larger objects, but not fine enough for detecting smaller objects. To fix this problem, YOLOv2 uses a pass-through layer. This layer concatenates the lower resolution features obtained at earlier convolution layer of 26x26 resolution with the higher resolution features at 13x 13 resolution [77].
- After every 10 batches, the network selects a dfferent image dimension to make training multi-scale [77]. This enables the network to train and predict well on different image resolutions.

YOLOv2's implementation uses Darknet-19 [82], an open source NN (neural network) framework written in C and CUDA [83] with 19 convolutional layers.

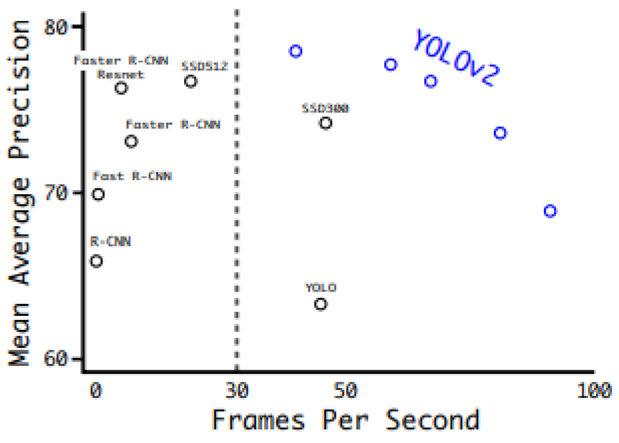

Figure 18. YOLOv2 Accuracy and Speed Compared to other Object Detectors [77]

2.3.2.3 YOLOv3

YOLOv3 improves onto YOLOv2 detection metrics by adding some incremental changes [78]. Following is a list of design changes making YOLOv3 slightly better than YOLOv2 [78]:

- YOLOv3 predicts an object confidence score for each bounding box through logistic regression and gets a score of 1 if its overlap with ground truth is more than any other prediction.
- Each bounding box has an independent logistic classifier to predict detected object class.
- Figure 19 shows YOLOv3's network architecture. Unlike YOLOv2, YOLOv3 predicts bounding boxes at 3 different scales. Feature maps are up-sampled and merged with feature maps from former layers. Furthermore, new convolutional layers are added to precess these feature maps predict object bounding boxes. K-means clustering is used to determine anchor boxes. 9 cluster are selected and divided equally between 3 scales, with 3 predictions at each scale.

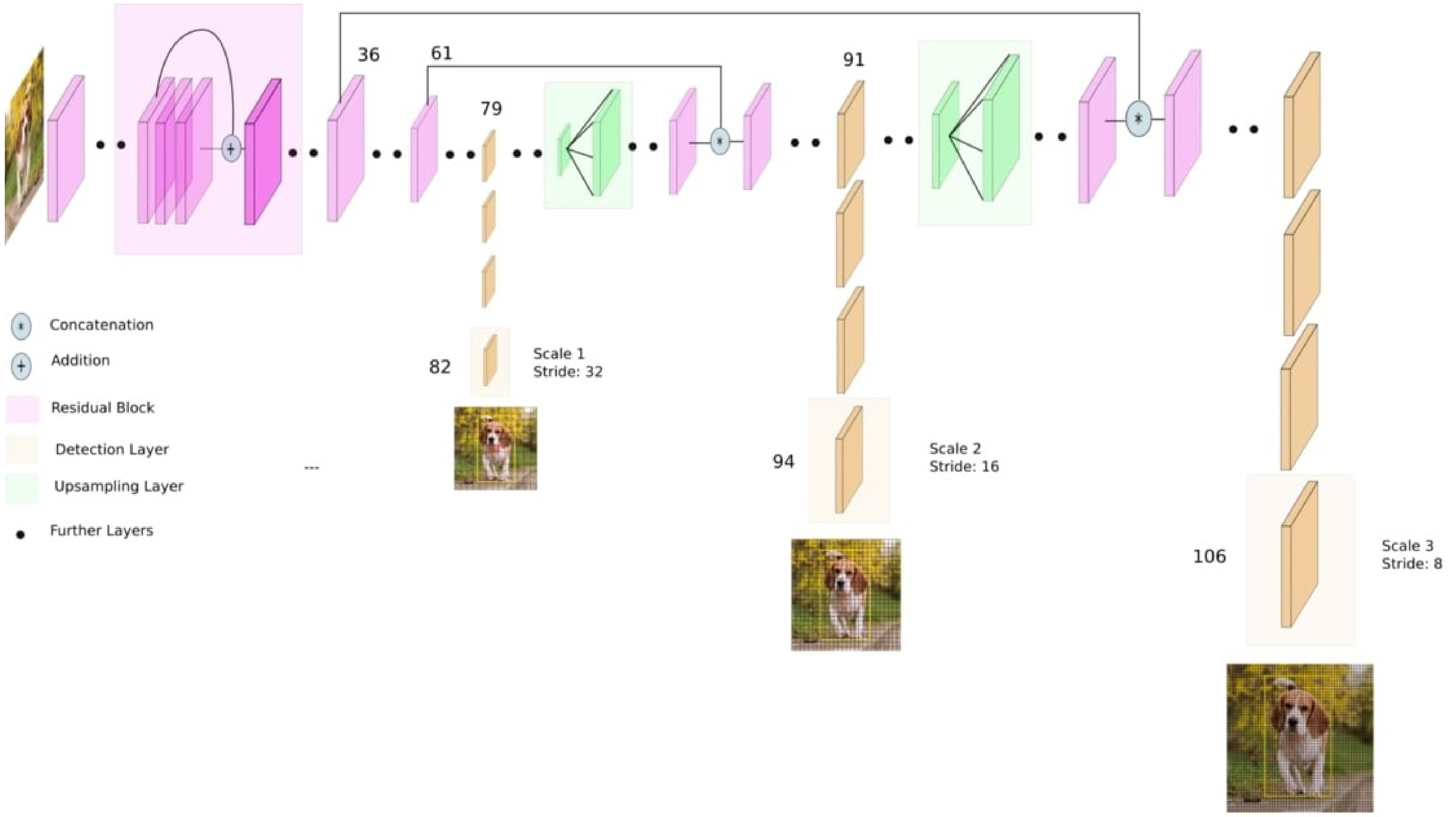

Figure 19. YOLOv3 Network Architecture [73]

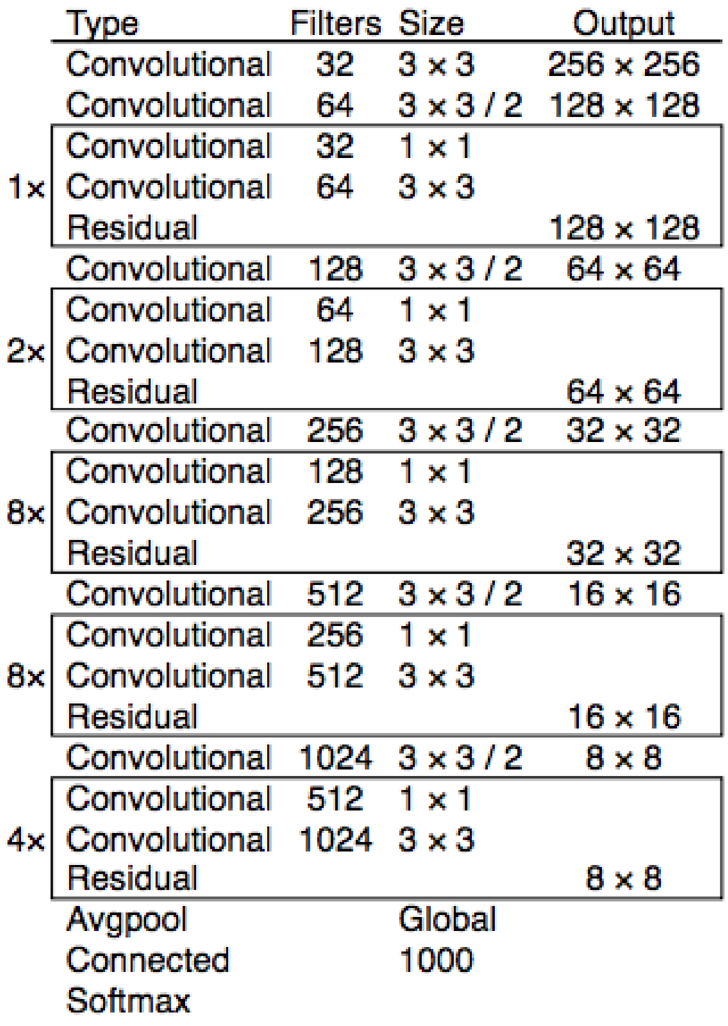

	Type	Filters	Size	Output
	Convolutional	32	3 × 3	256 × 256
	Convolutional	64	3 × 3 / 2	128 × 128
	Convolutional	32	1 × 1	
1×	Convolutional	64	3 × 3	
	Residual			128 × 128
	Convolutional	128	3 × 3 / 2	64 × 64
	Convolutional	64	1 × 1	
2×	Convolutional	128	3 × 3	
	Residual			64 × 64
	Convolutional	256	3 × 3 / 2	32 × 32
	Convolutional	128	1 × 1	
8×	Convolutional	256	3 × 3	
	Residual			32 × 32
	Convolutional	512	3 × 3 / 2	16 × 16
	Convolutional	256	1 × 1	
8×	Convolutional	512	3 × 3	
	Residual			16 × 16
	Convolutional	1024	3 × 3 / 2	8 × 8
	Convolutional	512	1 × 1	
4×	Convolutional	1024	3 × 3	
	Residual			8 × 8
	Avgpool		Global	
	Connected		1000	
	Softmax			

Figure 20. Darknet-53 layers [78]

- YOLOv3 also uses darknet-19 like YOLOv2, but adding all the residual layers and feature map merging makes the network larger, coming to 53 concolutional layers. The underlying framework is therefor now called darknet-53 (Figure 20). This makes the network larger and slower compared to YOLOv2 but improves accuracy.

2.3.2.4 Loss function

The loss function of YOLO contains three parts: the localization loss (errors between the predicted box and the ground truth box), the confidence loss (objectness of the box) as well as the category loss, as given in equation (2-10) [70] below:

$$Loss = loss_{localization} + loss_{confidence} + loss_{class}$$

$$= \sum_{i=0}^{S^2}\sum_{j=0}^{B} 1_{i,j}^{obj}\left[(t_x-\hat{t}_x)^2+\left(t_y-\hat{t}_y\right)^2+(t_w-\hat{t}_w)^2+(t_h-\hat{t}_h)^2\right]$$

$$+\sum_{i=0}^{S^2}\sum_{j=0}^{B}(1_{i,j}^{obj}[-\log(\sigma(t_o)]+1_{i,j}^{nobj}[-\log(1-\sigma(t_o)]) \tag{2-10}$$

$$+\sum_{i=0}^{S^2}\sum_{j=0}^{B} 1_{i,j}^{obj}\left[\sum_{c=1}^{C} BCE\left(\hat{p}_c,\sigma(p_c)\right)\right]$$

Here, each line represents each part of loss. t_x,t_y are the predicted bounding box coordinates and t_w,t_h are the width and height of the box. $1_{i,j}^{obj}$ indicates that j th bounding box in i th cell is responsible for that prediction [70]. t_o is the predicted objectness score for that box and p_c is the predicted class probability. Mean Squared Error (MSE) function is adopted to calculate the localization loss and Binary Cross Entropy (BCE) function is employed to calculate the confidence loss and classification loss.

2.3.2.5 Evaluation Matrics

Intersection over Union, also referred to as the Jaccard Index, is one of the most common and most basic concept to measure the performance of object detector. It quantifies the similarity between the ground truth bounding box and the predicted bounding box to evaluate how accurate the predicted box is. The IoU score ranges from 0 to 1, the similar the two boxes, the higher the IoU score. It is defined and calculated as the area of the intersection divided by the area of the union of the predicted bounding box and the ground-truth box, as illustrated in Figure 21.

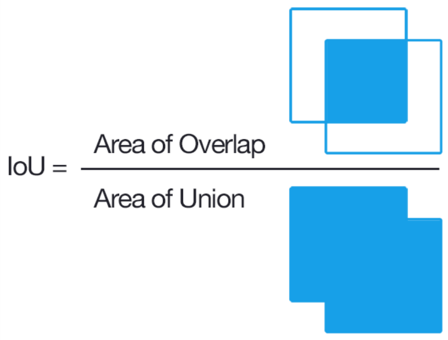

Figure 21. Illustration of Intersection over Union (IoU) [84]

By computing the IoU score for each detection, the IoU values above the defined threshold are considered positive predictions and those below are considered to be false predictions. More precisely, the predictions are classified into True Positives (TP), False Negatives (FN), and False Positives (FP) [85].

An example of confusion matrix of car detection is shown in Table 2- 3.Generally speaking, when the prediction class matches the class of the ground truth and IoU is greater than some certain threshold, then this prediction would be considered as truth positive (TP); otherwise, when the prediction class doesn't match the ground truth class or the IoU is lower than the threshold, then it would be viewed as false positive (FP). False negative (FN) refers to that the ground truth cannot be detected and true negative (TN) represents a correct misdetection.

Table 2. An example of confusion matrix of car detection

Actual / **Prediction**	**Car**	**Not Car**
Car	True Positive (TP)	False Positive (FP)
Not Car	False Negative (FN)	True Negative (TN)

Based on the confusion matrix, precision and recall can then be calculated and obtained. Precision is the ability of a model to detect only the relevant objects, which is defined as the number of true positives divided by the sum of true positives and false positives, as shown in equation (2-11):

$$Precision = \frac{TP}{TP + FP} = \frac{true\ object\ detection}{all\ detected\ boxes} \qquad (2\text{-}11)$$

Recall is the ability of a model to identify all the relevant objects, which is defined as the number of the true positives divided by the sum of true positive and false negatives (all ground truths), as shown in equation (2-12) [85]:

$$Recall = \frac{TP}{TP + FN} = \frac{true\ object\ detection}{all\ ground\ truth\ boxes} \qquad (2\text{-}12)$$

During detection, not only can the detector output the predicted bounding box, but also can predict the confidence score, which represents the probability that the bounding box contains the object. By setting the threshold for confidence score at different levels, different pairs of precision and recall can be obtained, and then Precision-Recall (PR) curve can be plotted, which indicates the relationship between the two metrics and helps to judge the performance of an object detector. An object detector of a particular class is considered good if its precision stays high as recall increases, which means that no matter how you vary the confidence threshold, the precision and recall will still be high [85].

Although the precision-recall curve can be used to evaluate the performance of a detector, it is not always easy to compare among different detectors straightforward when the curves cross with each other. Therefore, the average precision (AP), a numeric metric, which calculates the area under the Precision-Recall curve, is adopted. Essentially, AP is the precision averaged across all unique recall levels between 0 and 1 [85]. Given a PR curve, there are two ways to calculate AP: 11-point interpolation and all-points interpolation. The 11-point interpolation is a traditional method, which summarizes the shape of Precision-Recall curve by averaging the precision at a set of 11 equally spaced levels [0,0.1,0.2, …,1], as shown in Equation 13 [85].

$$AP = \frac{1}{11} \sum_{r \in \{0,0.1,\dots,1\}} p_{interp}(r) \tag{2-13}$$

With

$$p_{interp}(r) = \max_{\tilde{r}:\tilde{r} \geq r} p(\tilde{r}) \tag{2-14}$$

Where $p(\tilde{r})$ is the measured precision at recall $\tilde{r}$. The interpolated precision p_{interp} at a certain recall level r is defined as the highest precision found for any recall level $\tilde{r} \geq r$, as shown in equation 14. While currently, a new standard is to choose all unique recall levels in the data and interpolate through all points, without interpolating only 11 equally spaced points, which improves precision under low AP. AP can then be obtained by calculating the area under the interpolated precision-recall curve, as shown in equation (2-15) [85]:

$$AP = \sum_{r=0}^{1} (r_{n+1} - r_n)\, p_{interp}(r_{n+1}) \tag{2-15}$$

Where,

$$p_{interp}(r_{n+1}) = \max_{\tilde{r}:\tilde{r} \geq r_{n+1}} p(\tilde{r}) \tag{2-16}$$

An example of all-points interpolation in Precision-Recall curve is illustrated in Figure 22. The blue line is the original PR curve and the red dotted line is the interpolated version. The average precision (AP) is then acquired by calculating the area under the red dotted line. mAP (mean Average Precision) is the average of AP among all the classes.

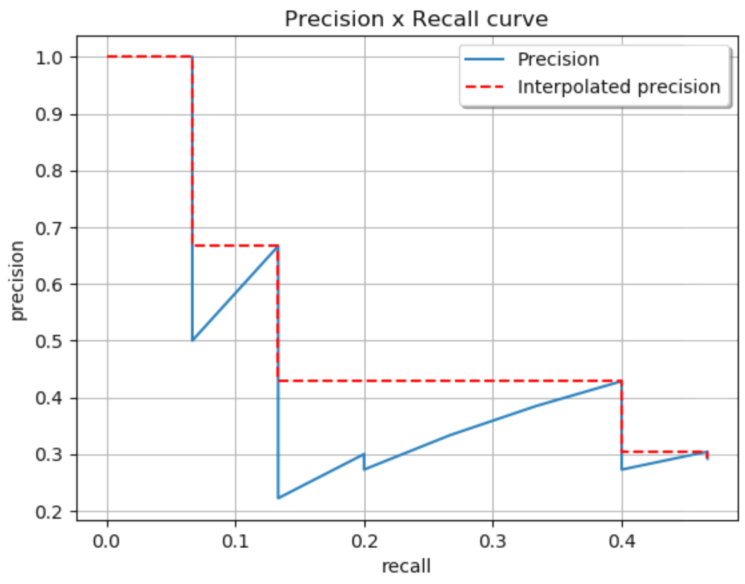

Figure 22 An example of all-points interpolation in Precision-Recall curve [85]

2.4 Datasets for environmental perception

An essential component in the development of a machine learning method is an appropriate dataset. Machine learning can be applied to analyze data that are difficult to express mathematically. Numerous complex systems, for instance, autonomous vehicles components such as object detection rely on machine learning-based methods. The qualitative and quantitative datasets often required to generalize complex problems with machine learning.

Assuming a correctly designed machine learning model, a high computational power machine and optimally set training parameters, the model is likely to perform well. However, it is proven [86] that the size of dataset makes a lot of impact on results. Especially for the machine learning-based visual object detection techniques, the quantity of dataset improves the performance of the machine learning model [86].

In this section, some popular datasets available for object detection and their performance on different object detection models will be discussed. Some of the available object detection dataset provides range information up to about 100 meters measured by LiDAR or stereo camera as a ground truth, but none of the dataset is focussed or specifically designed to predict the distance to the detected object. Additionally, the available datasets contains annotated objects which are relatively big in size, in other words, close to the camera and secondly contains images of urban driving scenarios, captured during sunny day and in decent weather conditions.

The recently published nuScenes [87] is a multimodal dataset for autonomous driving. This dataset was recorded with 6 cameras, 5 radars, and 1 lidar, all with a 360-degree field of view. It consists of 1000 scenes, each 20 seconds long and fully annotated with 3-dimensional bounded boxes for 23 classes and 8 attributes. The Honda Research Institute 3D (H3D) Dataset [88] is a large scare 3D multi-object detection a tracking dataset collected using a 3D LiDAR Scanner. H3D consists of 160 crowded traffic scenes. However, both datasets are focused on urban environments and traffic scenes, which differ from a railway setup.

Microsoft COCO Dataset (MS COCO) [89] contains complex scenes with common everday objects. Dataset contains in total 91 object classes with 2.5 million instances in about 328k images. The dataset is basically for object recognition purpose hence does not contaians any objects pose information. Objects are labeled using segmenting individual object instances.

2.4.1 Kitti Dataset

KITTI dataset [90] is a dataset built by the Karlsruhe Institute of Technology and Toyota Technological Institute at Chicago. The dataset was recorded from a car equipped with one Inertial Navigation System (GPS/IMU), one Laser scanner, two grayscale cameras and two high-resolution color cameras, (as shown in Figure 23) while driving around the city of Karlsruhe in Germany.

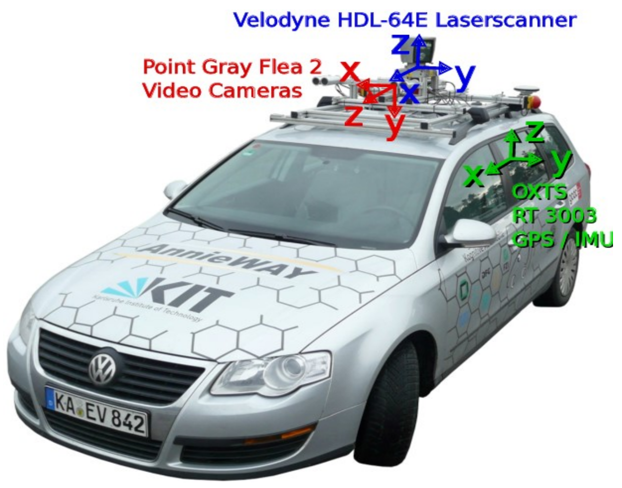
Velodyne HDL-64E Laserscanner
Point Gray Flea 2 Video Cameras
OXTS RT 3003 GPS / IMU
x
y
z

Figure 23. Recording Platform of KITTI dataset [90]

The detailed information about that recording platform and sensor setup can be seen in Figure 24.

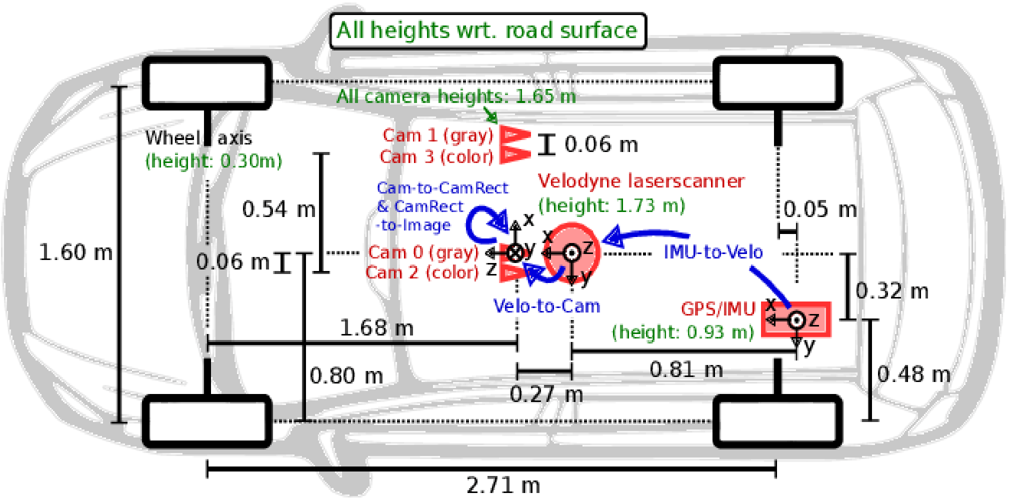

Figure 24. Detailed information on the recording platform [90]

The images include the scene of City, Residential, Road, Campus, and Person, which demonstrates the diversity of the KITTI dataset. The images are at the resolution of 1242x375 pixels. Some examples can be seen in Figure 25.

The accurate ground truth in benchmarks is provided by the Velodney laser scanner and the GPS localization system. Each object in the dataset is described by several parameters, including the information about the class of the objects (8 types available), truncation and occlusion, the 2D bounding box information of an object, the dimension and location of the 3D object as well as its orientation. The detailed explanation of the annotations in the KITTI dataset can be seen in Table 3.

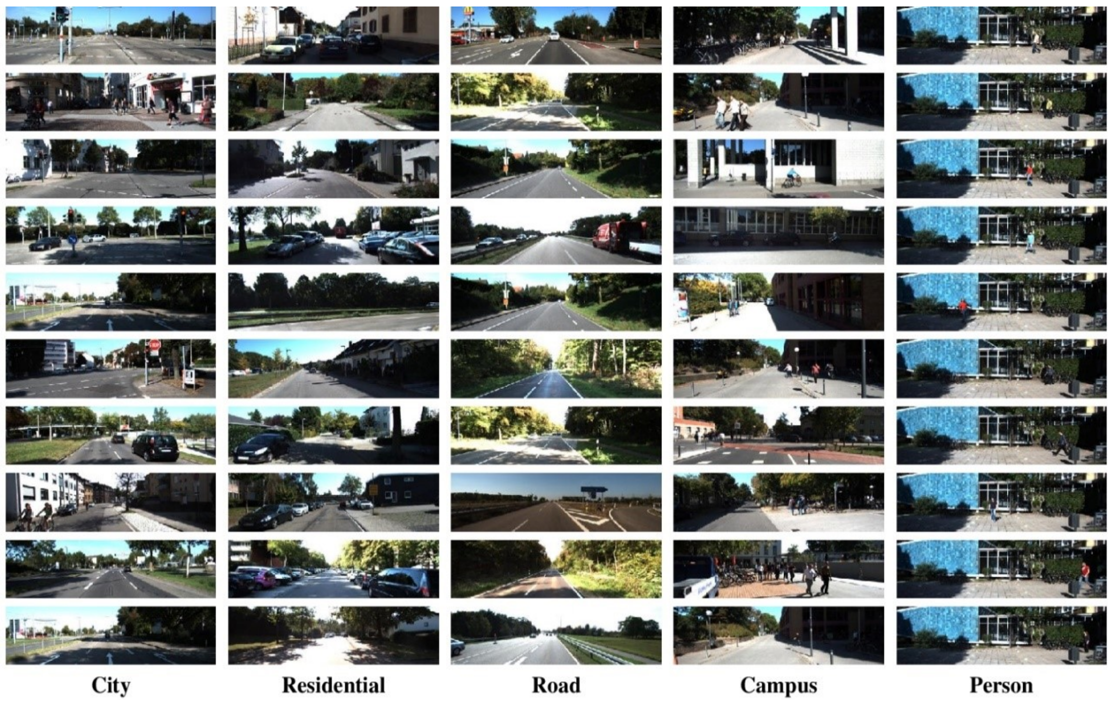

Figure 25. Examples from KITTI dataset [90]

Table 3. A detailed explanation of the annotations in KITTI dataset [90]

No.	Contained information	Possible values
1	type of the object	'Car', 'Pedestrian', 'Van', 'Truck', 'Cyclist', 'Person_sitting', 'Tram', 'Misc', 'DontCare'
2	the information whether the object is 'truncated' or 'not-truncated', where 'truncated' means that the part of the object is outside of the image range	float value from 0.00 ('non-truncated') to 1.00 ('truncated'), the higher the value the smaller the visible part of the object
3	the information about the occlusion state of the object	'0' - fully visible '1' - partly occluded '2' - largely occluded '3' - unknown
4	alpha angle - the observation angle of the object	$[-\pi, \pi]$
5-8	2D bounding box of object in the image	left, top, right, bottom pixel coordinates
9-11	3D object dimensions	height, width, length (in meters)
12-14	3D object location	x,y,z in camera coordinates (in meters)
15	rotation ry around Y-axis	$[-\pi, \pi]$ (in camera coordinates)

Here, in the row of No.1 in Table 3, ‘DontCare’ labels denote regions where objects have not been labeled, e.g. because they have been too far away from the laser scanner. What’s more, based on these classes, all the objects in the dataset were divided into two classes again, i.e. person and car. To be specific, the class of ‘Pedestrian’, ‘Cyclist’ and ‘Person_sitting’ were combined into the class of ‘person’, and the types of ‘Car’, ’Van’,’ Truck’, ’Tram’ and ’Misc’ were combined into the class of ‘car’. The object location at Z-axis (camera direction) is considered as the distance between camera and object. The distance range in the KITTI dataset is between 0 to roughly 150 meters. An example of the labeled images is shown in Figure 26.

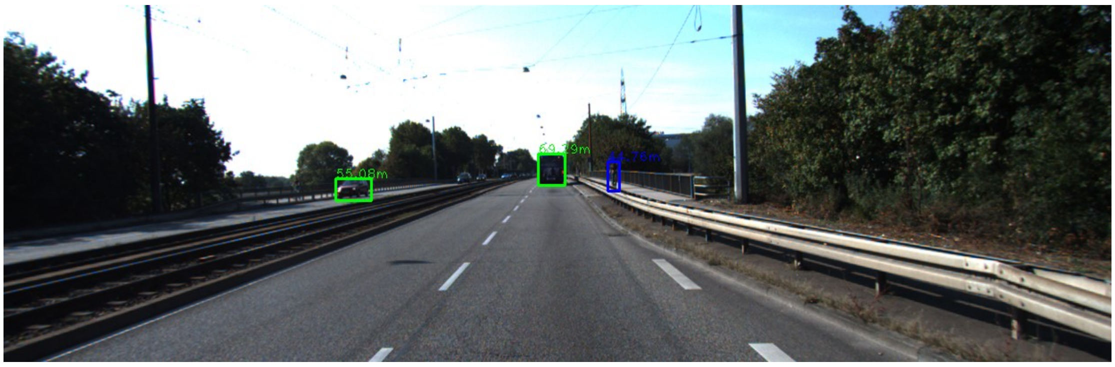

Figure 26. An example of labeled images in KITTI dataset [90]

2.5 Distance estimation

In many computer vision applications such as robotics and specifically in autonomous vehicles, precise depth information is crucially important. In this section, an introduction to often used sensors and approaches to estimate distance is given. Some of the sensors and methods which are commonly used in indoor and outdoor applications to produce distance or depth information are as follows.

2.5.1 LiDAR

LiDAR (Light Detection And Ranging) is a sensing method that measures the distance to the target by measuring the time required by the transmitted pulse of invisible laser light to reflect back to the sensor. The difference in laser pulse returns time and wavelengths is further used to make a digital 3D representation of target or surrounding. LiDAR is considered a reliable method to detect an object and accurately measure the distance to the object which is in its range, has high reflectivity and of sufficient size [91]. More than the distance measurements, LiDAR also provides size, the position of objects, and the speed of moving targets.

However, one of the limitations of LiDAR sensors is their limited range. Typically currently available commercial off-the-shelf LiDAR sees well about 60 to 100 meters [92]. Some LiDAR such as SICK LDMRS claiming the range up to 300 meters for ideally 100% reflective objects but this is dubious and practically not achievable. LiDAR is independent of illumination and weather conditions. However, rain, snow, fog, or dense dust causes the scattering of light. Therefore a tiny amount of laser pulses return back to the sensor which causes reducing the effectiveness and range of the LiDAR.

LiDAR is commonly used in indoor and outdoor robot localization [93] [94], mapping [95], obstacle detection [96], human tracking [97], and also become a part of some autonomous cars [98].

2.5.2 RADAR

RADAR (RAdio Detection And Ranging) works in much similar to LiDAR. The difference is it transmits the radio waves instead of a laser and analyzes the waves reflected back to it. The reflected waves tell that the obstacle is in the propagation direction. It is also used to determine the velocity, distance, and angle of objects. Radar produces lighter data than a camera and a LiDAR.

The radio waves have less absorption than light waves. Thus, radar can work relatively longer range than lidar and can reliably work in adverse weather conditions such as rain, snow, fog. However, commonly available long-range radar sensors for autonomous cars ranges up to 200 meters. Another advantage of radar is that the reflection helps to see behind the obstacles. However the significant limitations of radar are it easily faces interference with several objects in the air, poor quality to distinguish between multiple objects, and also the radio waves travel slower than light waves which cause slower data receiving.

2.5.3 Stereo Camera

Another way to determine depth information is the stereo vision. The term “stereoscopic” refers to the human ability to see simultaneously from both eyes in similar but slightly different viewing angles, as a result of the physical horizontal separation between the left and right eye which gives human, true depth perception [99], also known as stereopsis. The difference in object location in images seen by the left and right eyes is referring to as retinal or binocular disparity [99].

A stereo camera is the type of camera setup with two or more cameras. The stereo camera is widely used in robotics, and it gives human-like vision perception to humanoids to perform tasks such as object manipulating tasks. For such tasks, the robots need close object depth estimation. In the use case of short-range applications, a good stereo camera can reliably and accurately estimate the depth and can even eradicate the need for lidar or radar sensors.

Figure 27 shows the setup of ideally parallel stereo cameras. The depth estimation is possible only for the overlapping field of view (FOV) of cameras, as shown in Figure 27. The overlapping FOV depends on the physical horizontal separation between the cameras refers as baseline B and the FOV angle of the camera. The baseline also defines as centres of projection of cameras C_L and C_R. Point P in 3D space projects to P_L and P_R on the image plane. X_L and X_R are co-ordinates of P_L and P_R with respect to principal points C_L and C_R. The depth to point P in 3D space refers to Z is the difference between point P and the baseline.

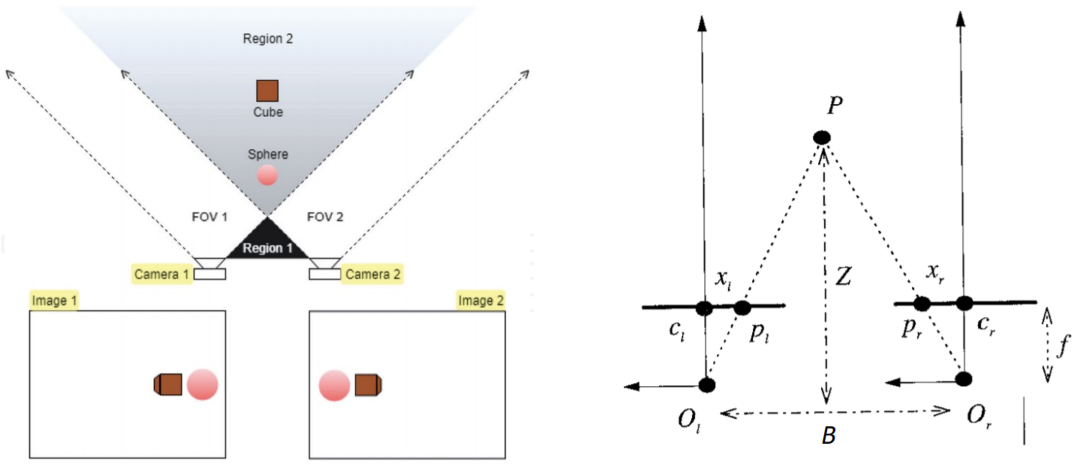

Figure 27. The stereo vision setup

As we know from similar triangles theorem, two triangles of the same shape and different in size are similar if their corresponding angles are congruent and their corresponding sides are in proportion. In Figure 27, the triangles (P_L,P,P_R) and (O_L,P,O_R) are similar. The depth Z can be express as a function of x_L, x_R, *f,* and *B*.

$$\frac{B + x_L - x_R}{Z - f} = \frac{B}{Z} \tag{2-17}$$

$$d = x_L - x_R \tag{2-18}$$

$$z = f\frac{B}{d} \tag{2-19}$$

Disparity d measures the distance between the corresponding points in the left and right images. The depth Z is inversely proportional to the disparity. The representation of computed disparity between the entire left and right images is known as a disparity map. The disparity map is a 3D image and can be visualized in 3D known as a point cloud or in 2D known as a disparity image. In disparity image, bright pixels represent the highest disparity or closest points in 3D space and dark points have the lowest disparity or farthest points in 3D space. Furthermore, algorithms such as block matching also produce uniform and accurate bounding boxes [100].

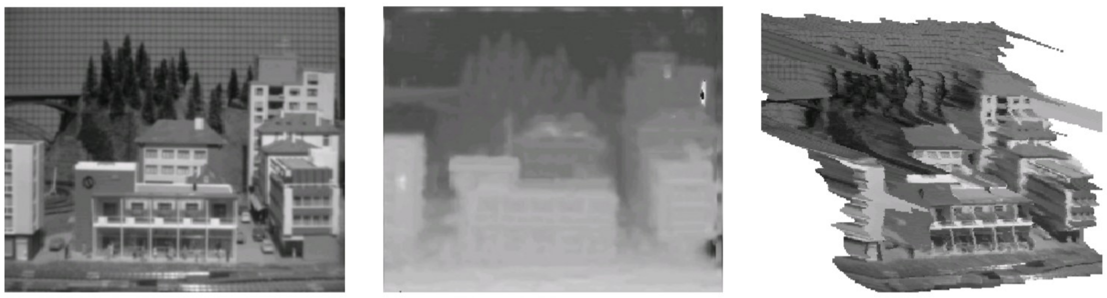

Figure 28. Input – First frame (left image), Depth image (center), Prespective view (right) [100]

The baseline is inversely proportional to the depth error. The wider is the baseline, the better is the depth estimation, but it also causes a smaller overlapping field of view. Thus, challenging to calibrate due to a large minimum depth of field.

$$Depth\, error \propto \frac{1}{B} \tag{2-20}$$

In general, the stereo cameras are not ideally parallel to each other. Therefore required stereo calibration to align them parallel, the calibration gives the external relation between the cameras with respect to reference point in the 3D world coordinate system. The relationship is further used to project the images from the left and right camera on a reference system [100].

As shown in Figure 29, the wide baseline stereo camera in comparison to the narrow baseline stereo camera is suitable for long-range distance estimation however in practice it is not possible to set up a stereo camera for long-range.

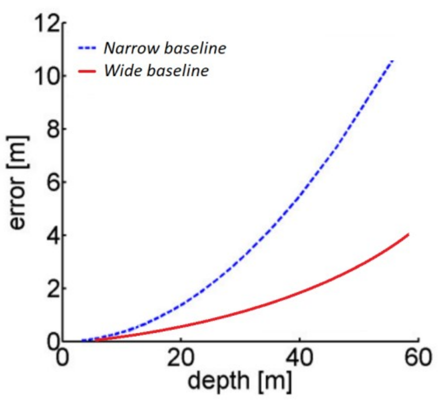

Figure 29. Error-Depth diagram for narrow and wide baseline [101]

2.5.4 Monocular Camera-based approaches

Previous research for distance estimation mainly paid particular attention to build a model that represents the geometry relationship between points on images and their corresponding physical distances on the real-world coordinates. Inverse perspective mapping (IPM) [102] is one of these classical methods, which transforms the forward-facing images to a top-down “bird’s eye” view and changes the nonlinear relationship between distances in the image and the real world into a linear relationship. However, the limitation of this method is that it performs poorly when objects lie on the sides of the camera or the curved road and when objects are far away from the camera (above 40 meters) [103].

Sadreddini et al. [104] proposed a system that estimates distances from a single camera for an indoor mobile robot application. The developed method utilized information from floor line detection and morphological operations extracted from an object to estimate the distance. However, this method was evaluated in only one use case. Pathi et al. proposed a method to estimate the distance between humans and a robot using images from a single camera mounted on the robot. The method first extracts 2D poses (skeleton structure) of the humans in the scene and then it uses the effect of perspective distortion from the camera’s point of view to estimate the distance. For the experimental validation of the method, the authors collected three datasets and the method demonstrated its effectiveness.

A recent work by Ali et al. [105] proposed a real-time vehicle distance estimation using a single view geometry. A fully convolutional deep network is used for lane detection on the road. Subsequently, an Inverse Perspective Mapping (IPM) and camera height are estimated from a known lane width and the detected horizon. At last, the distances of the vehicles on the road are calculated by back projecting image point to a ray intersecting the reconstructed road plane. The method was evaluated in three datasets, KITTI [90], nuScences [87], and Lyft level 5 dataset [106]. All the datasets have color images along with LiDAR data. The proposed method performed better on the nuScenes and Lyft datasets in comparison to two other deep learning approaches. However, the proposed method did not perform well on the KITTI dataset.

In [103], a base model that directly predicts distances for given objects in the images was introduced, which contains three parts: a feature extractor to generate a feature map for the entire RGB image, a distance regressor to directly predict a distance from the object-specific Region Of Interest (ROI) feature and a multi-class classifier to predict the category of an object from the ROI feature, as shown in Figure 30 [103].

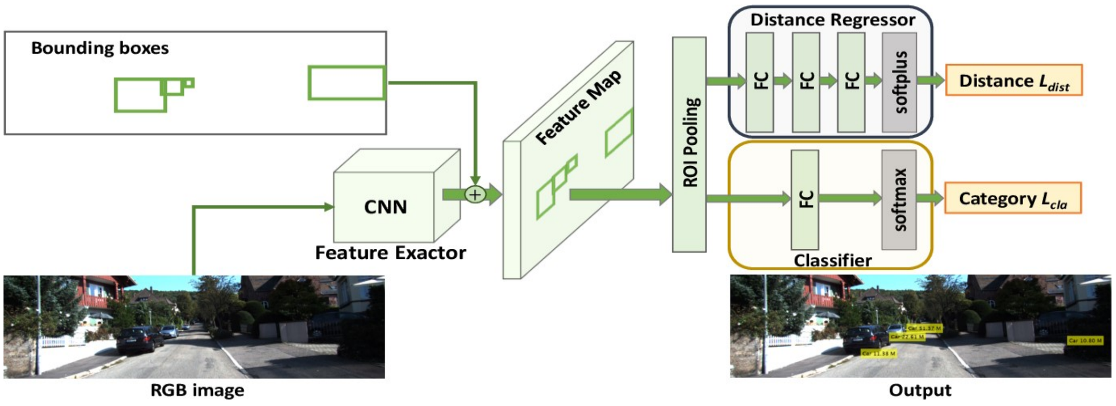

Figure 30. Framework of the base model [103]

To be specific, the popular network structures (vgg16 and res50) are adopted as feature extractor and extract the feature map for the whole image. Then the extracted feature map from the feature extractor and the object bounding boxes are feed into an ROI pooling layer to generate a fix-size feature vector to represent each object in the image [103]. After that, the distance regressor and classifier utilize the pooled feature to predict a distance and class information for each object. The distance regressor is made up of three fully connected layers and a softplus activation is employed on the output of the last fully connected layer to make sure the predicted distance is positive. The classifier uses a fully connected layer followed by a softmax function to predict the category.

Furthermore, in [103], an enhanced model with a keypoint regressor is proposed, which optimizes the base model by introducing a projection constraint and improves the performance of distance prediction, as shown in Figure 31 [103]. Here, the keypoint regressor is adopted to predict an approximate keypoint position in the 3D camera coordinate system [103].

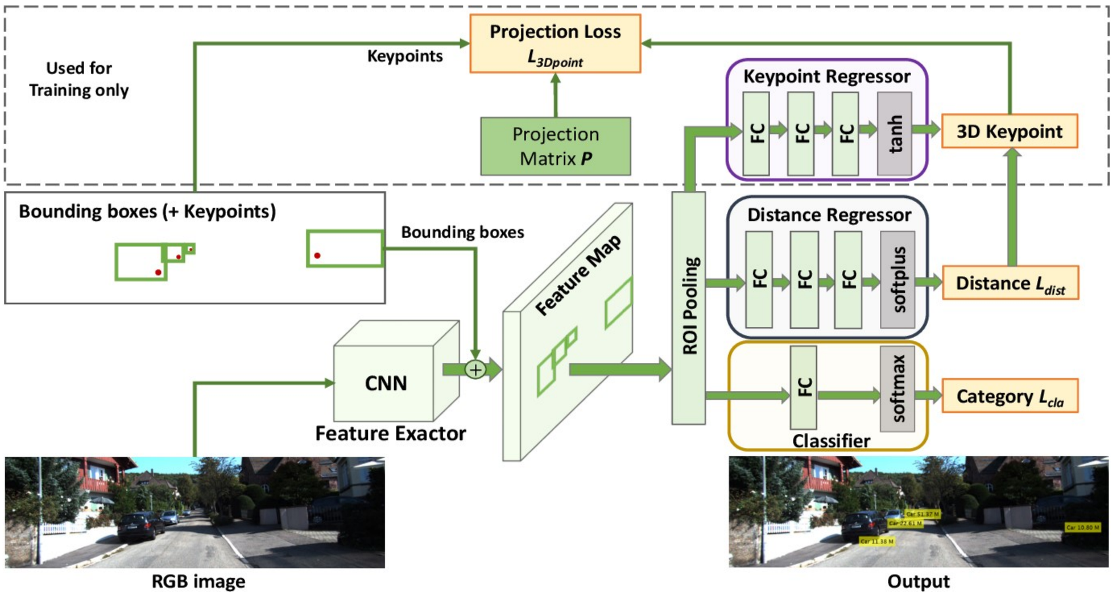

Figure 31. The Framework of the enhanced model [103]

2.5.1 Evaluation Matrices

RMSE (Root Mean Square Error) is a measure of how far spread the data is from the line of best fit. Equation 2-21 shows the spread of predicted distance from the ground truth which is the actual distance in a total of *N* detections. RMSE is a common technique used to analyze regression problems. Since distance estimation can be classified as a regression problem, RMSE is a good metrics to evaluate experimental results.

$$RMSE = \sqrt{\frac{\sum_{i=1}^{N}(distance_{predicted} - distance_{actual})^2}{N}} \tag{2-21}$$

3. Dataset for long-range object detection and distance estimation

Among all the significant advancements in many sectors due to the introduction of machine learning, the most notable achievement has been seen in object recognition. Numerous datasets for object recognition were created in recent years from the images gathered from the internet such as Google, for example, COCO [89], SUN [107], PASCAL VOC [108] and ILSVRC [53] [109]. Some datasets were formed by collecting the images from a multisensory obstacle detection system containing cameras and other short-range ranging sensors such as LiDAR or RADAR mounted on a car moving on streets such as KITTI [90] and the Caltech Pedestrian Datasets [110]. The labelled datasets are used to train and evaluate machine learning models such as AlexNet [48], Faster-RCNN [111], YOLO [70] and FCIS [112]. Also, the comparison of various datasets and performance of machine learning models on the datasets is made [110] to evaluate the quality of datasets and performance of models. The current popular datasets and object detection models show promising results for object detection in indoor and outdoor applications.

However, there are no datasets which are suitable for long-range object detection and distance estimation. The currently available dataset contains labelled objects which are at short-distance; hence the object size in the image is relatively big. Such as the state-of-the-art datasets COCO [89], KITTI [90] consists of images captured relatively at a short-range up to approximately 100 meters thus the size of the object is large in the image and tends to work for short-range object detection. The distance range and close objects labelling fulfill the requirement of autonomous cars obstacle detection system where the required range is relatively less in comparison to an obstacle detection system for railways. Due to that in the thesis, it was needed first to develop a new dataset that can work for long-range obstacle detection. The developed dataset is named as Long-Range Object Detection and Distance Estimation (LRODD).

The dataset was prepared in order to detect objects at short to long-distance from 20 meters to 1000 meters. moreover, the dataset created in this thesis contains images in which objects look smaller in size as they were captured at longer distances of up to 1000 meters. The objects' size-range due to capturing at different distances is needed to train machine learning models to detect objects small in size due to long-distance capturing.

The created dataset contributes not only to long-range object detection. It is also beneficial for providing long-range ground truth distance information to the labelled objects in images. Distance information is further utilized to train novel machine learning-based methods to estimate the object distance from a single monocular camera which is further explained in Chapter 4. Additionally, the use of the created dataset for sensor fusion and object tracking is given in Chapter 5 and Chapter 6 respectively. In the next sections, the data acquisition procedure, data extraction, and data augmentation procedures to create the LRODD dataset are described.

3.1 Dataset Preparation

The LRODD dataset is generated from the images taken from various experiments, including experiments conducted over two years period within the project SMART - SMart Automation of Rail Transport [16]. SMART image dataset is the first dataset aiming at object recognition for railways and it consists of images of objects, potential obstacles, on railway tracks. The images were captured using the vision sensors of SMART multisensory Obstacle Detection System (ODS) [16]: three RGB cameras with optical zooming functionality and Thermal Camer. In addition, LiDAR and GPS sensors were used for ground truth distance recording. The images of different objects were captured at different day and night time and in different weather conditions such as snow, dry, rain.

The experiments were conducted at the University of Bremen and Serbian Railways. Furthermore, in this Thesis, the data augmentation techniques were developed and implemented to expend the size of the dataset collected from real-world experiments.

In the following, before giving details on data acquisition and data collection experiments, the specifications of the used sensor are given.

3.1.1.Sensors Specifications

RGB Cameras:

The zooming cameras from the imaging source (TIS) (Figure 32) were selected due to their optical zooming functionality to cover long-range imaging and high resolution. The zoom camera DFK Z12GP031 [113] is categorised as GigE interface cameras that provide high data transfer rate, high bandwidth, and power over Ethernet (PoE) features which, in comparison to, for example, USB interface or FireWork interface, allows transmitting of twice bigger images. In performed experiments, three RGB cameras were used, configured at different zooming factors, to cover short, mid and long-range objects imaging. The main features of the DFK Z12GP031 zoom GigE camera are listed in Table 4.

Figure 32. DFK Z12GP031 from the Imaging Source [113]

Table 4. Main Features DFK Z12GP031 zoom GigE camera

Specification	
Resolution	2,592×1,944 (5 MP)
Frame rate	15 FPS (Maximum)
Pixel Size	H: 2.2 µm, V: 2.2 µm
Focal length	4.8 mm (wide) to 57.6 mm (tele)
Interface	GigE
Supply voltage	11 VDC to 13 VDC or POE: 48 VDC to 56 VDC
Trigger	Software and Hardware
I/Os	Yes
Dimension	H: 50 mm, W: 50 mm, L: 103 mm
Weight	330 g
Shutter	$^{1}/_{20,000}$ s to 30 s

Gain	0 dB to 12 dB
White balance	-2 dB to 6 dB

Thermal camera:

The thermal camera FLIR TAU2 model (Figure 33) with a resolution of 640x480 pixels and a 100mm objective lens [114] was chosen for SMART project experiments due to the GigE ethernet interface expansion module. The camera is further equipped with the narrow field lens with a long focal distance to achieve sufficient magnification for the detection of distant objects. The thermal camera also known as the IR camera is sensitive to wavelength in the infrared region. The imaging in invisible space helps to see the objects emitting invisible heat radiations regardless of lighting conditions.

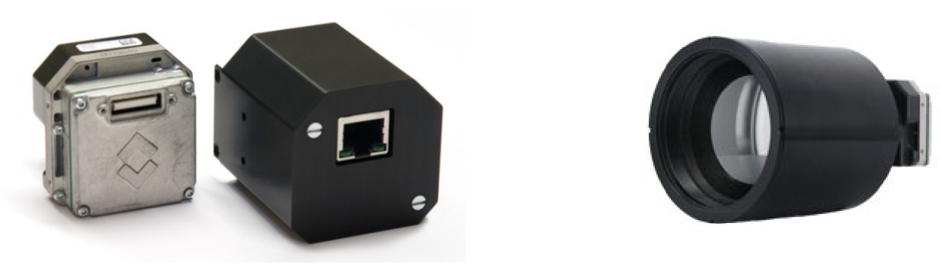
(a) FLIR Tau2 camera and GigE ethernet module from worskwell

(b) Objective lens from FLIR

Figure 33. FLIR Tau2 Camera and objective lens [114]

FLIR lens of 100mm focal length and f-number 1.6 fulfills all requirements for this sensor channel, detailed in Deliverable 1.1 of SMART project [115]. The main features of the selected thermal camera can be found in Table 5.

Table 5. Main Features of FLIR Tau2 Camera

Specification	
Resolution	640x512 (0.328 MP)
Frame rate	9 FPS (Maximum)
Pixel Size	17 µm
Focal length	100 mm
Interface	Workswell GigE adapter
Supply voltage	POE: 48 VDC to 56 VDC
Spectral range	Long Wavelength InfraRed (LWIR)

I/Os	Yes
Dimension (including lens)	Length: 110 mm Diameter: 82 mm
Weight (including lens)	479 g
Operational temperature range	-40° C to +80° C external temp
Gain	0 dB to 12 dB
Accuracy	±5°C
field of view	6.2° x 5°

Night-vision camera

A monochrome DMK 33GP031 CMOS camera (Figure 34) from TIS [113] with GigE communication interface equipped with a custom made image intensifier and objective lens from HARDER Digital SOVA was chosen for SMART ODS. The image intensifier and objective lens were designed to capture a minimal amount of light and magnify it on the CMOS sensor to produce a digital image of the scene. Table 6 summarizes the features of the CMOS sensor.

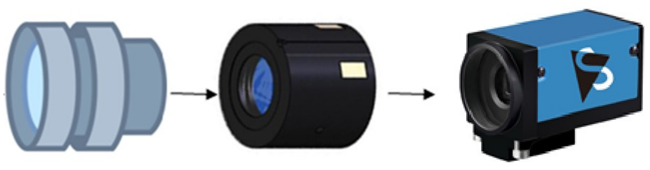

Figure 34. A monochrome CMOS camera sensor equipped with image intensifier and objective lens [116]

Table 6. Main features of the Nigh vision camera

Specification	
Resolution	2,592×1,944 (5 MP)
Frame rate	15 FPS (Maximum)
Pixel Size	H: 2.2 μm, V: 2.2 μm
Focal length	4.8 mm (wide) to 57.6 mm (tele)
Interface	GigE
Supply voltage	11 VDC to 13 VDC or POE: 48 VDC to 56 VDC
Trigger	Software and Hardware
I/Os	Yes
Dimension	H: 29 mm, W: 29 mm, L: 57 mm

Weight	65 g
Shutter	50 µs to 30 s
Gain	0 dB to 15.02 dB
Video Format	Monochrome

Laser scanner

A SICK laser scanner LD-MRS400001S01 (Figure 35) was selected [117] to provide mid-range distance information of the objects. The scanner helps the OD system by contributing the accurate distance measurement in 3D coordinates basing on the Time-of-Flight (ToF) technology and its built-in feature of object tracking. The LD-MRS sensor has the multi-echo capability which allows its use in adverse weather conditions (rain, snow, etc).

Due to the limited range up to 300 meters for highly reflective objects. The laser scanner does not show any practical advantage for real-time long-range obstacle detection however it is an excellent source to provide a precise ground truth distance for short to mid-range datasets.

Figure 35. Laser scanner LD-MRS400001S01 from SICK [117]

In Table 7, some most important features of the SICK LD-MRS laser scanner are mentioned [117].

Table 7. Main features of SICK LD-MRS laser scanner

Specification	
Laser class	1
Field of Application	Outdoor
Horizontal Field-of-View (HFOV)	110°
Vertical Field-of-View (VFOV)	3.2°
Range	0.5 m - 300 m
Max. range with 10 % reflectivity	50 m

Angular resolution	0.125°, 0.25°, 0.5
Scanning frequency	12.5 Hz ... 50 Hz, object tracking at 12.5 Hz
Operating voltage	9 V ... 27 V
Power consumption	8 W
Weight	1 kg
Dimensions (L x W x H)	94 mm x 165 mm x 88 mm
Layers	4
Echoes	3

GPS Sensor

The USB GPS sensor module from Odroid [118] (Figure 36) was used to collect the real-world position of SMART ODS in real-time and further with respect to object GPS coordinates estimate the ground truth distance to the object for dataset preparation of long-range.

Figure 36. USB GPS module from Odroid [118]

Table 8. Main features of the GPS module from Odroid [118]

Specification	
Chipset	Ublox 6010
Interface	USB 2.0
GPS protocol	NMEA 0183 position, velocity, altitude, status and control
Power consumption	100 mA (5 V-)
Dimensions	50x38x16 mm
Tracking sensitivity	-160dBm
Acquisition sensitivity	0.125°, 0.25°, 0.5

3.1.2. Data Collection Experiments

University of Bremen experiments, July 2017:

The first experiments for data collection were performed in July 2017 on-site University of Bremen Campus. The RGB cameras and LiDAR were mounted on a test-stand as shown in Figure 37. Images were captured simultaneously with LiDAR point cloud of various objects moving from 0 to 100 meters including various objects such as pedestrians, bicycles, cars, and bikes. Figure 38 shows some of the collected images.

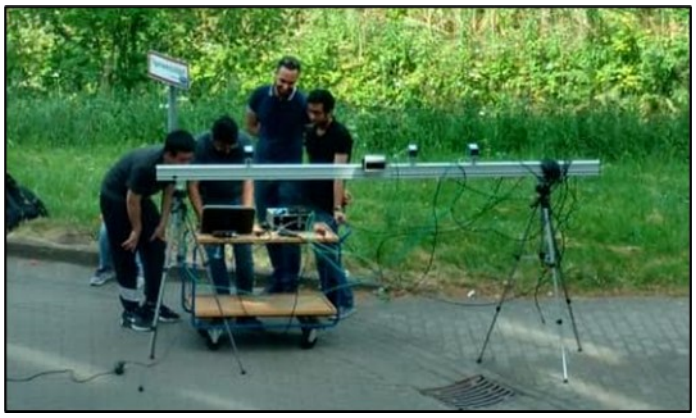

Figure 37. Field tests performed in University Campus. Test-stand with the vision sensors and laser scanner.

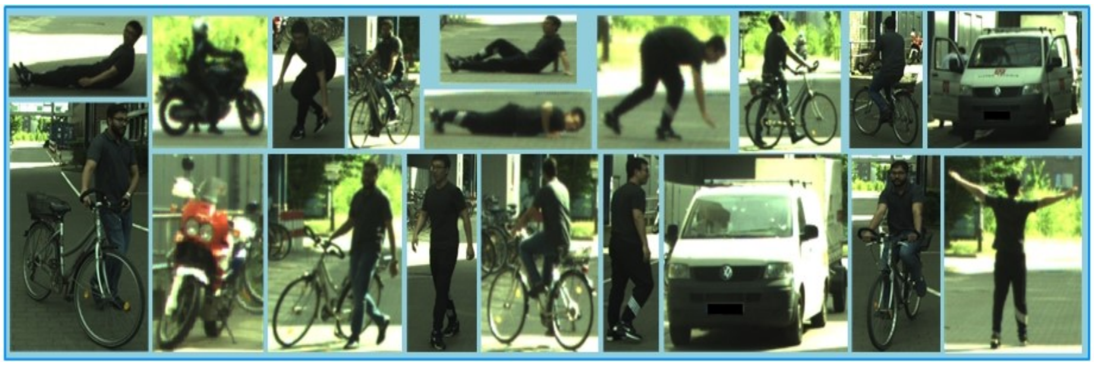

Figure 38. Example images from the experiments at the University of Bremen Campus

Serbian Railways experiments, November 2017-May 2019:

The most extensive set of data collection experiments were performed on Serbia railway tracks in the period November 2017 – May 2019 within the H2020 Shift2Rail project SMART [119]. Two types of experiments were conducted: Static and Dynamic field tests.

In the static experiments, vision sensors were mounted on the static test-stand as shown in Figure 39. The camera images were recorded on the location of the straight rail tracks in the length of about 1100 m in different times of the day and night and in different weather conditions in November 2017, March 2018 and November 2018. During the performed static field tests, for the purpose of dataset generation, members of the SMART team imitated possible obstacles (persons) on the rail tracks in addition to various objects such as bicycles and suitcases located at known distances from the cameras in the range from 0 to 1000 meters.

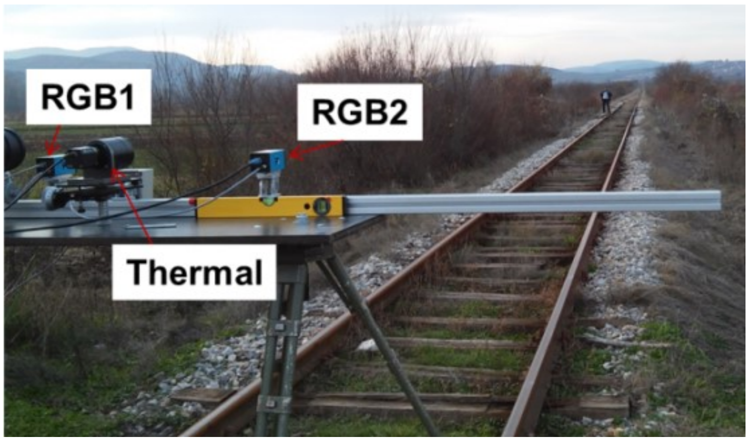

Figure 39. Field tests performed on the straight rail tracks; Test-stand with the vision sensors viewing the rail tracks and an object (person) on the rail track.

In this set of experiments selected LiDAR could not be used as the source of ground truth objects distances due to the limited range of LiDAR. Instead, the ground truth distance was collected manually by indicating the locations on the rail tracks where the objects were located. For example, in the experiments conducted in November 2018, for the purpose of ground truth distance estimation, two persons were walking along the rail tracks 1000 m away from the cameras and back, 1000 m towards the cameras. At every 5 m, while walking in both directions, they signalized in a particular way, so that frames recorded at moments of the signalization could be used for the dataset generation. These camera frames, corresponding to person locations at every 5 meters from 0 to 1000 meters, were extracted from the whole recorded video so that manually drawn bounding boxes of the objects (persons) could be labelled with ground truth distance. The example RGB and Thermal images recorded in static field experiments for the purpose of dataset generation are given in Figure 40.

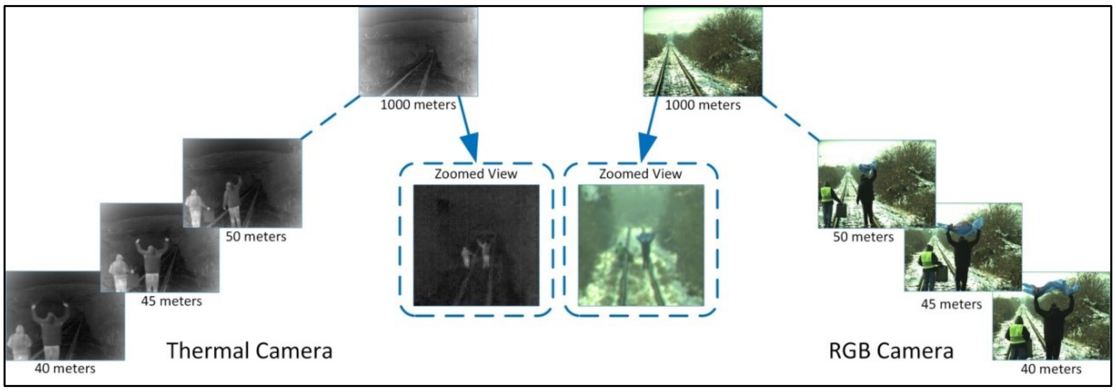

Figure 40. RGB and thermal images recorded in field experiments performed on the long-range straight rail tracks for dataset generation [120]

Dynamic experiments were performed in July 2018 and May 2019. During these experiments, vision sensors were integrated into specially designed protective sensors' housing (as shown in Figure 41), which was mounted onto the moving locomotive Serbia Cargo type 444 pulling the freight train with 21 wagons on the Serbian part of the Pan European Corridor X to Thessaloniki in the length of 120 km with a maximal train speed of 80 km/h. The sensors' housing mounted onto locomotive at the beginning of dynamic experiments is shown in Figure 41. The on-board cameras recorded the data of the real-world rail tracks scenes in front of the locomotive. SMART team members mimicked objects (obstacles) on several crossings along the route according to previously adopted test protocols. During the rest of the tests, as the train was in real traffic, unintended objects were detected along the route. These objects represented possible obstacles, which could cause an accident. The GPS coordinates of the train were recorded simultaneously with cameras' images recording to label ground truth distance. The ground truth object distances were calculated off-line using recorded GPS coordinates of the train and approximate GPS positions of objects on Google Maps calculated using Google maps GPS coordinates of the infrastructure (e.g. crossings) and railway infrastructure information (e.g. distance between pillars).

The Serbian Railways experiments were performed in different illumination conditions including day, night, and dawn as well as in different weather conditions including winter (snow) and summer (38°C environmental temperature). In this way, recorded data formed a dataset of diversity needed for the development of reliable machine learning-based methods for obstacle detection in railways. Some of the images from the dataset are given in Figure 42.

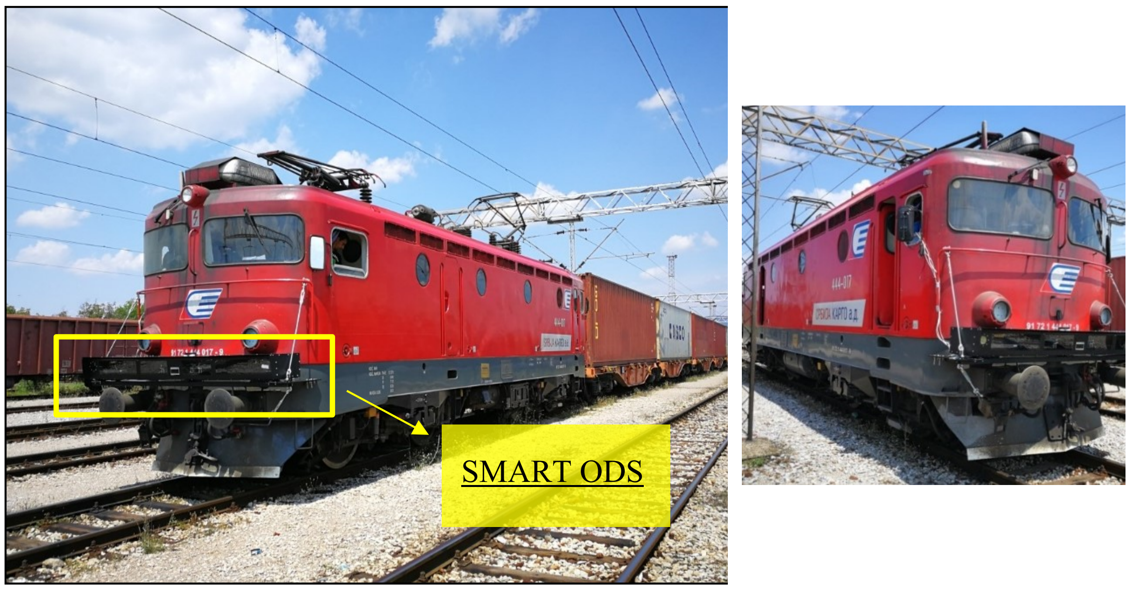

Figure 41. SMART ODS mounted on Serbian freight train during dynamic tests

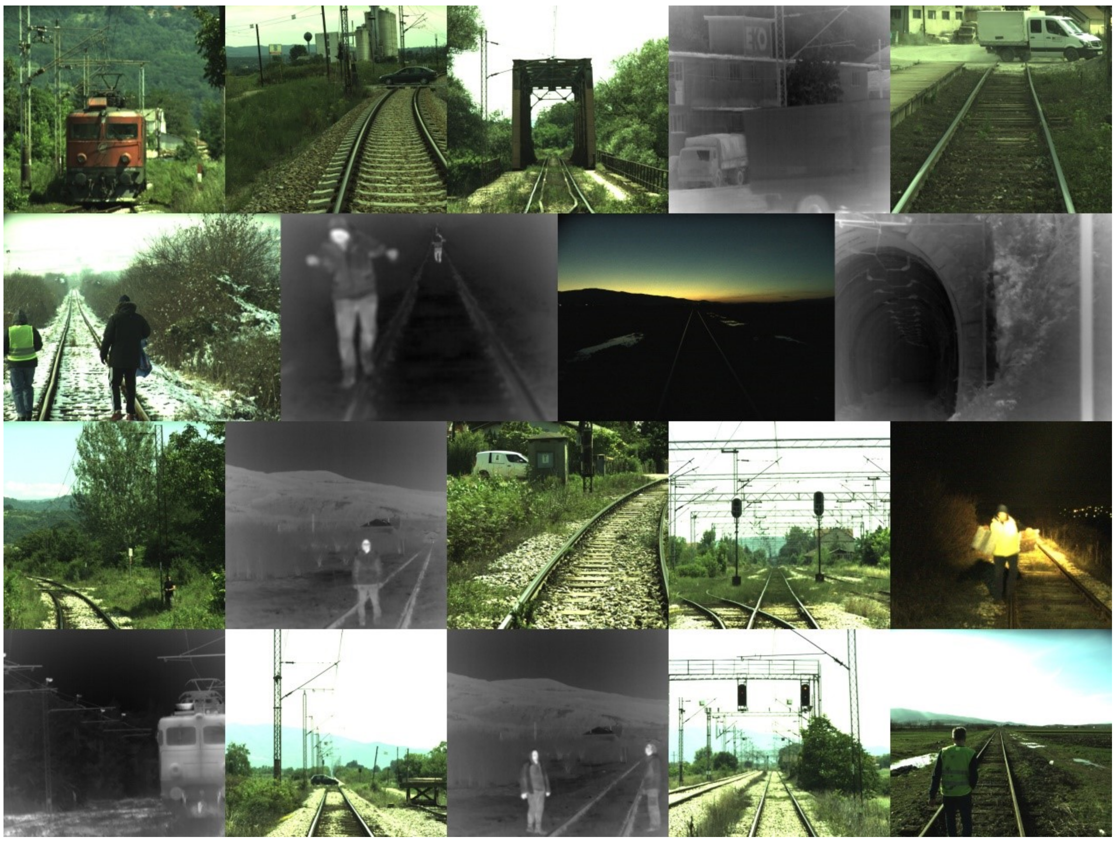

Figure 42. Example images of a real-world scene captured during dynamic experiments

3.1.3. Data Acquisition Procedure

Robot Operating System (ROS) [121] based data acquisition interface was developed that provides services such as hardware abstraction, low-level control, and data passing between different modules. A data acquired from sensors in the form of ROS messages were recorded in ROSBAGS file. The data from each sensor can be accessed by subscribing to a specific ROS topic assigned to a specific sensor. The rosbags were created by subscribing to the ROS topics of specific sensors and storing the data in an efficient file structure in a local memory of the computer.

The asynchronous data recorded from all the sensors were time-synchronized by comparing the timestamps of each sensor's messages and outputs set of messages that were close in the timestamp. Figure 43 shows an example where four sensors are giving data at varying frequencies illustrated as horizontal lines and blue dots represent acquired data over time. The red dots represents data and dotted lines indicate a set of messages that are approximately timely synchronised.

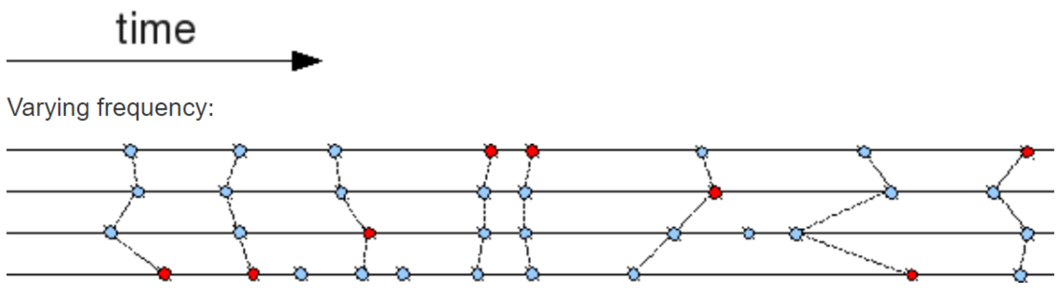

Figure 43. Time approximate synchronization of data at carrying frequency [122]

The sensors synchronisation is needed for multisensory dataset creation to process the data captured by each sensor at the same time event. To be specific, all the sensors provide data at different frequencies and in order to correspond the data from all the sensors, the data synchronization is needed. However, time-approximate synchronisation of data downsamples the data which causes loss of data of high-frequency sensors due to not correspond with data of the low-frequency sensors within the threshold of time approximation.

The asynchronous recorded data shows the random length of samples and can happen that the number of data samples of one sample differs from other sensors. After the synchronisation, the length of data samples becomes the same for all the sensors; hence the data correspond and useable for the dataset labelling stage.

3.1.4 Dataset labelling

Once the sensor data is collected, the camera images are further processed to manually label them with ground truth distance, object bounding box, and object class in an image. The method to manually label dataset is also called "hand-engineering" where a person manually assigns the ground truth to the corresponding input data. The ground truth or expected output can be defined as the desired output from the machine learning model on a given set of inputs.

The recorded images were manually labelled using an annotation tool [123]. The annotation tool helps to create a bounding box around a region in an image where the potential object is, and helps to label the region with ground truth distance and object class as shown in Figure 44. The manually created bounding box coordinates in pixels, the respective image file name, the object class, and distance to the object were recorded and structured in the form of a table. Similarly, the whole set of images, one by one, was labelled and the LRODD dataset was formed. Most images contained multiple objects so that each camera frame consists of multiple objects bounding box information.

It is also important to statement that the LRODD dataset consists of sequential data which means the subsequent frames were labelled to form a sequential dataset. This characteristic of LRODD dataset make it also unique over other datasets since other object detection datasets are built on random images without any temporal relation. The sequential datasets benefit in object tracking as presented in chapter 6.

Table 9 shows the size of the whole LRODD dataset, and here it is also clear that the dataset itself consists of small segments of synchronised images based on a set of cameras used because in some experiments not all the cameras were used to record data. However, the table also shows that the dataset consists of multiple object classes and also shows the distance ground truth measurement method.

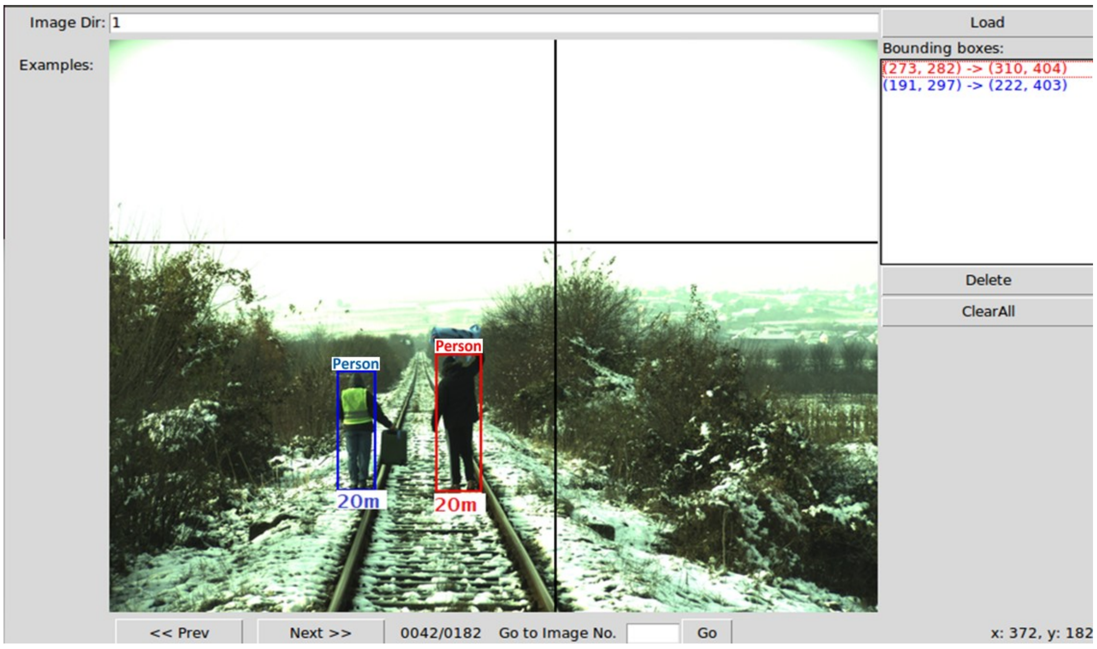

(273, 282) -> (310, 404)
(191, 297) -> (222, 403)

Figure 44. Bounding Box Toolbox for Annotation of Images

However, in the dataset obtained from the experiments, there are few instances for object class bicycle in comparison to person class, hence data augmentation techniques were also considered in order to increase the size and improve the quality of the LRODD dataset for bicycle class. Data was augmented only for the object class *Bicycle*.

The Table 9, shows that in total 136,419 synchronised images were recorded with ground truth distance information and objects instances. Where as around 517,235 are totala number of combined synchronized images from cameras.

Table 9. Long-Range Obstacle Detection and Disance Estimation Dataset (LRODD)

Total Synchronised Images	Synchronised Images		Image Sensors					Ground Truth			Object Classes			
		Distance Range (m)	Cam-01	Cam-02	Cam-03	Night-vision	Thermal	GPS	LIDAR	Manual	Persons	Vehicles	Bicycles	Animals
340,700	68,140	20 – 925	✓	✓	✓	✓	✓	✓	-	✓	✓	✓	✓	-
1008	252	20 – 925	✓	✓	✓	✓	-	-	-	✓	✓	-	-	-
3600	900	20 – 925	✓	✓	✓	-	✓	-	-	✓	✓	-	-	-
43,524	14,508	20 – 925	✓	✓	✓	-	-	-	-	✓	✓	-	-	-
49,221	16,407	20 – 925	✓	-	✓	✓	-	✓	-	-	✓	-	✓	✓
14,034	4,678	20 – 925	✓	-	-	-	✓	-	-	✓	✓	-	-	-
25,088	12,544	20 – 925	-	✓	-	-	✓	-	-	✓	✓	-	-	-
25,880	12,940	20 – 925	-	-	-	✓	✓	-	-	✓	✓	-	-	-
7660	3,830	20 – 925	-	✓	✓	-	-	-	-	-	✓	✓	✓	-
280	140	20 – 925	✓	✓	-	-	-	-	-	-	✓	✓	-	-
6240	2080	20 - 140	✓	✓	✓	-	-	-	✓	✓	✓	✓	✓	✓
=517,235	=136,419													

3.2 Data Augmentation

The data augmentation techniques were applied to improve the LRODD dataset extracted from real-world images. In the original dataset, the instances of objects such as bicycle or vehicles other than persons were very few for the long-range distances. The proposed object augmentation technique allows augmenting objects in an image by placing it in an image with random rotations and scale also considering the object projection on image plane with respect to change in distance. Figure 45 presents the flow chart for the dataset augmentation.

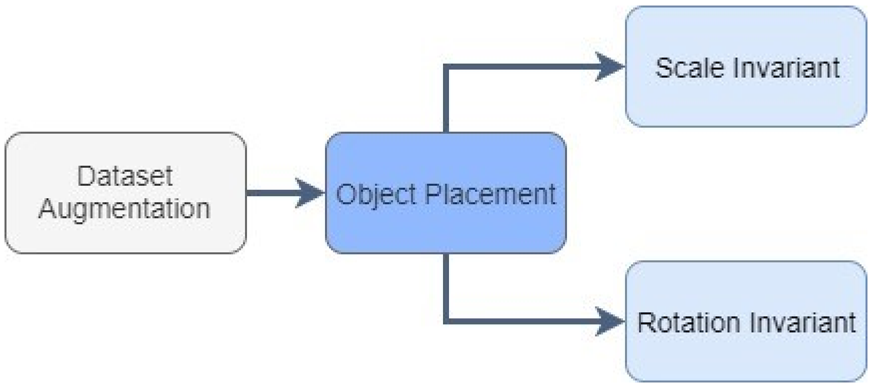

Figure 45. Flow Chart for Dataset Augmentation

An object class *Bicycle* was chosen to increase images in dataset with augemented bicycle. A bicycle was overlaid on the images in different sizes relative to distance. First, the relation between the average size of bicycle appearances in an image with respect to change in distance to the camera was approximated. It was needed to map the real-size object to 2D image that can be calculated by projective transformation. The geometry of the bicycle in the real-world and the size of the bicycle in pixels in multiple images taken at various known distances. By doing so the factor k by which the bicycle size in image change with respect to change in distance was found.

$$Size\ of\ object\ in\ Image \propto \frac{k}{Distance\ to\ object}$$

Using the factor the bicycle was placed at different scales on an image from the original dataset with known ground truth distance from 0 to 1000 meters. An example of augmented images is given in Figure 46.

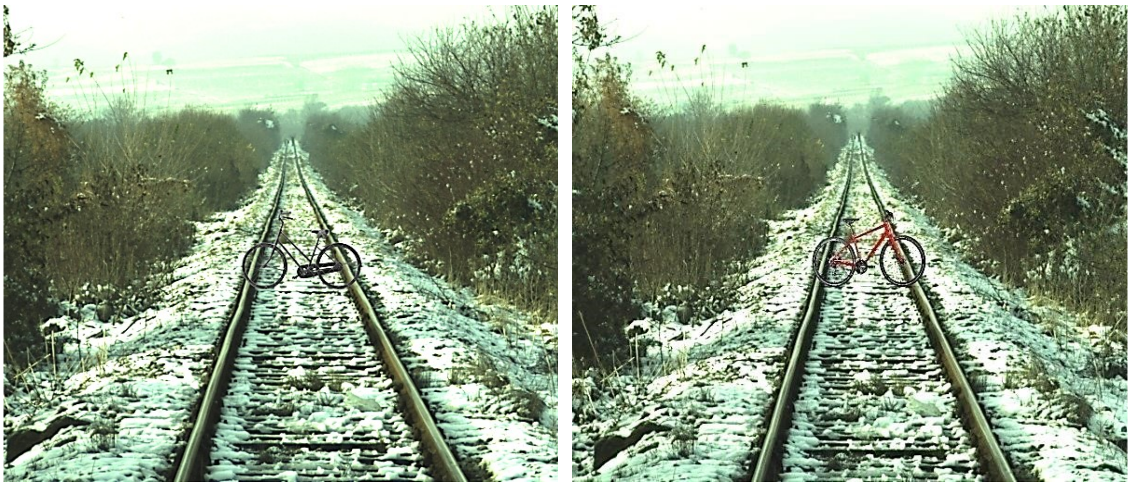

Figure 46. Black bicycle overlaid at 60 m (left). Red bike rotated by 180 degrees overlaid at 60 m (right)

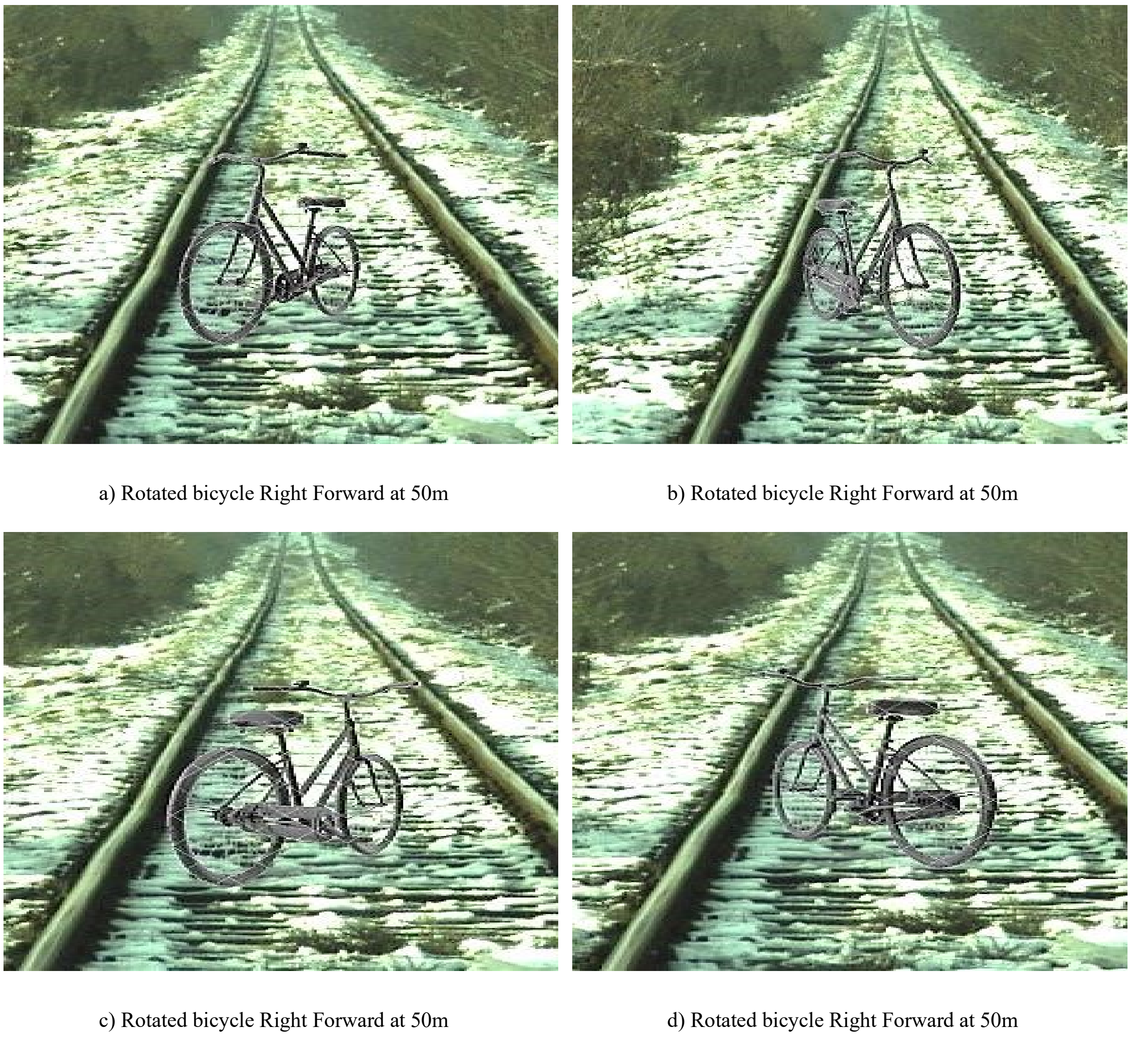

a) Rotated bicycle Right Forward at 50m

b) Rotated bicycle Right Forward at 50m

c) Rotated bicycle Right Forward at 50m

d) Rotated bicycle Right Forward at 50m

Figure 47. Augmentation Example of a Bicycle

To diversify and add more data, the bicycle was placed at each 45-degree angle shift with respect to the camera. Hence for each 5 meters interval, the five samples were formed as follows, bicycle without rotation and four samples with a rotation of 45, 135, 225, and 315 degrees. Figure 47 illustrates the bicycle placement at various angles at 50 meters ground truth. The images are zoomed for clarity. Table 10 shows the augmented bicycle images in total. The augmentation techniques were only applied on two RGB camera images and Table 10 shows the total addition in the dataset for the object class bicycle with long-range ground distances.

Table 10. Augmented Data through Object Placement

	Reference Camera	Rescaled	Rotated	Total Augemented
Bicycles	CAM01	364	728	1092
	CAM02	410	820	1230
Combined	-	774	1548	2322

The Table 10. Shows that total 2322 augmented images were added into original LRODD dataset. The augmentation was done by varying scale and rotation of object overlaid in image. The scale and rotation augmentation improve the performance of ML models to detect bicycle from different angles and appearance in real-time captured images.

4. A machine learning-based distance estimation from a single camera

A single camera-based distance estimation to the object is a very challenging task and up to now, this topic is not explored considerably. In this chapter, two novel object distance estimation methods from a single camera are presented. The first proposed method named DisNet (Distance Network) has been presented by Haseeb et al. in [124] and in [125]. The method estimates the distance of the objects detected by the object detector. DisNet makes use of features extracted from the objects bounding box and object class type, to estimate the distance to the detected objects. The method can be used with any object detector that outputs object bounding box and object class. However, in this work, a state-of-art object detector namely You Only Look Once (YOLO) has been used.

The second proposed method is named YOLO-D. It is another approach to estimate distance to the detected object by modifying the architecture of the YOLO object detection model, a deep learning network. In this method, the modified architecture of YOLO predicts the distance to the detected object besides its primary function of the object bounding box and class prediction.

4.1 DisNet: a machine learning-based object-specific distance estimation from a single camera

In this thesis, the very first method DisNet that estimates the distance based on bounding box information of detected objects is presented. Any object detector that outputs object bounding box and class in an image such as YOLO, fast RCNN, MaskNet can be used with DisNet to estimate the distance to the detected objects.

During the development of DisNet, YOLOv3 is considered as an object detector to obtain an object bounding box and class.

The architecture of the DisNet-based distance estimation system is illustrated in Figure 48. The main blocks are YOLO based object detection, feature extraction, and DisNet.

The camera image is input to the Object Detector which is based on a state-of-the-art computer vision object detector YOLO (You Only Look Once) [70] pre-trained with the COCO object detection dataset [89]. YOLO is a fast and accurate object detector based on Convolution Neural Network (CNN) as explained in chapter 2. Its outputs are bounding boxes of detected objects in the image and labels of the classes detected objects belong. The objects bounding boxes resulted from the YOLO object detector are then processed further to calculate the features, bounding boxes parameters. Based on the input features, the trained DisNet gives as outputs the estimated distance of the object to the camera sensor. In the system architecture illustrated in Figure 48, an example of the estimation of distances of two persons on the rail tracks is shown.

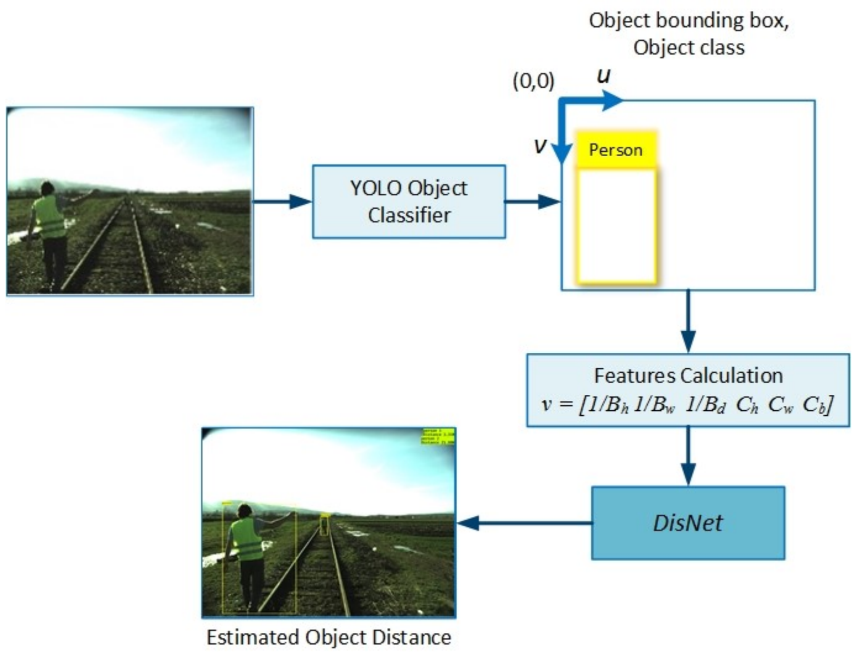

Figure 48. The DisNet -based system used for object distance estimation from a monocular camera [89]

For the training of DisNet, a supervised learning technique was used. This method required a collected dataset including both inputs and outputs, i.e. the ground truth. In the presented system, a set of LRODD dataset was used to train the DisNet model.

The set of LRODD dataset used to train DisNet contains in total 2000 samples of the object classes person, bicycle, and vehicles for the distance range of 0 to 70 meters. The details of the structure and training of DisNet are given in the following sections.

4.1.1 Feature Extraction

In the presented work, the objective is that DisNet is trained for the estimation of an object's distance to the onboard sensory obstacle detection system. More formally, the task is to estimate the distance to an object in the laser's reference frame, which is on the same distance from the object as the camera reference frame, given an input also called feature vector $\boldsymbol{v}$. In the presented work, $\boldsymbol{v}$ contains the features of the bounding box of the object detected in camera images and the ground-truth is the distance to the object as measured by the laser scanner. Some of the objects recorded at different distances and their bounding boxes from the dataset are shown in Figure 49.

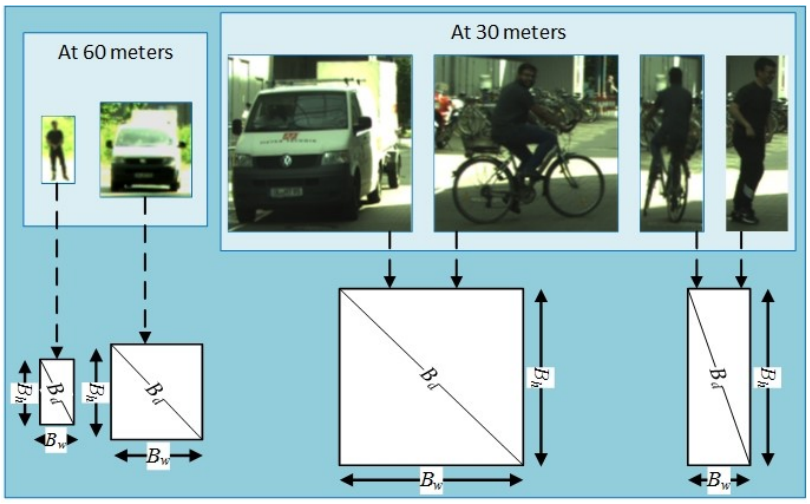

Figure 49. Example of some objects bounding boxes at various distances

For each extracted object bounding box, a six-dimensional feature vector $\boldsymbol{v}$ was calculated:

$$\boldsymbol{v} = [1/B_h \; 1/B_w \; 1/B_d \; C_h \; C_w \; C_b] \tag{4-1}$$

where the coordinates of vector $\boldsymbol{v}$, features, are:

Height, B_h=(height of the object bounding box in pixels/image height in pixels)

Width, B_w=(width of the object bounding box in pixels/image width in pixels)

Diagonal, B_d=(diagonal of the object bounding box in pixels/image diagonal in pixels)

The ratios of the object bounding box dimensions to the image dimensions B_h, B_w, and B_d enable the reusability of the DisNet trained model with a variety of cameras independent of image resolution. C_h, C_w, and C_b in (4-1) are the values of average height, width, and breadth of an object of the particular class. For example for the class "person" C_h, C_w and C_b are respectively 175 cm, 55 cm, and 30 cm, and for the class "vehicle" 160 cm, 180 cm, and 400. The features C_h, C_w, and C_b are assigned to objects labelled by YOLO detector as belonging to the particular class in order to complement 2D information on object bounding boxes and so to give more information to distinguish different objects.

The relationships of the calculated features of object bounding boxes in the 2D image, B_h, B_w, and B_d, and the real distance to the image measured by laser scanner in the range 0-70 m, are given in Figure 49. Geometrically, by the projective transformations, the object bounding box size is expected to get smaller the further away the object is, so the inverse of bounding box size is expected to increase as the distance increases. Inspection of the data confirms that this is the case and suggests that the relationship is approximately linear, which gives a clear motive to use it for the dataset used for the training of DisNet.

Table 11. Correlation between the extracted features with distance

Attributes	Width	Height	Diagonal	1/Width	1/Height	1/Diagonal
Distance	-0.630	-0.682	-0.693	0.805	0.769	0.953

Table 11 and Figure 50 also show that the inverse relation of bounding box height, width, and diagonal highly correlate with distance, thus the inverse was selected for DisNet.

4.1.2 DisNet architecture and training

In order to find the appropriate number of hidden layers experiments with various numbers of hidden layers (1, 2, 3, 5, and 10) were performed assuming that each hidden layer had 100 neurons. Figure 51 (a) shows the accuracy of distance estimation over 1000 epochs achieved for the different number of hidden layers. As obvious, DisNet with one hidden layer achieves the lowest distance estimation accuracy. It is also apparent that there is no significant difference in distance estimation accuracy achieved with 2, 3, 5 and 10 hidden layers. For this analysis, a reduced dataset was used. The networks were trained on the 80% dataset and the estimation accuracy reported is on the 10% validation set.

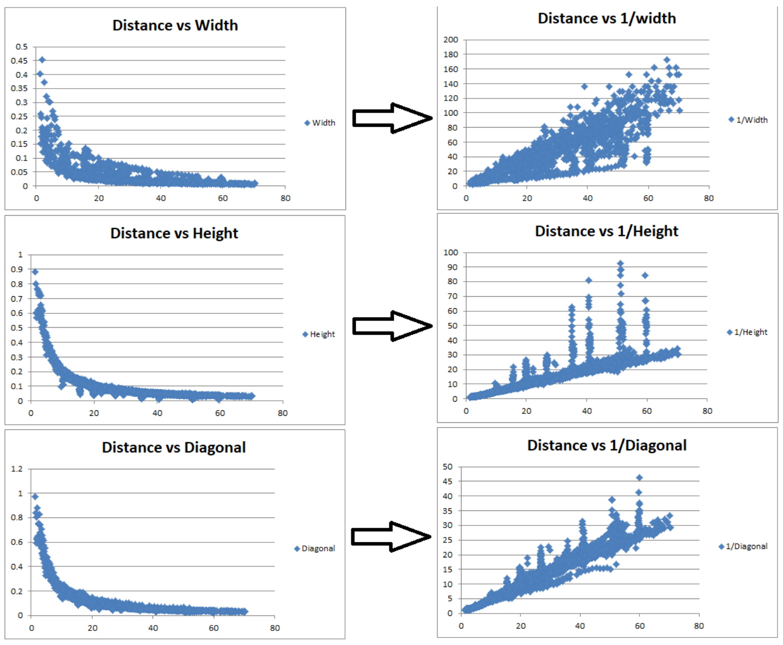

Figure 50. Distance vs inverse and non-inverse bounding box features

Similar behaviour can also be seen in Figure 51(b) where the Mean Absolute Error over 1000 epochs achieved for a different number of hidden layers is shown. As obvious, the Mean Absolute Error is most significant for the DisNet with one hidden layer, while there is no significant difference in the Error achieved with 2, 3, 5 and 10 hidden layers.

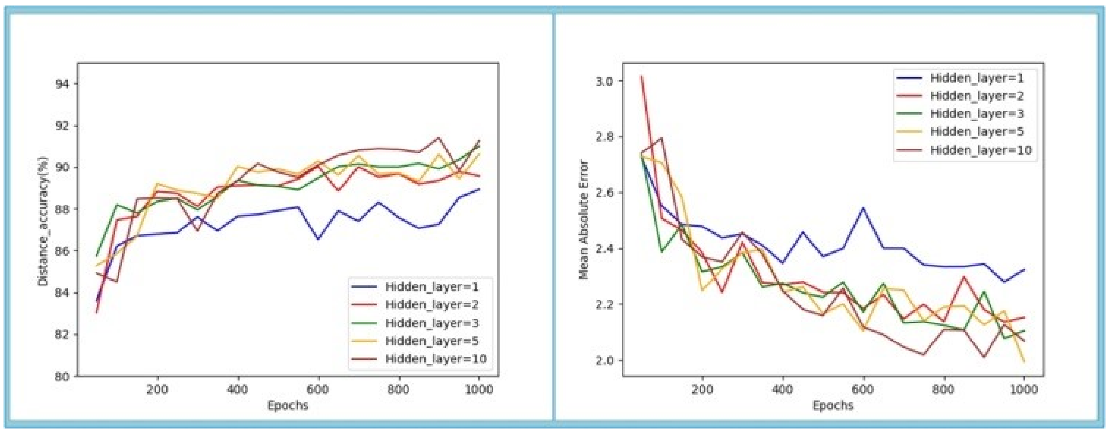

(a) (b)

Figure 51. (a) Distance Estimation Accuracy and (b) Mean Absolute Error achieved for different numbers of hidden layers

Even though the smallest values of Mean Absolute Error were achieved for 10 hidden layers and the distance accuracy was highest for 10 hidden layers, a trade-off was made between the computational time and accuracy/error and finally, DisNet with 3 hidden layers was chosen.

After deciding on the network with 3 hidden layers, in order to find the appropriate number of neurons for the hidden layers experiments with various numbers of hidden neurons were performed. Figure 52(a) shows the accuracy of distance estimation over 1000 epochs achieved for the different number of neurons per hidden layer. As obvious, the distance estimation accuracy achieved with 10 hidden neurons is very low, much lower than distance estimation accuracy achieved with 30, 100 and 200 hidden neurons. The magnified diagram in Figure 52 (b) shows that distance estimation accuracy with 30 hidden neurons is lower than with 100 and 200 neurons. Bearing in mind that there is no significant difference in distance accuracy estimation with 100 and 200 hidden neurons, in order to reduce the complexity of DisNet, finally, 100 neurons per hidden layer were chosen.

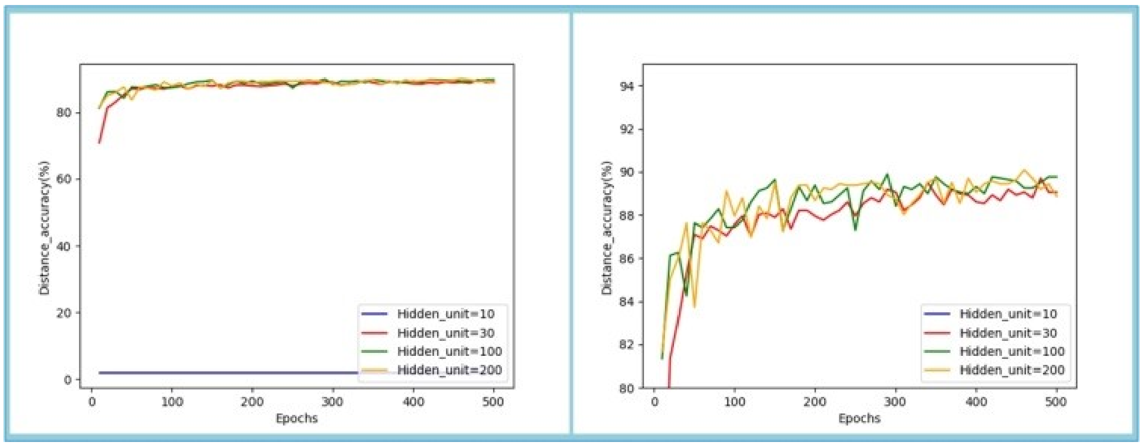

(a) (b)

Figure 52. Distance Estimation Accuracy achieved for different number of hidden neurons per hidden layer in 3-hidden layers neural network DisNet

The final structure of DisNet having 3 hidden layers with 100 hidden neurons per layer is shown in Figure 53.

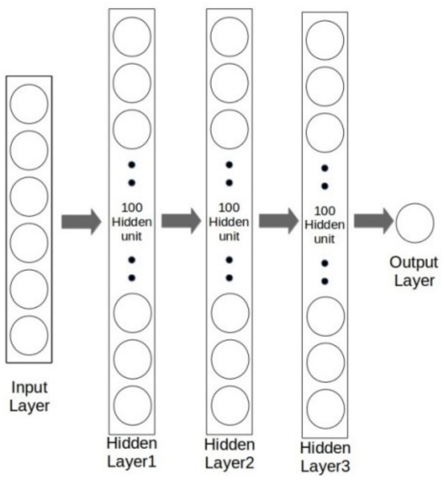

Figure 53. The structure of DisNet used for object distance prediction

DisNet input layer consists of 6 neurons corresponding to 6 features, parameters of output layer consists of only one single neuron. The output of this node is the estimated distance between the camera and the object viewed with the camera.

For training the network the input dataset was firstly randomly split into a training set (80% of the data), validation set (10% of the data), and test set (10% of the data). The DisNet was trained using the backpropagation method with Adam optimizer [16] to minimize the Mean Absolute Error (MAE) loss function for distance estimation give in equation 4-2, in which y_i refer to estimated distance and $\widehat{y_i}$ refer to ground-truth distance.

$$MAE = \frac{1}{n}\sum_{i=1}^{n}|y_i - \widehat{y_i}| \tag{4-2}$$

Scikit-Learn's GridSearchCV [126] hyperparameters tuning technique was used to fine-tune the hyperparameters of our model. The combinations of hyperparameters were given to Gridsearch and it evaluates the performance on all possible combinations and gave the best configuration of parameters. To find the best combination, the following set of hyperparameters was given:

- Optimizers = adam [127], rmsprop [128]
- Weights initializer [129] = glorot_uniform, glorot_normal, he_normal
- Batch size = 25, 50, 100
- learning rate = 0.001, 0.0001, 0.00001
- Number of layers = 1, 2, 3, 5, 10

- Number of hidden units = 10, 30, 100, 200
- Activation function = relu, elu, selu

The best combination of parameters was selected for DisNet given by GridSearch method of hyperparameters tuning: SELU (Scaled Exponential Linear Unit) activation function, batch size of 50, epochs 1000 with early stopping technique, uniform weights initialization, and learning rate of 0.001.

4.1.3. Performance Evaluation

For the evaluation purpose, the performance of DisNet was measured on the test dataset by measuring the Mean Absolute Error (MAE) and Accuracy is computed by the equation (4-3). Figure 54, shows that the DisNet, distance estimation is close to the actual distance. The DisNet accuracy is measured with the tolerance criteria which means the estimation with less than 5 meters error is considered as an accurate measurement.

$$Accuracy = \frac{1}{n}\sum_{i=1}^{n}(|distance_{true} - distance_{estimated}| < 5) \qquad (4\text{-}3)$$

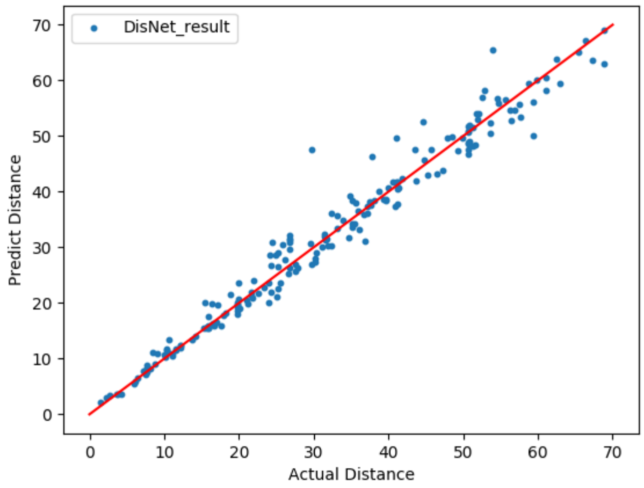

Figure 54. the distance estimation vs ground truth distance

Furthermore, for the sake of performance evaluation, some popular neural network models were also compared with the DisNet model, trained on the same set of datasets as DisNet. The bar diagram in Figure 55, shows the comparison of DisNet with linear regression model [130], lasso regression model [131], Gaussian RBF kernel Models

[132], and support vector machine with linear kernel [133], respectively. The accuracy of each model is shown in Figure 55. The straight lines on top of each bar represent error bars and indicate the error or uncertainty in a reported measurement. The standard error of the mean (SEM) [134] of each model is 4.25, 4.52, 3.91, 6.24, 1.90 respectively. The test accuracy of the DisNet model achieves 94.5% and Mean Absolute Error loss 1.90 with a 753 training epoch using the early stop method.

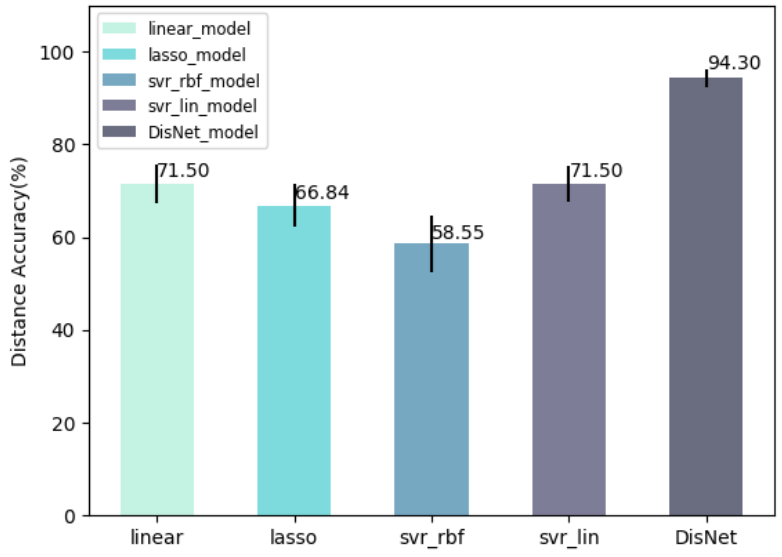

Figure 55. Distance accuracy of DisNet vs other models

The performance of DisNet on unseen data has also been evaluated. The DisNet-based system for distance estimation was evaluated on two different scenarios, the railway scene, and the road scene. The next section is divided into two sub-sections, namely static and dynamic experiments. The static experiments section contains results of the railway scene where the SMART ODS system was placed at a fixed position while objects were moving. Whereas, in dynamic experiments, the section contains results from railway and road scene while both the camera and the objects were moving simultaneously. The images recorded in the field tests within the H2020 Shift2Rail project SMART [119] were used for railway scene evaluation. The details of SMART ODS are given in section 3.1.

4.1.3.1. Static Experiments

The sensor data, which were used for the evaluation of a DisNet-based system for object distance estimation, were recorded in the field tests on the straight rail tracks at different times of the day and night on the location of the straight rail tracks (Figure 39 – Section 3.1.2). Monocular RGB cameras, thermal and night vision camera were mounted on the static test-stand, together with the laser scanner in the locations which resemble their intended locations in the dynamic obstacle detection experiments (Figure 39 – Section 3.1.2). During the performed field tests, the members of the SMART Consortium imitated potential static obstacles on the rail tracks located on different distances from the test-stand.In this section, some results of DisNet on RGB, thermal, and night vision images were taken at different weather and illumination conditions covering short, mid, and long-range are presented.

Distance estimation from single RGB camera images

Some of the results of the *DisNet* objects (persons) recognition and distance estimation from RGB images are given in Figure 56 and Figure 57. The estimated distances are also given in Table 12.

Table 12. Estimated distances from RGB images vs. ground truth

Figure	Object	Rail Scene		
		Ground Truth	Distance estimated from DisNet	Error
Figure 56	Person 1	100 m	101.89 m	1.89%
	Person 2		99.44 m	0.6%
Figure 57	Person 1	50 m	54.26 m	8.52%
	Person 2	150 m	167.59 m	11.726%
	Person 3	100 m	132.26 m	32.26%
	Person 4	300 m	338.51 m	12.836%
Figure 58	Person 1	835 m	826.90 m	0.97%
	Person 2		849.57 m	1.74%

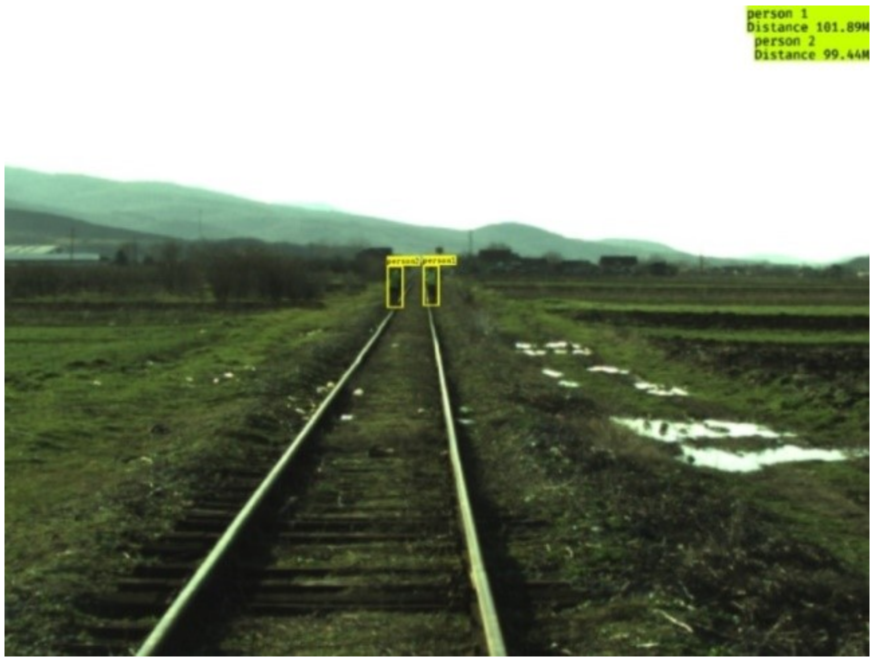

Figure 56. *DisNet* estimation of distances to objects in a rail track scene from the RGB camera image. Distance estimation of detected persons at 100 m

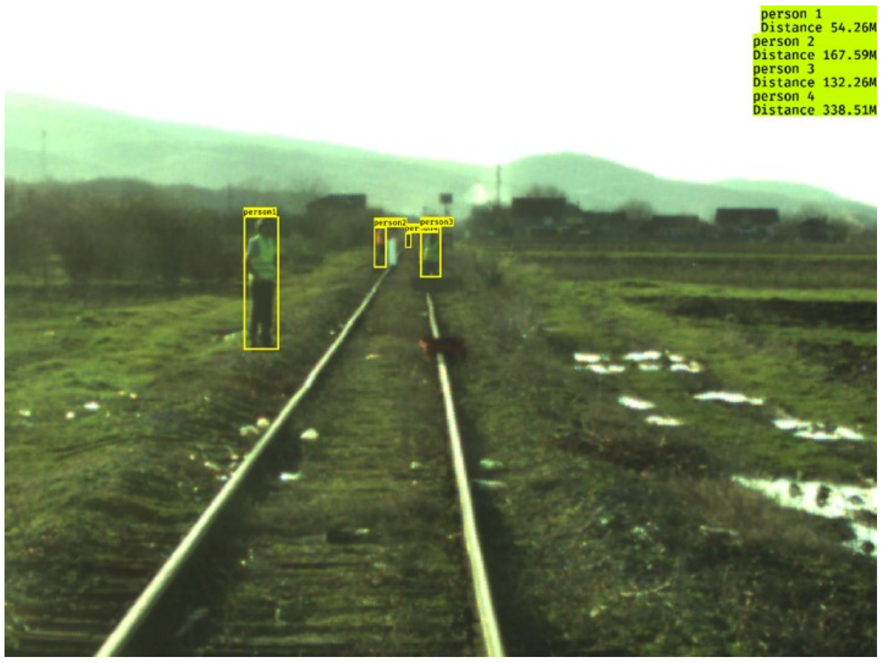

Figure 57. *DisNet* estimation of distances to objects in a rail track scene from the RGB camera image. Magnified RGB image overlaid with bounding boxes and distance estimation of detected persons at 50, 100, 150, and 300 m respectively.

As evident from Figure 56 and Figure 57, YOLO based object detection in images is reliable even though the YOLO detector was used in its original form trained with the COCO dataset, without re-training with the images from the SMART field tests. Also, it is obvious that achieved distance estimation is satisfactory in spite of the fact that the *DisNet* database did not contain object boxes from the real rail tracks scenes. This, in the first place, means that the objects in real field test scenes were at larger distances from the sensors than in the recording tests used for dataset generation. Also, the distances of the objects in field tests were outside the laser scanner range (0 m – 60 m) used for the training of *DisNet*. However, the difference in the estimation of distances of persons at 100 m (Figure 57) indicates the need for overcoming the problem of bounding box extraction inaccuracy.

As per the requirement of long-range obstacle detection for railways, the DisNet successfully able to estimate the distance to the distant objects. The results shown in Figure 58 prove that DisNet can precisely estimate the distance to the object regardless of how far it is from the camera, if it is detected by the object detector.

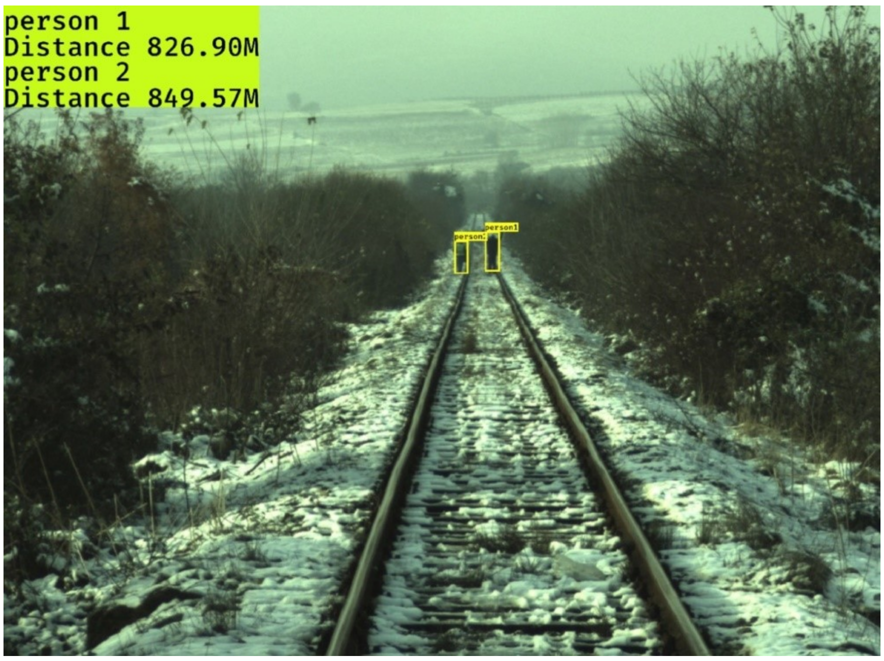

Figure 58. Object detection and distance estimation in RGB camera image recorded in winter (snow) environmental conditions; Ground truth distance: 835 m (0,97 % and 1,74% respectively).

Distance estimation from thermal camera images

Another advantage of DisNet is that it can work with any type of camera. DisNet originally is trained with bounding box features extracted by RGB images. Besides RGB camera, the performance was also evaluated on thermal and night vision cameras. Some of the results of the DisNet object distance estimation in thermal camera images of the same scenes as in Figure 56 and Figure 57 are given in Figure 59 and Figure 60. The estimated distances are also given in Table 28.

Table 13. Estimated distances from thermal image vs. ground truth

Figure	Object	Rail Scene		
		Ground Truth	Distance estimated from DisNet	Error
Figure 59	Person 1	100 m	101.06 m	1.06%
	Person 2		100.10 m	0.1%
Figure 60	Person 1	50 m	48.36 m	3.28%
	Person 2	150 m	157.02 m	4.68%
	Person 3	100 m	161.02 m	61.02%
	Person 4	500 m	469.94 m	6.012%

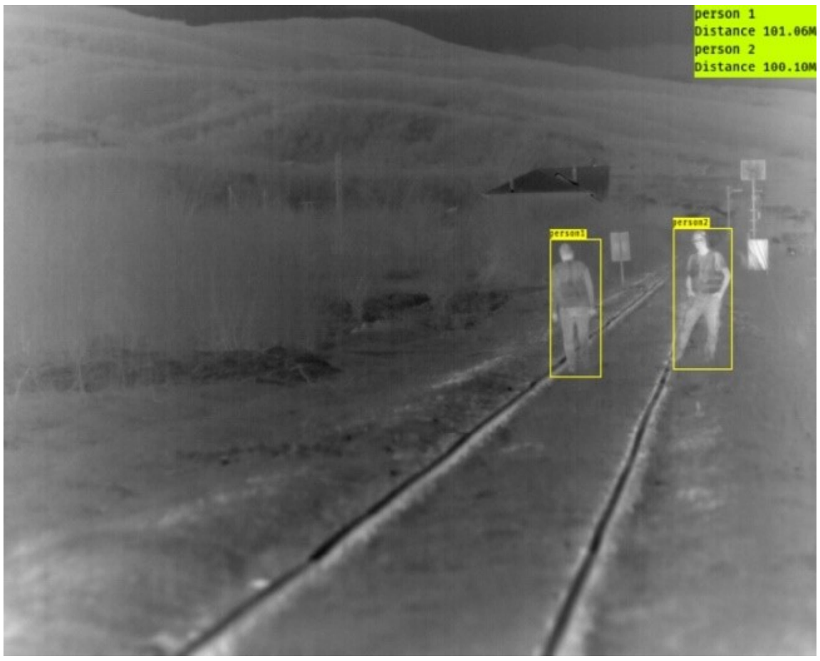

Figure 59. *DisNet* estimation of distances to objects in a rail track scene from the thermal images. Distance estimation of detected persons at 100 m

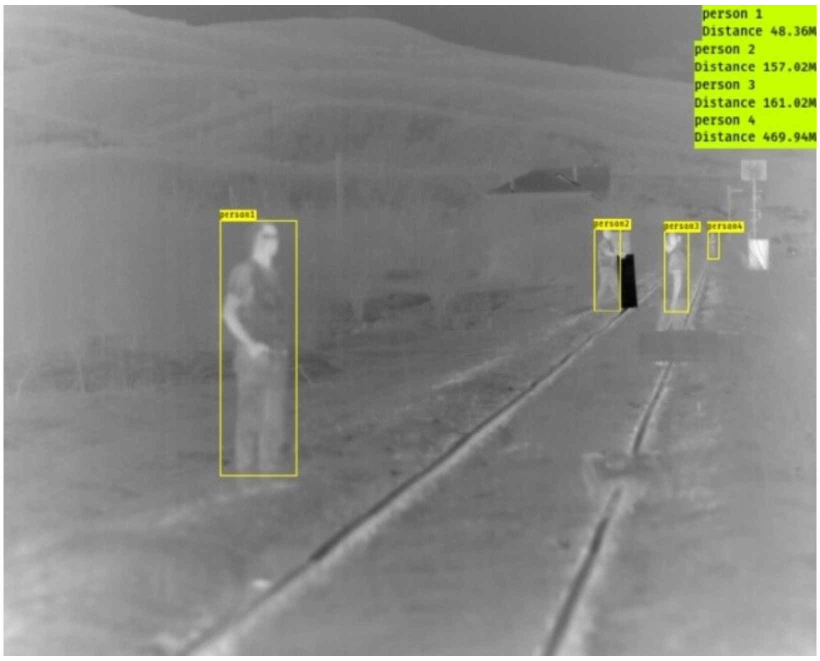

Figure 60. ***DisNet*** **estimation of distances to objects in a rail track scene from the thermal images. Distance estimation of detected persons at 50, 100, 150 and 500 m respectively**

As obvious from Figure 59 and Figure 60, YOLO based object detection in images is reliable in spite of the fact that the YOLO classifier was used in its original form based on RGB images from the COCO dataset, without re-training with the thermal camera images. Moreover, it is obvious that achieved distance estimation is satisfactory in spite of the fact that *DisNet* database did not contain object bounding boxes from the images of rail tracks scenes, both either RGB or thermal camera images. Also, it is obvious that long-range object distance estimation (500 m) was achieved with satisfactory accuracy in spite of the fact that distances of the objects in the field tests were much outside the laser scanner range (0 m – 60 m) used for the training of *DisNet*. However, due to inaccuracy in bounding boxes extraction, there are more significant errors in some estimation results, i.e. for 100 m estimation in Figure 60. This indicates the need for a method to overcome the problem of uncertainty in single cameras object detection. Moreover, the results of object detection and distance estimation from two cameras, RGB and thermal show the advantages of multiple viewing angles due to different positioning of cameras on the test-stand. The multiple perspectives assist to detect the person at 300 m in RGB image, which cannot be seen in the thermal image view due to its position behind the person at 500 m. Similarly, a person at 500 m can be seen in the thermal image, but not in the RGB image. A machine learning-based method for distance estimation from multiple cameras, which overcome the mentioned problems of distance estimation from monocular cameras is given in detail in Chapter 5.

Distance estimation from night vision camera images

Figure 61 shows the results obtained on the night vision image were two persons walking at a 225-meter distance from the camera. Table 14 shows the estimated distances from the night vision images and the ground truth.

Table 14. Estimated distances from Night Vision images vs. ground truth

Object	Railway Scene		
	Ground Truth	Distance estimated by DisNet	Error
Person 1	225 m	225.93 m	0.413%
Person 2		237.23 m	5.435%

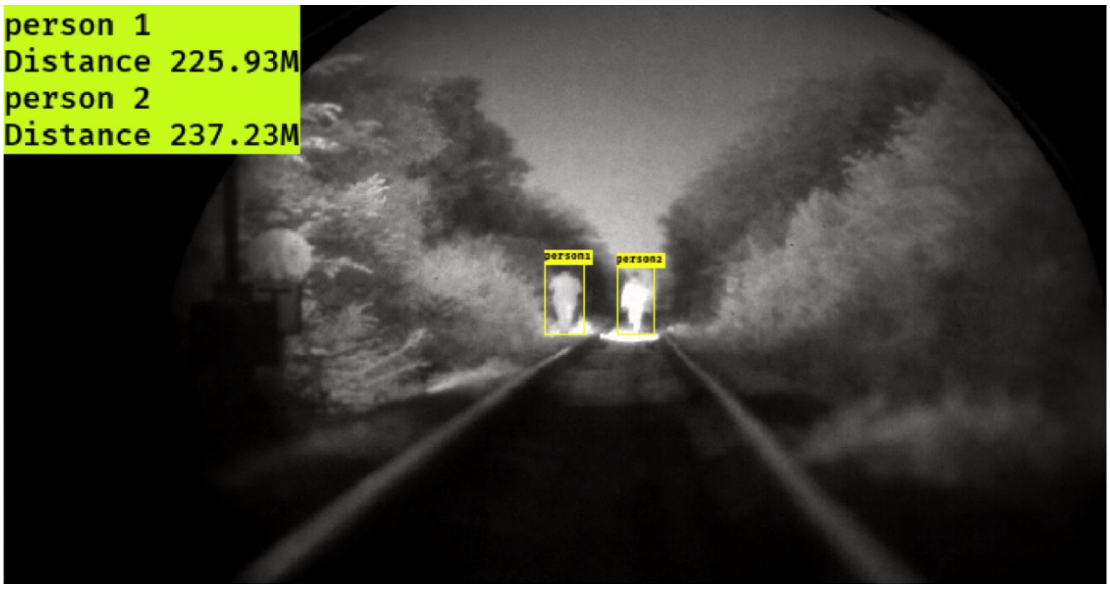

Figure 61. *DisNet* estimation of distances to objects in a rail track scene from the night vision images.

4.1.3.2. Dynamic Experiments

Railway Scene

For all dynamic tests of SMART ODS, the OD demonstrator was mounted onto the test locomotives. The test length was 120 km, the average speed was 34 km/h and the run on the whole length lasted 3.5 h. On the straight rail-tracks sections, between Niš Marshalling Yard and station Grdelica, the maximal speed was 80 km/h.

Similar to Static experiments, SMART team members mimicked objects (obstacles) on two crossings along the route according to previously adopted test protocols. During the rest of the test, as the train was in real traffic, accidental objects were detected along the route. These objects represented possible obstacles, which could cause an accident, for example, a truck crossing the unsecured crossing at the station while the train was approaching.

Some of the results of the DisNet based distance calculation with RGB cameras are shown in Figure 62. Figure 62 (a)-(d) show four subsequent frames of the RGB camera video in which two persons crossing the track are recognized out of which one person is pushing the bike, which also was recognized. The person and the bike were recognized though they are not on the same track as the train. As can be seen from Figure 62, a person without the bike, who is crossing the rail track, in four subsequent frames was recognized at distances 121,74 m, 114,16 m, 86,37 m, and 81,71 m as opposed to ground truth distances of 120.12 m, 111.95 m, 83.66 m, and 80.62 m respectively. The ground truth distances were calculated using GPS coordinates of the train, Google maps GPS coordinates (e.g. crossing), and railway infrastructure information (e.g. distance between pillars).

Table 15. Long-range distance estimation

Object	Railway Scene		
	Ground Truth	Distance estimated by DisNet	Error
Person	120.12 m	121.74 m	1.34%
	111.95 m	114.16 m	1.97%
	83.66 m	86.37 m	3.23%
	80.62 m	81.71 m	1.35%

Due to the geometry of the rail tracks in dynamic tests, there were no straight rail tracks sections longer than 600 m on which accidental objects could be detected. However, Mid- to Long-range results of about 200 m - 600 m were achieved as illustrated in Figure 63-66, from RGB, thermal and night vision camera. Static tests were performed in November 2018 on the straight rail tracks in the length of about 1000 m, with the planned (mimicked objects) on the whole length, complementing so dynamic tests (a result shown in Figure 57). Due to the positive results achieved in static field tests, similar performance is expected to be achieved in operational conditions as well.

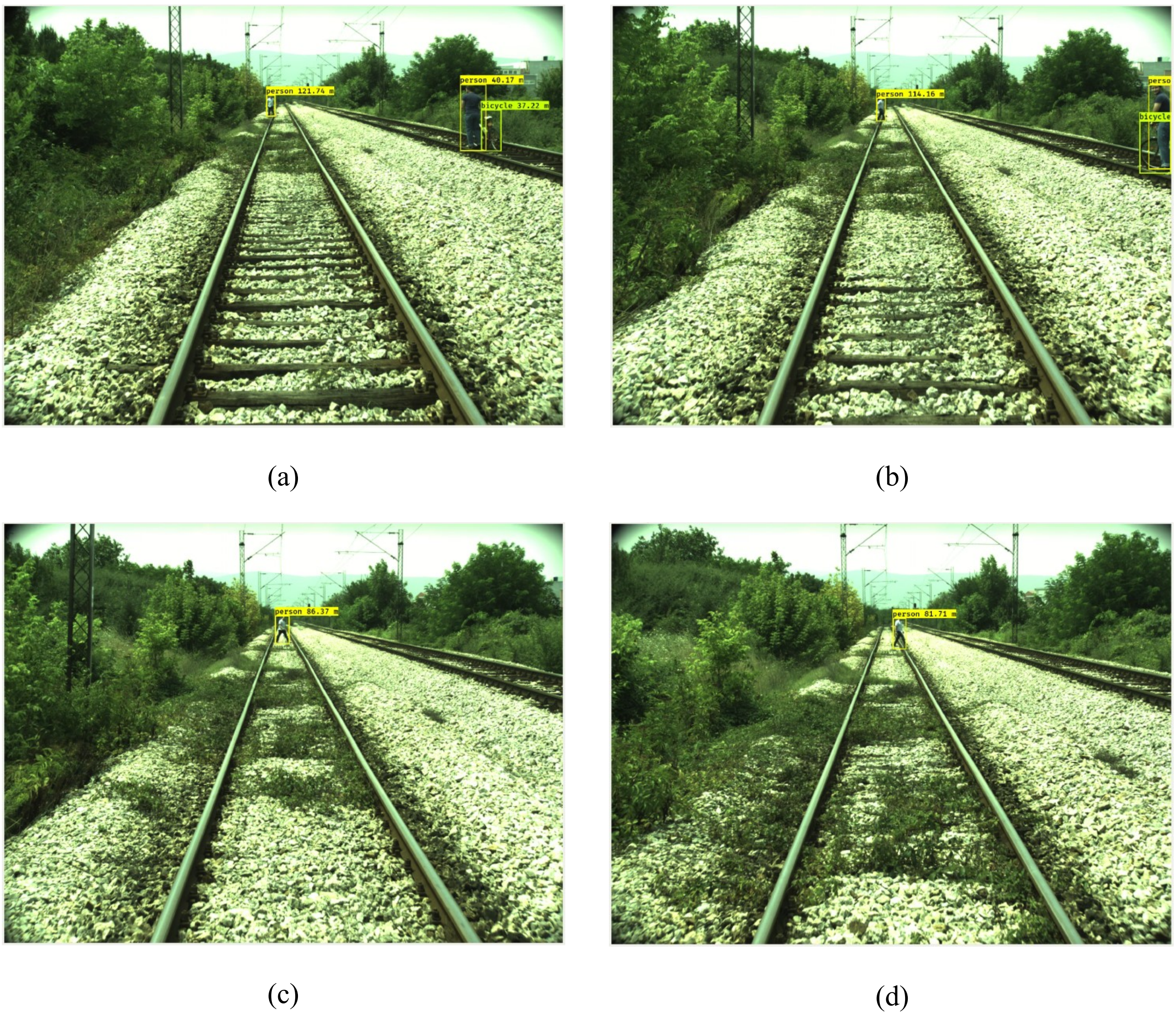

Figure 62. Four subsequent frames of the RGB camera video overlaid with the bounding boxes of the detected objects as well as with the estimated distances from the locomotive to the objects

Table 16. Long-range distance estimation for RGB, Thermal and Night Vision Images

Figure	Object	Rail Scene		
		Ground Truth	Distance estimated from DisNet	Error
Figure 63	Person 1	272.75 m	245.02 m	10%
Figure 64	Person 1	231.97 m	253.65 m	8.2%
	Person 2		251.09 m	8.24%
Figure 65	Person 1	266.69 m	231.42 m	~8.32%

Figure	Object	Rail Scene		
		Ground Truth	Distance estimated from DisNet	Error
	Person 2		281.44 m	
	Person 3		280.87 m	
	Car 4	597.87 m	593.71 m	0.69%
Figure 66	Person	155 m	154.96 m	0.025 %
	Truck	202 m	196.34 m	2.8%
Figure 67	Person 1	162 m	158.68 m	2.04%
	Person 2	181 m	182.90 m	1.04%
	Person 3	176 m	179.99 m	2.26%

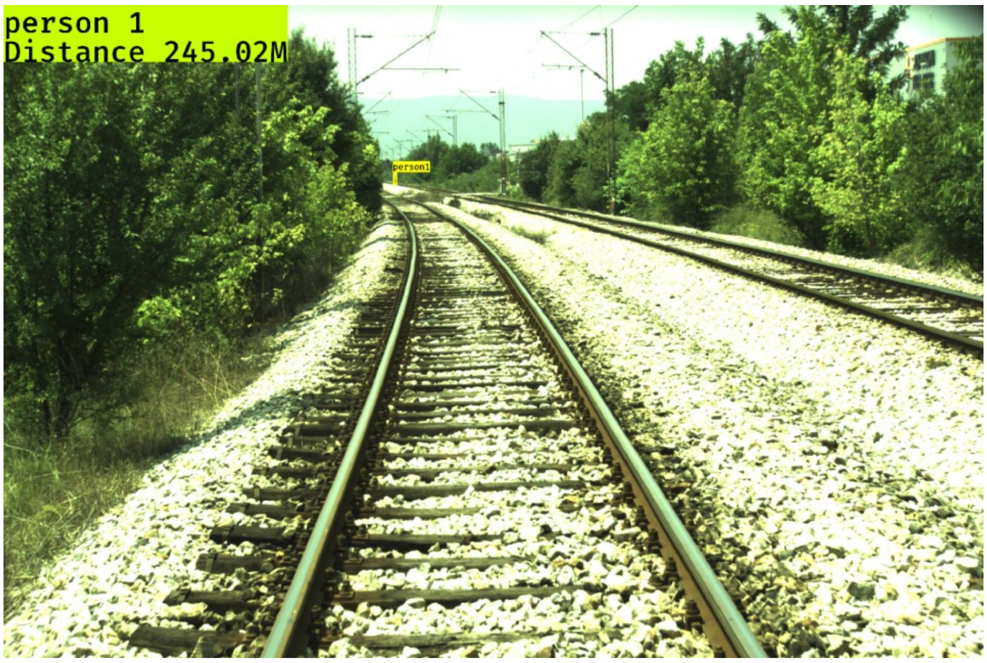

Figure 63. Mid-range object detection and distance estimation in on-board RGB camera image; Ground truth distance: 272.75 m (error 10%)

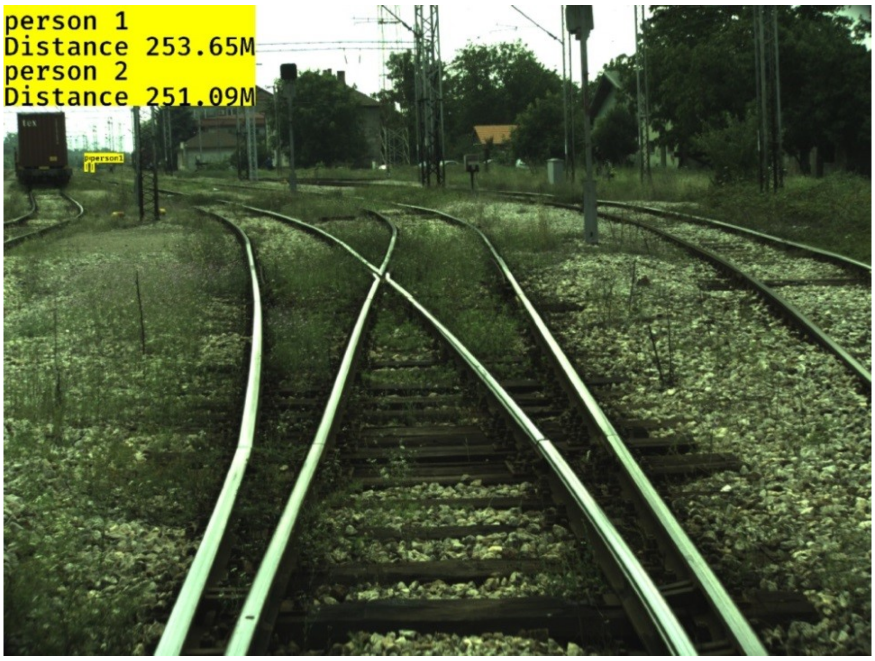

Figure 64. Mid-range object detection and distance estimation in on-board RGB camera image; Ground truth distance: 231.97 m (errors 8.2% and 8.24% respectively)

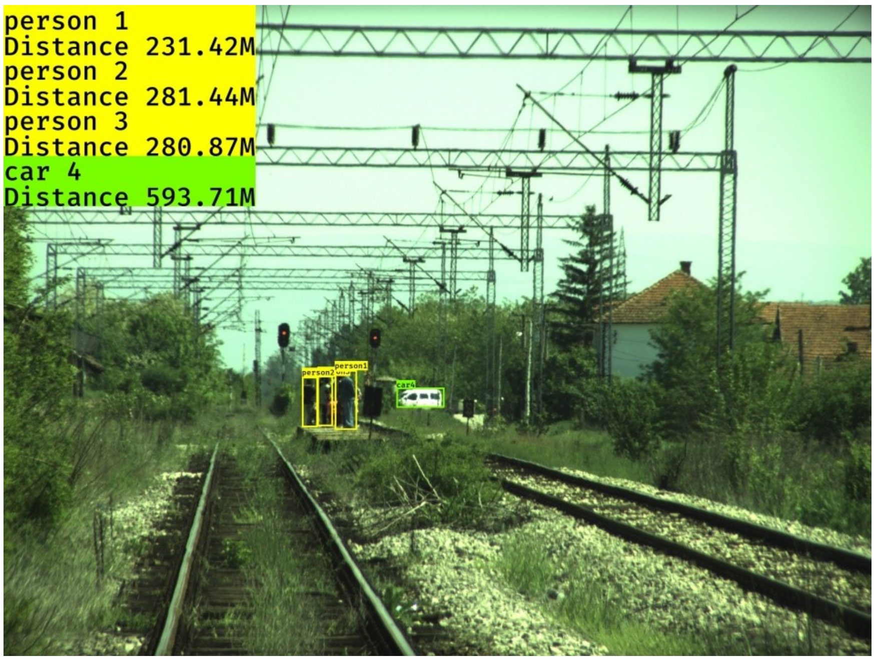

Figure 65. Mid- to Long-range object detection and distance estimation in on-board RGB camera (zoom) image; Ground truth distance: for persons (station middle point) 266.69 m (average error 8.32%), for the car 597.87 m (error 0,69%)

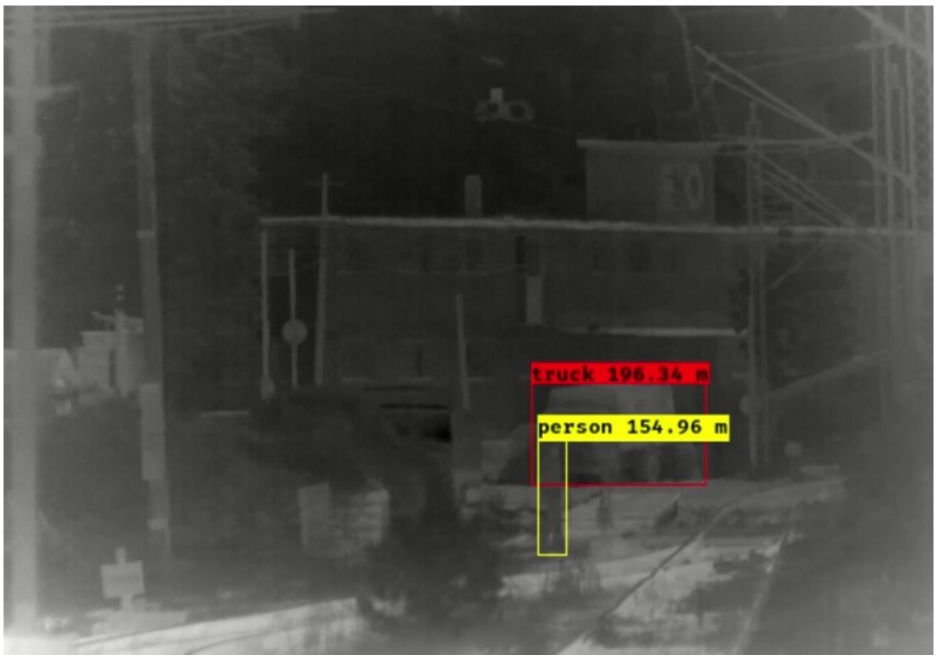

Figure 66. Object detection and distance estimation in onboard thermal camera image recorded in the environmental condition of 38°C; Good detection result in spite of low-contrast image; Ground truth distance for a person: 155 m (0.025 %)

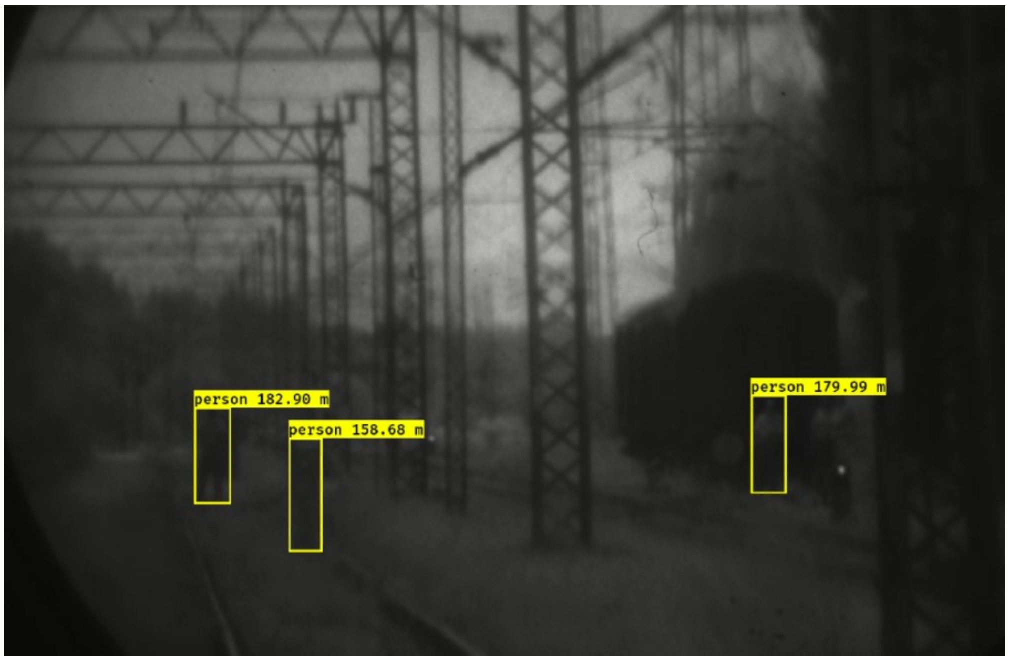

Figure 67. Mid-range object detection and distance estimation in on-board night vision camera image; Ground truth distance: 162 m, 181 m and 176 m opposed to 158.68 m, 182.90 and 179.99 m respectively.

Road Scene

Although the presented DisNet-based method for distance estimation from the monocular camera has been originally developed for autonomous obstacle detection in railway applications, it can be applied to road scenes as well. To demonstrate this, the presented method was applied to the image of a different resolution than images used for the training of DisNet. The images recorded within the project HiSpe3D-Vision presented in [135] [136] were used to evaluate the performance of the DisNet on-road scene. The main goal of HiSpe3D-Vision was to develop a high speed, low latency stereo vision-based collision warning system for automotive applications. The obstacle detection and distance calculation for collision warning was based on the segmentation of the disparity map created from the car-mounted stereo-vision system.

The result of object detection and distance estimation in a dynamic environment (moving car and moving object-obstacle) is shown in Figure 68, where the original image is overlaid with the bounding cuboid for the object closest to the car (the person on the bike). Distance for this object, as estimated by the HiSpe3D-Vision method, is given in the left upper corner of the image in Figure 68, as well as in Table 17.

In contrast to the HiSpe3D-Vision method, which detected only the object closest to the car, the presented DisNet method recognized different objects in the scene recorded by the car-mounted camera: person, bicycle, car, and track. The bounding boxes of the recognized objects are overlaid on the image in Figure 68 together with distances estimated by DisNet. The objects distance estimation achieved by DisNet vs. the distance estimation achieved by the HiSpe3D stereo vision method is given in Table 17.

Table 17. Objects Distances Estimated by DisNet vs. Objects Distances Estimated by HiSpe3D-Vision method (adapted from [124])

Object	Road Scene	
	Distance estimated by HiSpe3D-Vision [136]	Distance estimated by DisNet
Person	6.24 m	6.12 m
Bicycle	-	5.39 m
Car	-	27.64 m
Truck	-	30.25 m

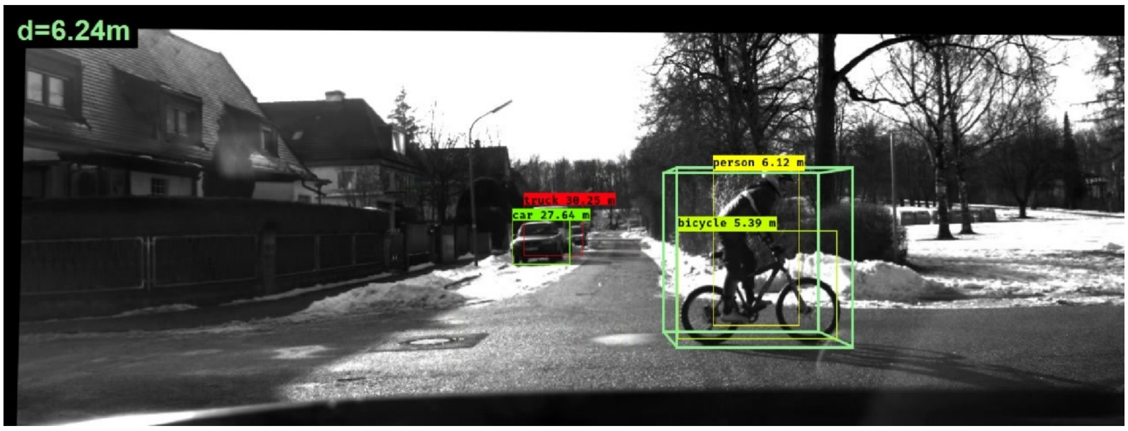

Figure 68. Road scene image overlaid with objects recognition and distance estimation results achieved by proposed DisNet and by stereo-vision based HiSpe3D method [124]

As obvious, DisNet outperforms the HiSpe3D-Vision method in a number of different objects recognized in the recorded scene. The person distance estimation by both methods is comparable.

Presented results illustrate the reliable estimation of distances from a single RGB, a thermal camera, and a night vision camera to objects in static and dynamic railway scenes recorded by cameras in various weather and illumination conditions. The general nature of the presented distance estimation method is demonstrated by the result of distance estimation in a dynamic road scene captured with a different type of cameras. This indicates that the presented method can be used for object distance estimation from different types of monocular cameras, such as thermal camera and night vision camera.

4.2 YOLO-D: a deep learning-based object-specific distance estimation from a single camera

In this section, the second method for distance estimation from a single camera has been discussed. The method is based on YOLOv3 named as YOLO-D (You Only Look Once to estimate distance). Together with object detection, the method also predicts the distance to detected object. The main idea behind this method is to replace handcrafted features calculation and DisNet as a separate network for distance estimation with a direct estimation of distance from YOLOv3 beside object detection.

In this section, firstly the modification into the existing YOLOv3 network architecture to achieve the task of object detection and distance estimation is presented. Secondly, the dataset and training method are discussed. At the end of this section, some evaluation results and the advantages and limitations of YOLO-D are also given.

4.2.1 Modification of YOLOv3 network

As explained in section 2.3.2., the "*You Only Look Once*," or YOLO is a series of models that come into different versions namely YOLOv1, YOLOv2, and YOLOv3. The end-to-end deep learning models designed for fast object detection, developed by Joseph Redmon, et al. and first term in the paper titled "You Only Look Once: Unified, Real-Time Object Detection" [70].

The YOLO is built on a single deep convolution network called DarkNet53 originally based on VGG. The proposed method is based on YOLOv3. The primary objective of YOLO as an object detection model is to predict the bounding box and classify objects. However, the proposed method based on YOLOv3 along with its primary objective of object detection also simultaneously estimates the distance to the detected objects. Hence the proposed method is named YOLO-D where D refers to distance estimation. In this section, the modification into YOLOv3 architecture and changes made in the learning process are explained.

In order to achieve this task, two major changes are made. Firstly one more output that is distance is added into the three detection layers of the YOLO architecture. For the simplification, the modification into the detection layer is shown in Figure 69. The details of YOLO architecture is given in section 2.3.2.

The purpose of three detection layers is to detect objects of big, medium, and small in size. The first, second, and third detection layers are of size 13x13x255, 26x26x255 and 52x52x255 respectively. The 13x13, 26x26 and 52x52 represent the size of the feature map whereas 255 come from the 3 x (4+1+80). '3' is the number of a bounding box that each grid cell predicted; '4' represents the coordinates of the predicted box: tx, ty, tw, th; then the '1' refers to the objectness score, which indicates how likely there is an object in that grid cell; and '80' is the number of predicted class. However, the number of classes is not fixed it depends on the classes on which YOLO is trained. In the default version, the YOLO is trained with the

COCO dataset which contains 80 classes. For example in case of two classes to predict the size of detection layers will be 21 come from the 3 x (4+1+2).

Likewise, in case of modification, the sizes of detection layers are changed due to the addition of one more output that is distance estimation. The sizes of three detection layers are changed to 13x13x24, 26x26x24 and 52x52x24 respectively. The 24 comes from 3 x (4+1+**1+2**) where additional 1 indicated the estimation of the distance to the corresponding detected object and 2 is the number of classes to predict.

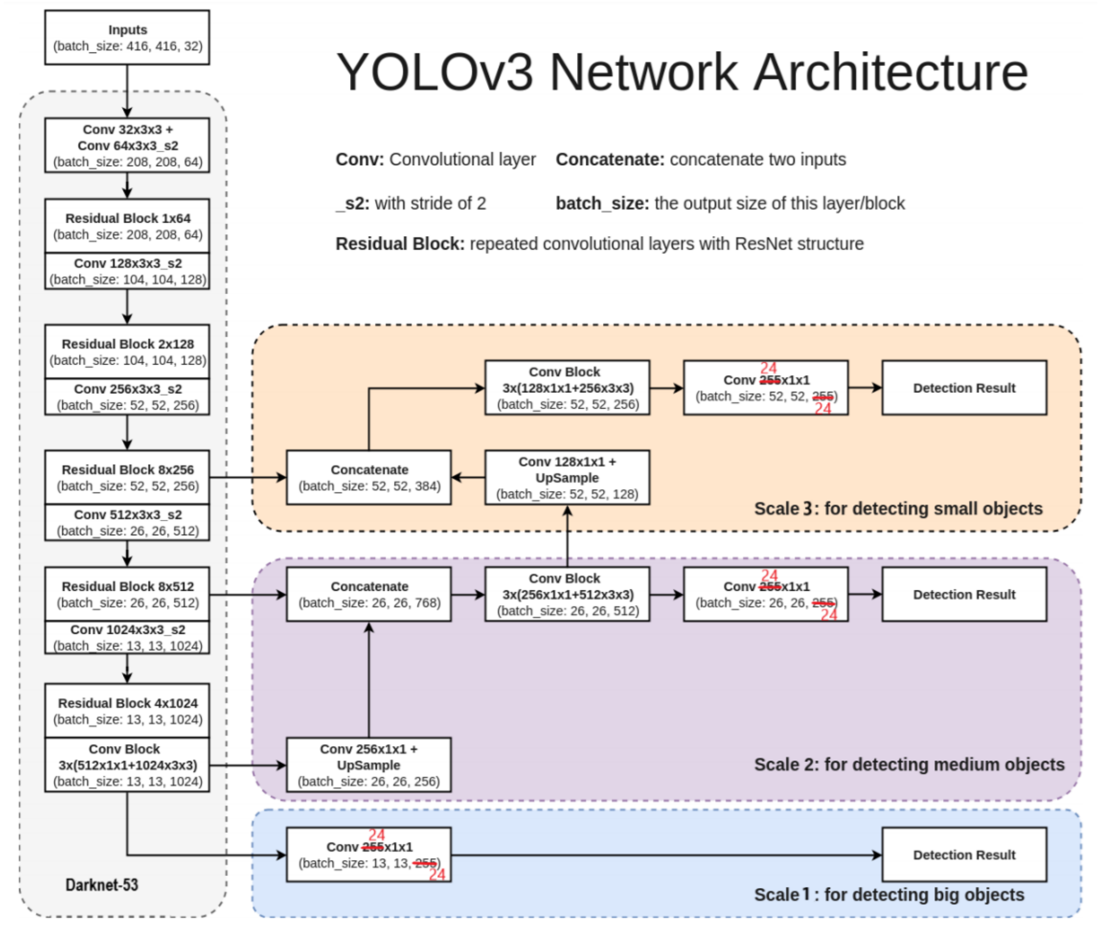
YOLOv3 Network Architecture
Conv: Convolutional layer
Concatenate: concatenate two inputs
_s2: with stride of 2
batch_size: the output size of this layer/block
Residual Block: repeated convolutional layers with ResNet structure
Inputs (batch_size: 416, 416, 32)
Conv 32x3x3 + Conv 64x3x3_s2 (batch_size: 208, 208, 64)
Residual Block 1x64 (batch_size: 208, 208, 64)
Conv 128x3x3_s2 (batch_size: 104, 104, 128)
Residual Block 2x128 (batch_size: 104, 104, 128)
Conv 256x3x3_s2 (batch_size: 52, 52, 256)
Residual Block 8x256 (batch_size: 52, 52, 256)
Conv 512x3x3_s2 (batch_size: 26, 26, 512)
Residual Block 8x512 (batch_size: 26, 26, 512)
Conv 1024x3x3_s2 (batch_size: 13, 13, 1024)
Residual Block 4x1024 (batch_size: 13, 13, 1024)
Conv Block 3x(512x1x1+1024x3x3) (batch_size: 13, 13, 1024)
Darknet-53
Conv Block 3x(128x1x1+256x3x3) (batch_size: 52, 52, 256)
Conv ~~255~~ 24 x1x1 (batch_size: 52, 52, ~~255~~ 24)
Detection Result
Concatenate (batch_size: 52, 52, 384)
Conv 128x1x1 + UpSample (batch_size: 52, 52, 128)
Scale 3: for detecting small objects
Concatenate (batch_size: 26, 26, 768)
Conv Block 3x(256x1x1+512x3x3) (batch_size: 26, 26, 512)
Conv ~~255~~ 24 x1x1 (batch_size: 26, 26, ~~255~~ 24)
Detection Result
Conv 256x1x1 + UpSample (batch_size: 26, 26, 256)
Scale 2: for detecting medium objects
Conv ~~255~~ 24 x1x1 (batch_size: 13, 13, ~~255~~ 24)
Detection Result
Scale 1 : for detecting big objects

Figure 69. The graphical representation of YOLO architecture and modification on its final detection layers [137]

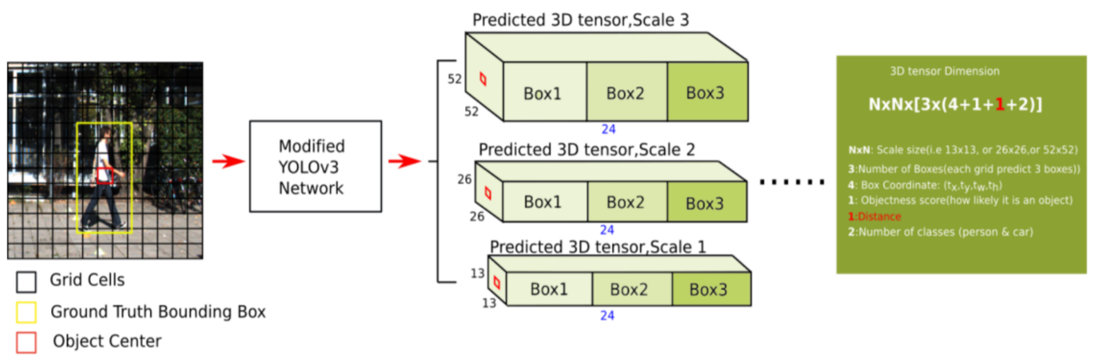
Grid Cells
Ground Truth Bounding Box
Object Center
Modified YOLOv3 Network
Predicted 3D tensor,Scale 3
52
52
Box1
Box2
Box3
24
Predicted 3D tensor,Scale 2
26
26
Box1
Box2
Box3
24
Predicted 3D tensor,Scale 1
13
13
Box1
Box2
Box3
24
3D tensor Dimension
NxNx[3x(4+1+1+2)]
NxN: Scale size(i.e 13x13, or 26x26,or 52x52)
3:Number of Boxes(each grid predict 3 boxes))
4: Box Coordinate: (tx,ty,tw,th)
1: Objectness score(how likely it is an object)
1:Distance
2:Number of classes (person & car)

Figure 70. The architecture of modified YOLOv3 (YOLO-D)

4.2.2 Loss Function

The second major change to achieve distance estimation from YOLOv3 is made into its loss function by adding the distance loss function into the YOLOv3 default loss function. The YOLO loss function is a cumulative loss function of localization (errors between the predicted bounding box and the ground truth bounding box), confidence (likelihood of objectness of the box) and class type. By adding the loss function for distance estimation the loss function for YOLO-D will be as given in equation (4-4).

$$Loss_{total} = Loss_{localization} + Loss_{confidence} + Loss_{class} + \boldsymbol{Loss_{distance}} \qquad (4\text{-}4)$$

From the understanding of loss function selection during the development of DisNet, the Mean Absolute Error function was selected over other loss function due to its small loss relative to other loss functions. Similarly, the loss function selection process was also conducted for YOLO-D training. Since the distance estimation is a regression problem, the selection of loss functions was made between the two famous MAE and MSE loss function as given in equation x and y.

$$MAE = \frac{1}{n}\sum_{i=1}^{n}\left|dist_i - \widehat{dist_i}\right| \qquad (4\text{-}5)$$

$$MSE = \frac{1}{n}\sum_{i=0}^{n}\left(dist_i - \widehat{dist_i}\right)^2 \qquad (4\text{-}6)$$

Let’s add the distance loss into the YOLO loss function. The total loss function of YOLO-D based on MAE based distance loss function is given in equation (4-7) and similarly the total loss function by adding the MSE based distance loss function is given in equation (4-8).

$$Loss_{total} = Loss_{localization} + Loss_{confidence} + Loss_{class} + \boldsymbol{Loss_{distance(MAE)}}$$

$$\begin{aligned} &= \sum_{i=0}^{s^2}\sum_{j=0}^{B} 1_{i,j}^{obj}\left[(t_x - \widehat{t_x})^2 + \left(t_y - \widehat{t_y}\right)^2 + (t_w - \widehat{t_w})^2 + (t_h - \widehat{t_h})^2\right] \\ &+ \sum_{i=0}^{s^2}\sum_{j=0}^{B} 1_{i,j}^{obj}[-\log(\sigma(t_o)) - \log(1-\sigma(t_o))] \\ &+ \sum_{i=0}^{s^2}\sum_{j=0}^{B} 1_{i,j}^{obj}\left[\sum_{k=1}^{C} BCE\left(\widehat{y_k}, \sigma(s_k)\right)\right] + \sum_{i=0}^{s^2}\sum_{j=0}^{B} 1_{i,j}^{obj}\left|dist - \widehat{dist}\right| \end{aligned} \tag{4-7}$$

$$Loss_{total} = Loss_{localization} + Loss_{confidence} + Loss_{class} + \boldsymbol{Loss_{distance(MSE)}}$$

$$\begin{aligned} &= \sum_{i=0}^{s^2}\sum_{j=0}^{B} 1_{i,j}^{obj}\left[(t_x - \widehat{t_x})^2 + \left(t_y - \widehat{t_y}\right)^2 + (t_w - \widehat{t_w})^2 + (t_h - \widehat{t_h})^2\right] \\ &+ \sum_{i=0}^{s^2}\sum_{j=0}^{B} 1_{i,j}^{obj}[-\log(\sigma(t_o)) - \log(1-\sigma(t_o))] \\ &+ \sum_{i=0}^{s^2}\sum_{j=0}^{B} 1_{i,j}^{obj}\left[\sum_{k=1}^{C} BCE\left(\widehat{y_k}, \sigma(s_k)\right)\right] \\ &+ \sum_{i=0}^{s^2}\sum_{j=0}^{B} 1_{i,j}^{obj}\left(dist - \widehat{dist}\right)^2 \end{aligned} \tag{4-8}$$

Both MAE and MSE based loss functions are evaluated for YOLO-D training and testing as given in the next sections.

4.2.3 Dataset preparation

Before beginning with the training process, firstly the dataset is required to discuss for the training of YOLO-D. There are some of the comprehensive datasets available for object detection, but none of them serves the specific purpose of this thesis which is long-range object detection with distance estimation. Table 18 shows a list of available online datasets relevant to object detection. Although the KITTI dataset [90] does have short-range distance information, it only covers urban driving scenarios.

While the primary focus of this thesis is long-range object detection and distance estimation using a single camera. Hence the proposed LRODD was also utilized.

The LRODD dataset proposed in this thesis provides all the information required for end-to-end training of YOLO-D for object detection and distance estimation, including ground truth distance to the annotated bounding box and object class. Despite the usefulness of the LRODD dataset, the dataset itself is not enough to train YOLO-D for object detection and distance estimation. The dataset provides very few data samples for object classes other than *person* object class. Furthermore, due to a few diverse examples, the dataset performance for object detection is not satisfactory. However, still, the distance ground truth labelling is beneficial for the distance estimation task of YOLO-D. In order to train YOLO-D for a new task of distance estimation without losing its performance on object detection, two widely used object detection datasets i.e. COCO, KITTI were also used in the training process together with LRODD dataset. COCO teaches the network object detection while KITTI and LRODD dataset teaches distance estimation and improve object detection for road and railway scenes.

Table 18. List of available datasets related to object detection and distance estimation

Dataset	Annotated Images	Distance Range
COCO	~ 120,000	No distance information
Pascal VOC	~ 12000	No distance information
KITTI	~ 7500	0 to ~120 meters
LRODD	~ 8000	20 to ~ 925 meters

KITTI Dataset

In order to combine KITTI and LRODD dataset to train YOLO-D, the KITTI labelled dataset was organized in the form of a table in same order as LRODD dataset in a text file. Each row of the text file corresponds to one particular image as well as the bounding box, class and distance information of the objects in that image. The parameters in each row are arranged as follow:

img_path	dist	bbox_left	bbox_top	bbox_right	bbox_bottom	class_id	………

Where, *'img_path'* is the location of the training image; *'bbox_left'* and *'bbox_top'* are the left top coordinates of the bounding box of the object in the image, while

’bbox_right’ and *‘bbox_top’* are the right bottom coordinates; *‘class_id’* refers to ‘Person’ and ‘Car’ object class; ‘dist’ represents the distance to the object. More than one object in an image is also represented in the same row.

There were 7481 annotated images from KITTI combined with 192 images from the LRODD dataset containing multiple objects. In total 7673 annotated images were used for the training and testing of YOLO-D. The KITTI and LRODD datasets were randomly split into 80% of training, 14% of validation, and 6% of the test dataset, as shown in Table 19.

Table 19. Information about training, validation and test sets for the KITTI and LRODD datasets

Dataset	Annotated images	Training dataset	Validation dataset	Test dataset
KITTI	7481	5985	1047	449
LRODD	192	153	27	12
KITTI + LRODD	7673	6193	1074	461

4.2.4 Training and testing

Instead of training the modified YOLO (YOLO-D) from scratch, the weights of the network trained from the COCO dataset were loaded. The main concept of transfer learning was applied here while training YOLO for distance estimation. The pre-trained YOLO model with COCO images learned the object detection task. It is assumed that the pre-trained YOLO network with COCO dataset has been trained quite well for object detection, by training the whole YOLO-D network, the weights of the network can modify too soon (lower layers) and too much which can disturb the performance of the model on object detection task. The YOLO-D model was trained to fine-tune the weights learned from the COCO dataset to work on the targeted dataset and also to predict distance.

Considering the size of our training dataset and the computation capability of the processing computer in the lab, a mini-batch gradient descent method was utilized, i.e. the total training images are divided into the batch size of 8 and for epoch, 8 images are fed into the network to train.

The training of our YOLO-D network comprises two training stages. In the first training stage, the first 53 convolutional layers (main body of YOLOv3 network which is Darknet-53) were frozen, only the last remaining convolutional layers were trained. In order to get a stable loss for the first stage, the network was trained by all the training images for 50 epochs. In the second training stage, the first 53 layers are unfrozen and all the layers are trained for another 50 epochs. During the first training stage, the network adapts its weights of last layers, whereas in the second stage whole network fine-tune its weights based on weights learned from the first stage. In order to avoid over-fitting, the early-stopping method and learning rate reducing method were applied. To be specific, during training, when the loss on the validation dataset after 3 subsequent epochs stops reducing, the learning rate will become 10 times smaller, and if the loss doesn't change for 10 epochs, the training will be stopped. The two stages of the training process of YOLO-D on two versions of loss function are shown in Figure 71 and Figure 72.

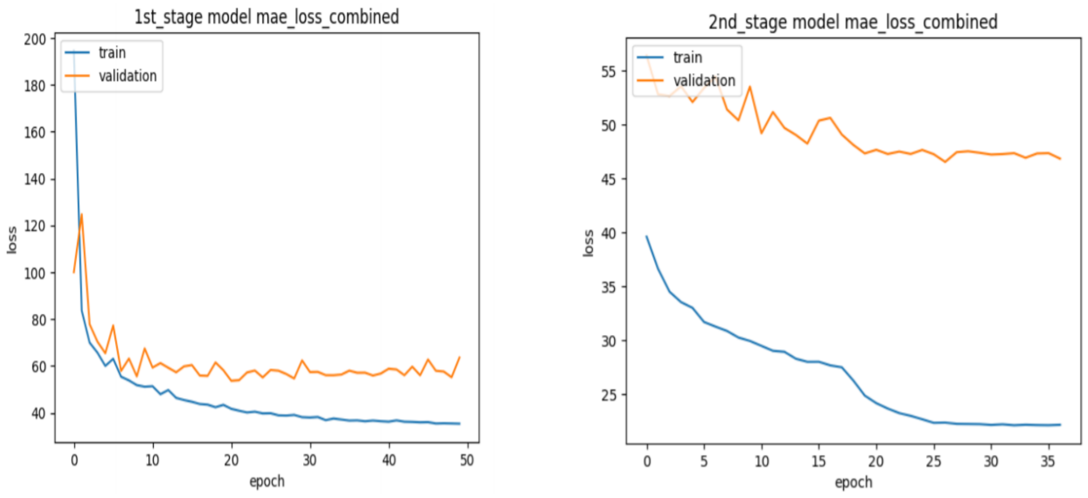

Figure 71. 1st and 2nd training stage of the based on MAE-distance loss function

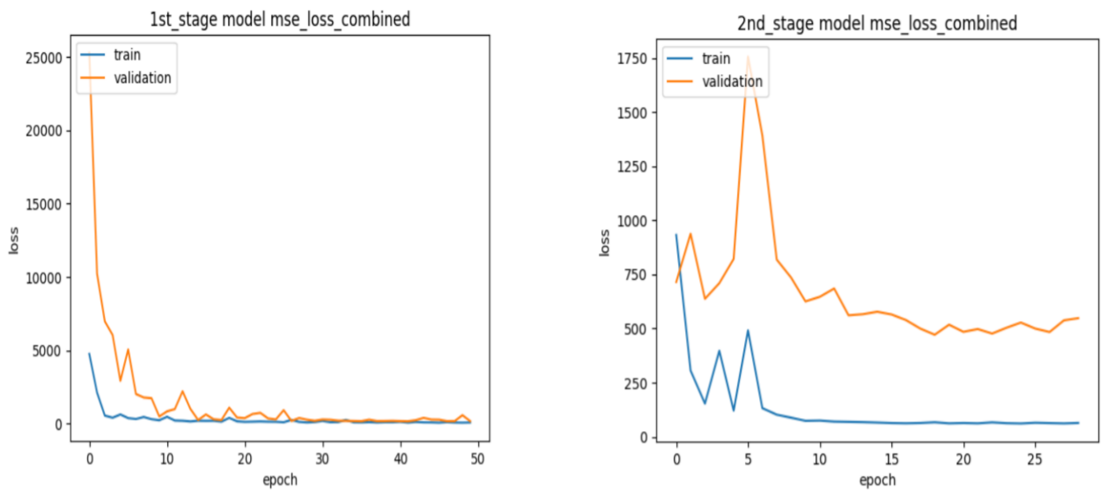

Figure 72. 1st and 2nd training stage of the based on MAE-distance loss function

From the figures listed above, it is clear that, for the network based on MAE-distance loss function, the training loss drops constantly and the training stops at 37 epochs at the second stage; while for the network of MSE-distance loss function, the loss is relatively significant and unstable and the training stops at 28 epochs at the second stage.

4.2.5 Performance Evaluation

In this section, the performance on object detection and distance estimation is measured separately for the YOLO-D model based on MAE and MSE loss functions. The performance of object detection is measured based on the confusion matrix and metrics of precision and recall as well as the average precision (AP) [138] of two object classes ‘Person’ and ‘Car’. The test dataset images were used for performance evaluation. The test dataset of 461 images contains 2159 cars and 326 persons which were labelled, as shown in Figure 75.

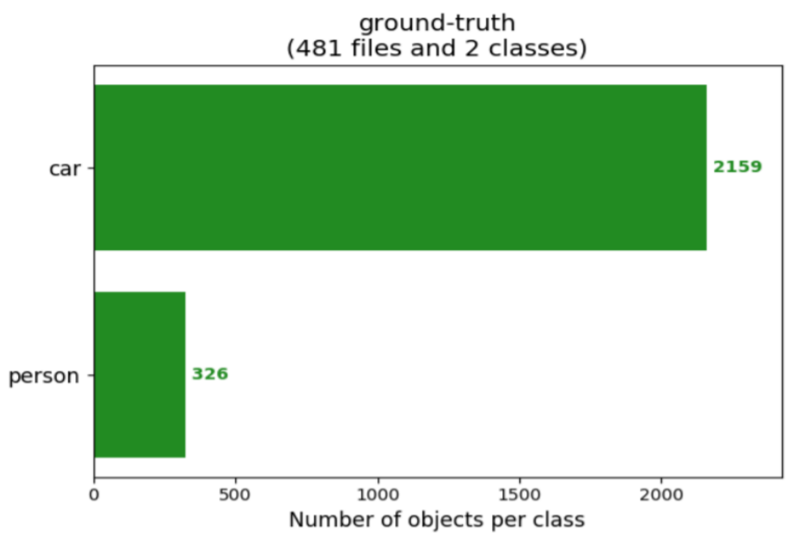

Figure 73. Number of ground-truth labelled cars and persons in the test dataset

The YOLO-D model trained with MAE loss function detects 1729 cars out of 2159 and 209 persons out of 326. On the other side MSE based YOLO-D model, detects only 1402 cars and 140 persons correctly, as shown in Figure 74. Here, when the detected object shares the same label with the ground truth object and the IoU (Intersection over Union) is greater than 0.5, the detection would be considered as true positive. False-positive refers to the detection whose IoU with ground truth object is less than 0.5 or no ground truth object matches that detection.

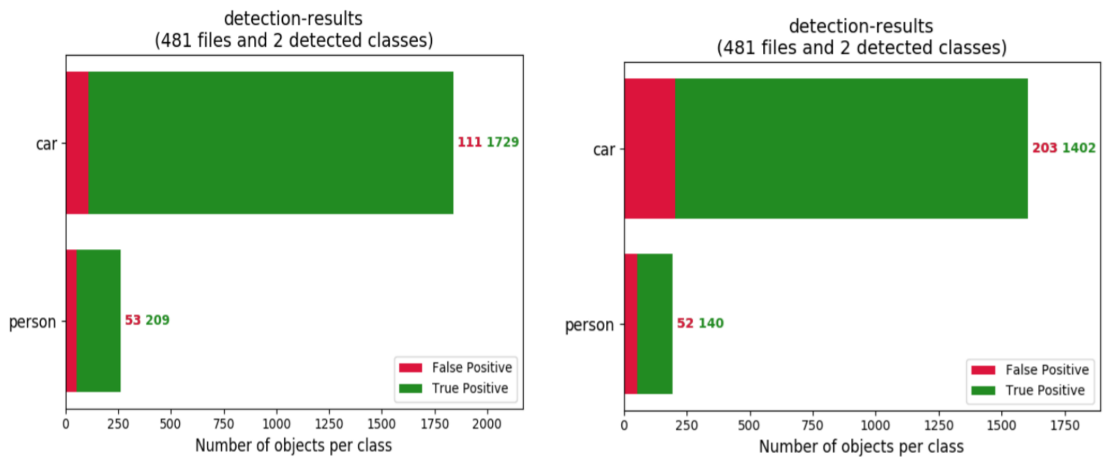

Figure 74. Detection results of network based on MAE-distance loss

An example of true positive and false positive during the evaluation process can be reviewed in Figure 75. In which the light blue bounding boxes are the ground truth bounding box provided by the KITTI dataset, green boxes are true positive predicted bounding boxes, and red box is the false positive prediction that falsely predicts that symbol as a person.

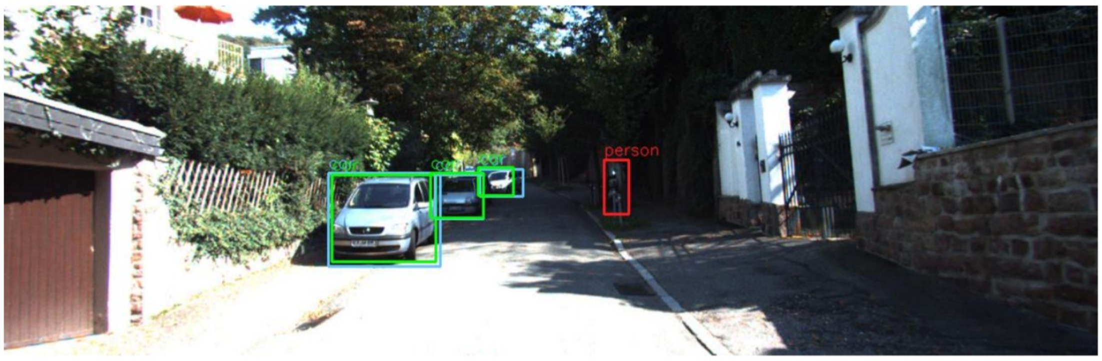

Figure 75. An example of true positive and false positive during the evaluation process

By referring to the method [138] and setting a different threshold for the confidence score that we predicted, we got different pairs of precision and recall value and then plotted the Precision-Recall (PR) curve of these two classes, as shown in Figure 76 and Figure 77.

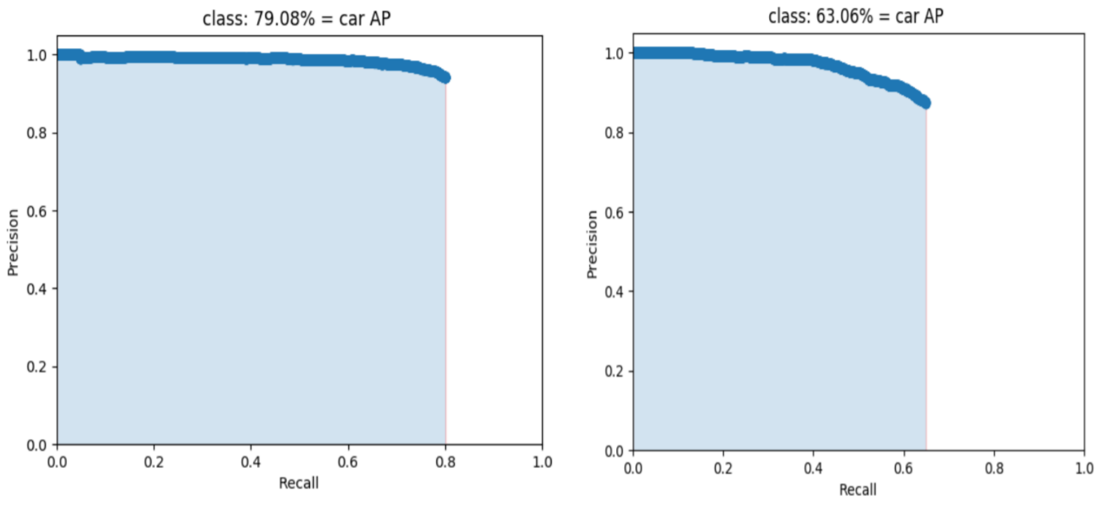

Figure 76. PR curve of car prediction by network-based on MAE and MSE-distance loss

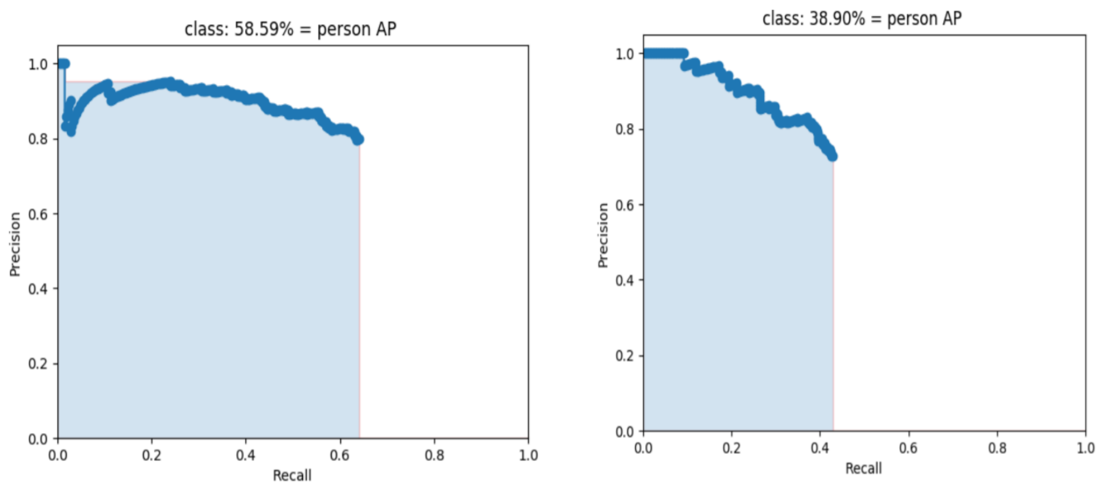

Figure 77. PR curve of person prediction by network-based on MAE and MSE distance loss

Then through calculating the area under the Precision-Recall curves, the average precision (AP) for these two classes (car and person) as well as the mean average precision (mAP) for these two types of network is measured, as shown in Figure 78.

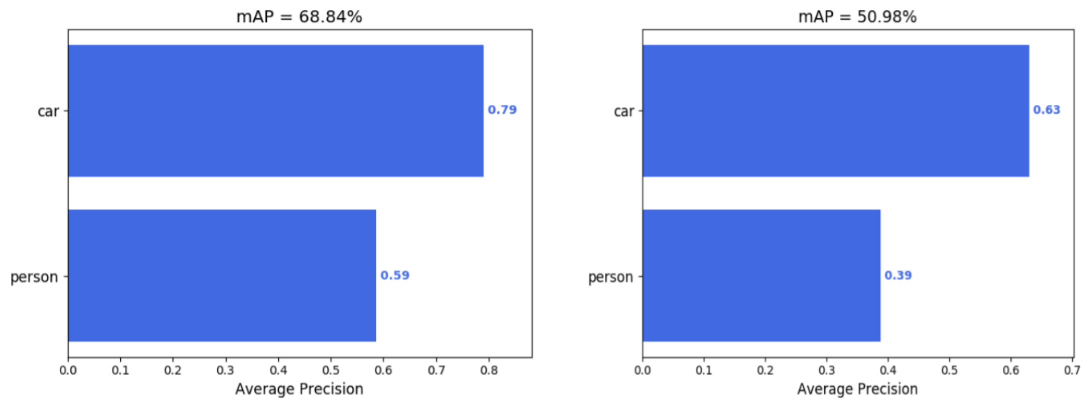

Figure 78. Average Precision of prediction by network-based on MAE and MSE distance loss

From Figure 78, it is clear that for the network trained by MAE- distance loss, the average precision of car and person achieves 79% and 59% separately and the mean average precision is 68.84% for two object classes i.e. Person and Car; while for the other type, the average precision of car and person is relatively lower, 63% and 39% respectively, and the mAP is 50.98%.

Additionally, the detection performance was evaluated on LRODD images from the test and validation dataset. For the network trained by MAE-distance loss, 67 out of the 86 persons could be detected correctly (IoU>=0.5), while for the other, only 39 persons could be detected correctly. An example of these two detections at the ground truth distance of 320m is shown in Figure 79 and Figure 80, respectively.

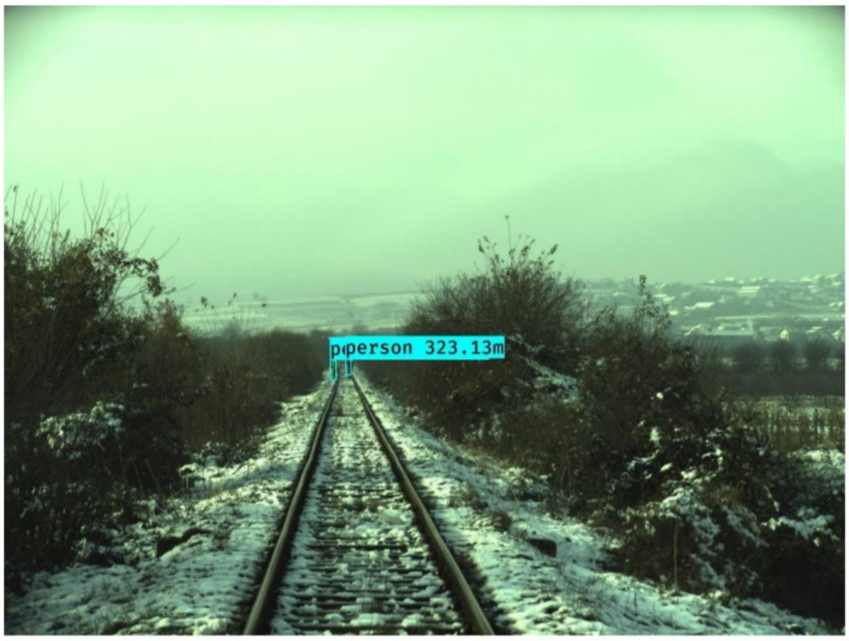

Figure 79. Detected objects at 320m by network-based on MAE-distance loss

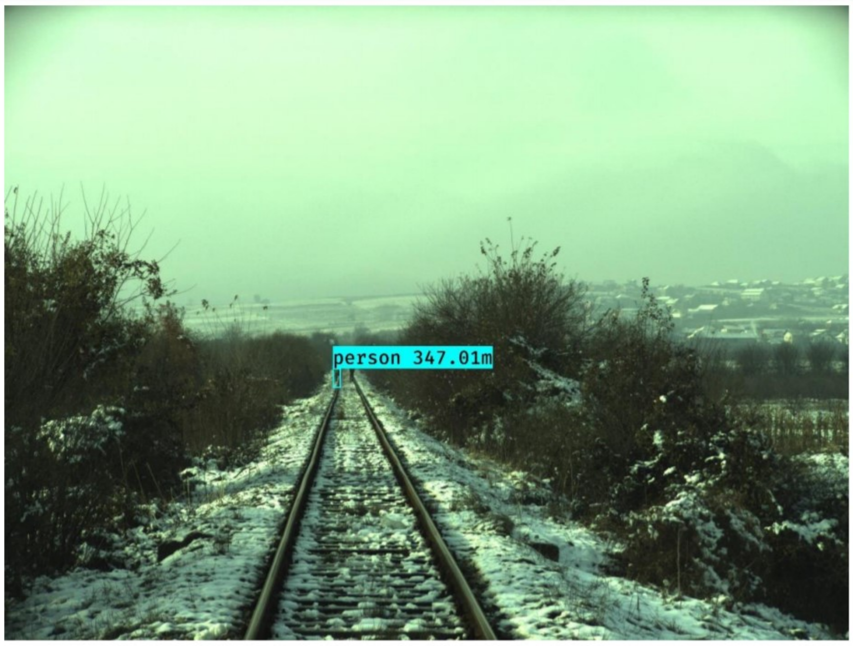

Figure 80. Detected objects at 320m by network-based on MSE-distance loss

From the figures and statistics listed above, the conclusion could be obtained that, the object detection performance of the YOLO-D model trained by MAE-distance loss is better than that trained by MSE-distance loss.

Similarly, the performance of YOLO-D to estimate distance is measured for both detection classes. KITTI test dataset and SMART test dataset were separately evaluated. Firstly, in the KITTI test dataset, for the network based on MAE-distance loss, the average error is 1.12 meters and on the other side, the average error for the MSE-based model is 1.25 meters as shown in Table 20. Average error and accuracy of YOLO-D for both object classes on KITTI test dataset. The accuracy of the network for distance estimation based on MAE-distance loss is 97.5% while for the MSE-based is 96.9%. The accuracy of the model is measured with the tolerance criteria of 5 meters which means that the distance estimation with an error less than or equal to 5 meters is considered as an accurate measurement.

Table 20. Average error and accuracy of YOLO-D for both object classes on KITTI test dataset

Modified Network	Average Error	Accuracy (<=5m)
Modified YOLOv3 Network based on MAE-distance loss	1.12m	97.5%
Modified YOLOv3 Network based on MSE-distance loss	1.25m	96.9%

Similarly, in the LRODD test dataset, the average error between predicted distance value and ground truth distance value for the network based on MAE-distance loss is 10.83 meters, while for the other is 46.03 meters. Since the distance range in the LRODD dataset is quite large (from 20 meters to 925 meters) and the evaluation dataset size is quite small, therefore the accuracy of predicted distance is not calculated as a distance evaluation metric. Instead, the scatter plot of distance between the ground truth and predicted value on these two types of model are plotted, as shown in Figure 81.

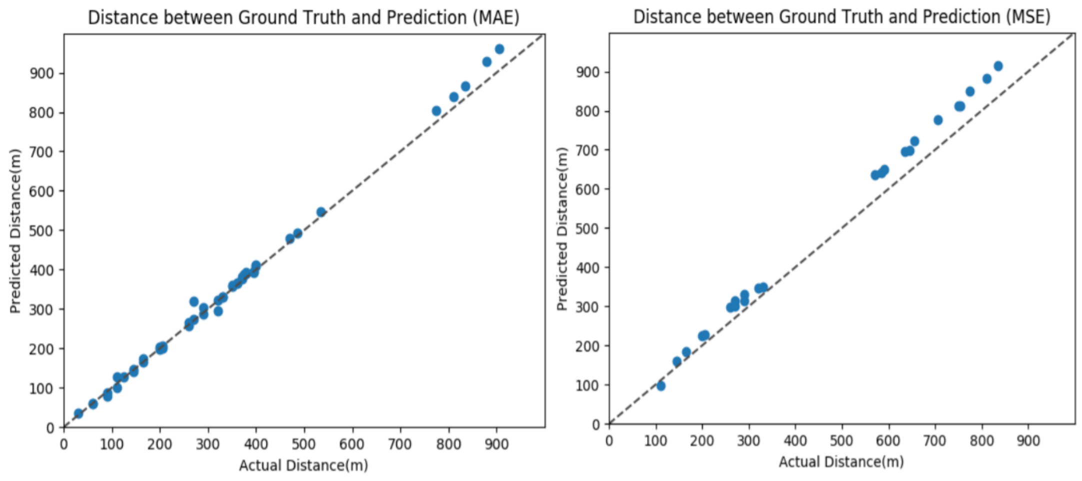

Figure 81. Scatter plot of distance on the network based on MAE and MSE distance loss

In Figure 81, the left plot shows that the estimated values are closer to ground truth distance compared to the right plot. It shows that, for long-range distance estimation, the performance of network-based on MAE distance loss is better than the network based on MSE distance loss function.

In conclusion, when it comes to the performance of object detection, the network trained by MAE-distance loss performs much better than the model trained by MSE-distance loss. With regard to the performance of distance estimation on the KITTI dataset, there is no noticeable difference between these two networks, while for the long-range distance in the LRODD dataset, the performance of network-based on MAE-distance loss is better than the MSE-based model.

4.2.5.1 Road Scene

Some results of test images as well as the ground truth information is shown in the following figures 81-83 and tables 21-23:

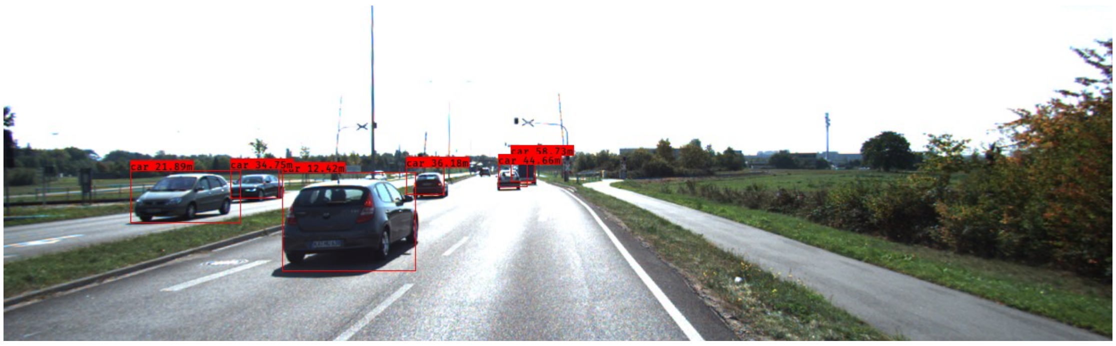

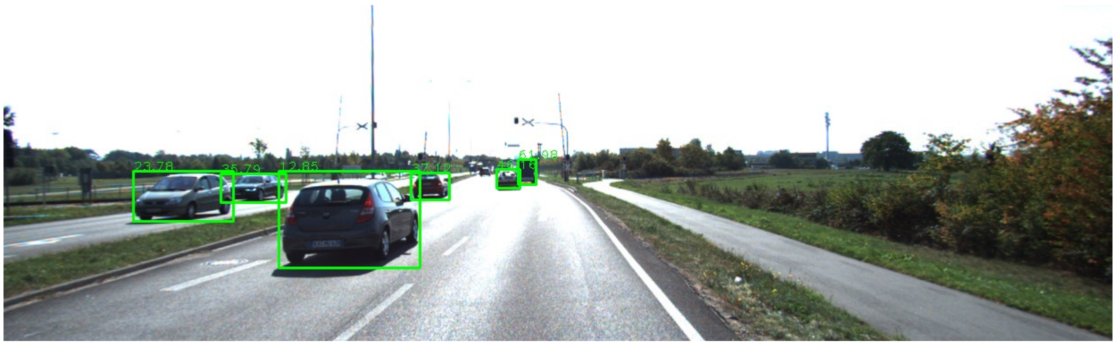

Figure 82. YOLO-D detection result of test image 1 from KITTI dataset

Table 21. Ground truth and estimated distance test image 1 from KITTI dataset

	Car1	Car2	Car3	Car4	Car5	Car6
Estimated	12.42m	21.89m	34.75m	36.18m	44.66m	58.73m
Ground Truth	12.85m	23.78m	35.79m	37.12m	46.16m	61.98m

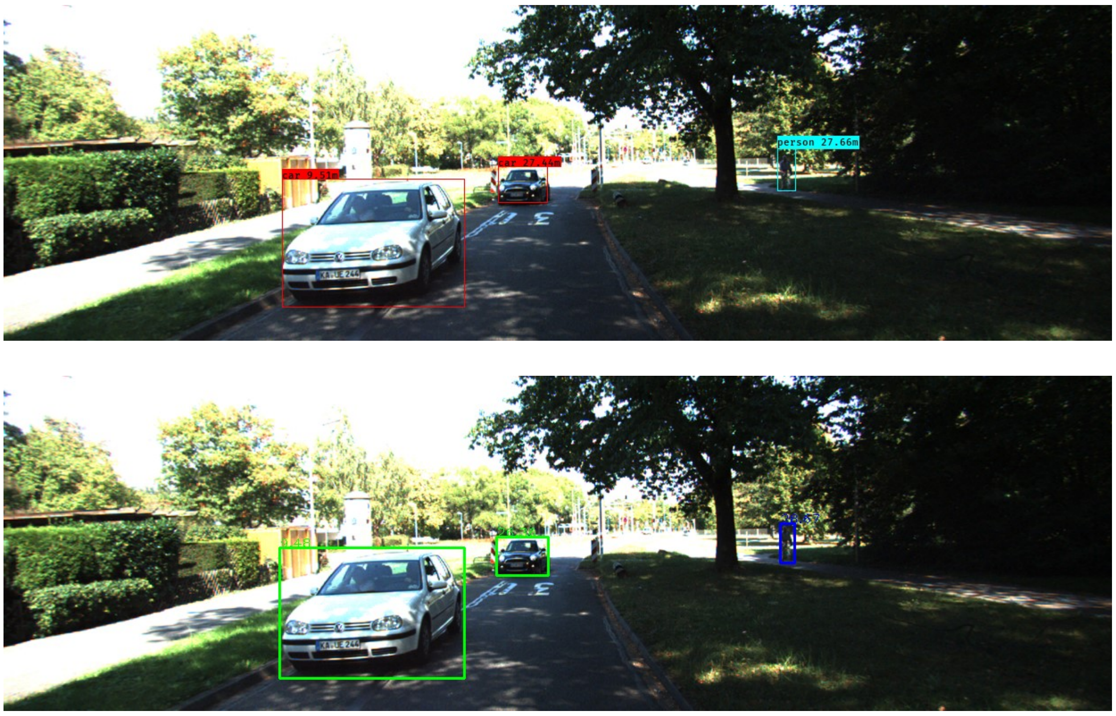

Figure 83. YOLO-D detection result of test image 2 from KITTI dataset

Table 22. Ground truth and estimated distance test image 2 from KITTI dataset

	Car1	Car2	Car3
Estimated	9.51m	27.44m	27.66m
Ground Truth	9.48m	26.36m	28.67m

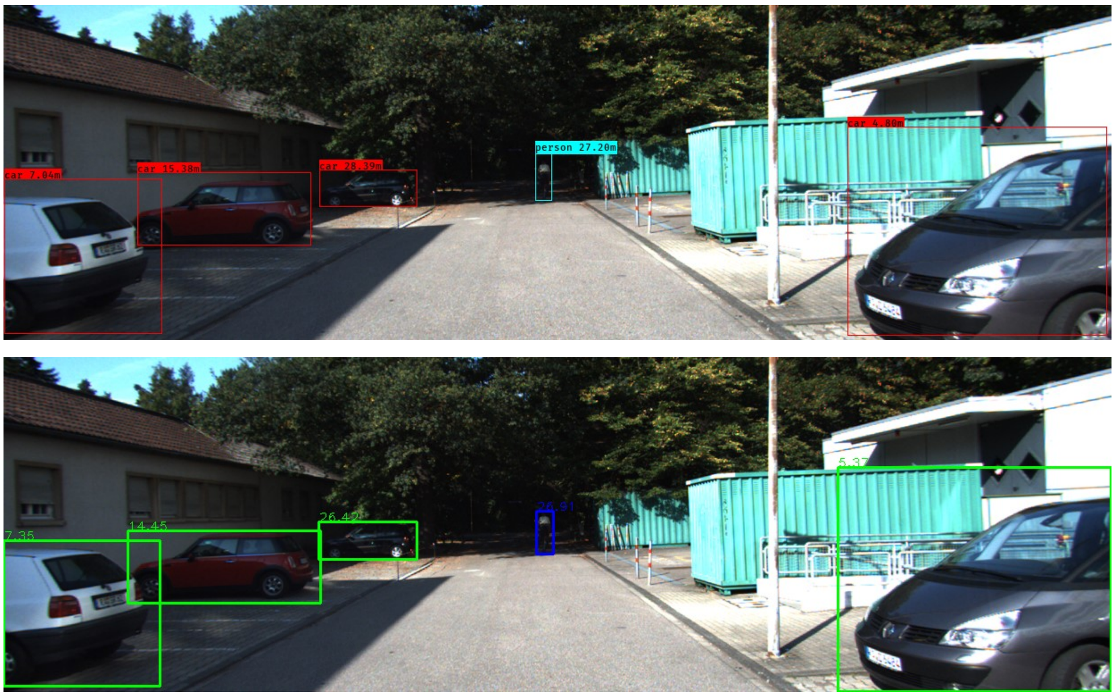

Figure 84. YOLO-D detection result of test image 3 from KITTI dataset

Table 23. Ground truth and estimated distance test image 3 from KITTI dataset

	Car1	Car2	Car3	Car4	Person1
Estimated	4.80m	7.04m	15.38m	28.39m	27.20m
Ground Truth	5.37m	7.35m	14.45m	26.42m	26.91m

In addition, the performance of YOLO-D model is compared with DisNet and HiSpe3D-Vision method [51] by applying these methods into an image that is totally different from our training dataset (i.e., the resolution and color of the image). The detection result of HiSpe3D-Vision is shown in the left upper corner of the image in Figure 85, which could only detect the distance to the person. The detection from YOLO-D is also shown in the form of bounding boxes and overlaid distance above the detected objects. The results of DisNet are taken from the Table 17 as shown in section 4.1.3. The comparison of distance estimation results among these methods are given in Table 24.

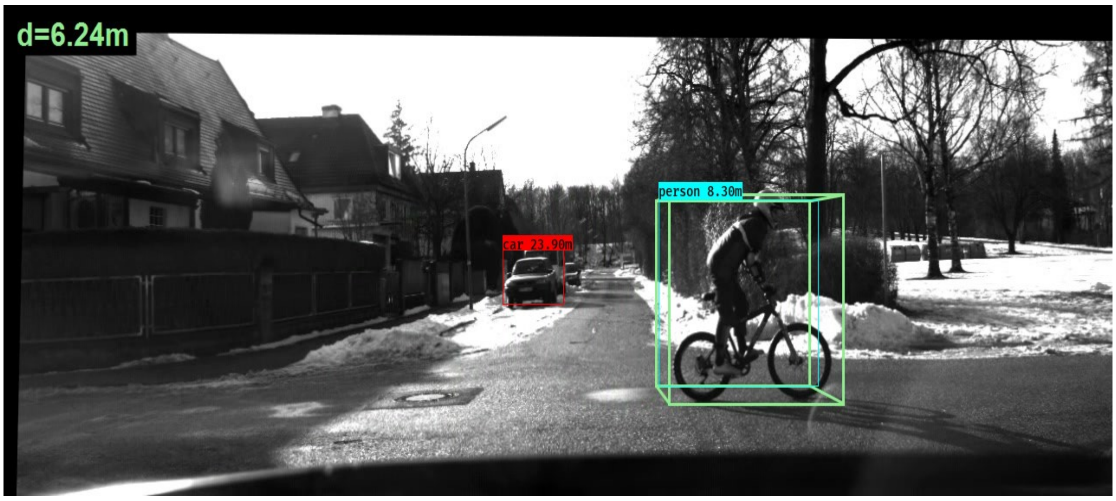

Figure 85. Objects distance estimated by YOLO-D vs DisNet vs HiSpe3D-Vision method

Table 24. Comparison of distance estimation among three methods

Object	Distance Estimation		
	HiSpe3D-Vision	DisNet	YOLO-D
Person	6.24 m	6.12 m	8.30 m
Bicycle	-	5.39 m	-
Car	-	27.64 m	23.90 m
Truck	-	30.25 m	-

The distance estimated by YOLO-D method is close to the estimation from DisNet. Although YOLO-D could not detect the Truck and Bicycle currently, as the training dataset does not contain these classes and model was not trained to detect them.

4.2.5.2 Railway Scene

Some of the results of the YOLO-D based distance calculation with RGB cameras for railway scenarios are shown in Figure 85-87. However, the result of YOLO-D distance estimation for thermal and night vision images are not shown here but the method is also capable to work for them.

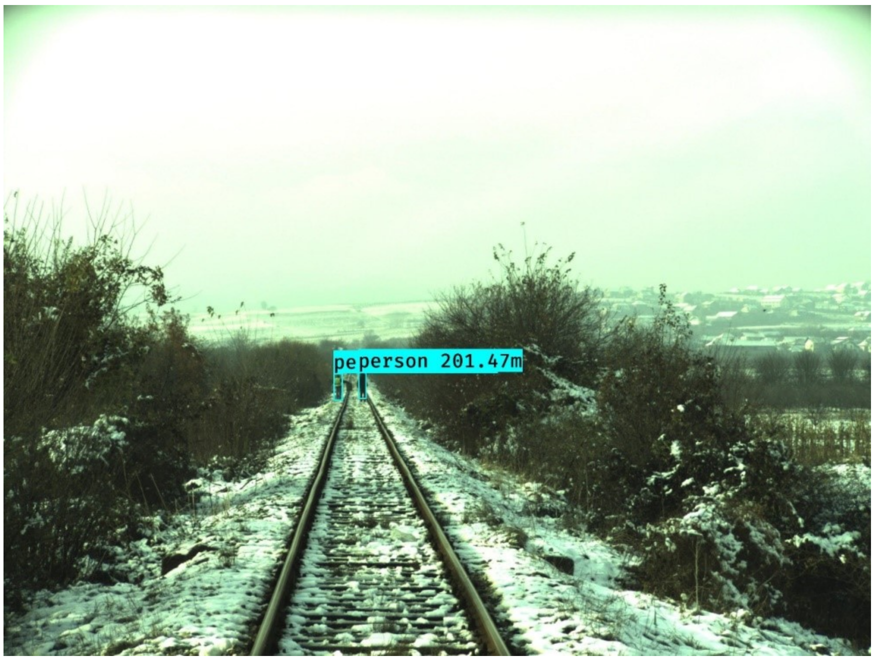

Figure 86. YOLO-D detection result of test image 1 from LRODD dataset

Table 25. Ground truth and estimated distance test image 1 from LRODD dataset

	Person1	Person2
Estimated	206.59m	201.47m
Ground Truth	205m	205m

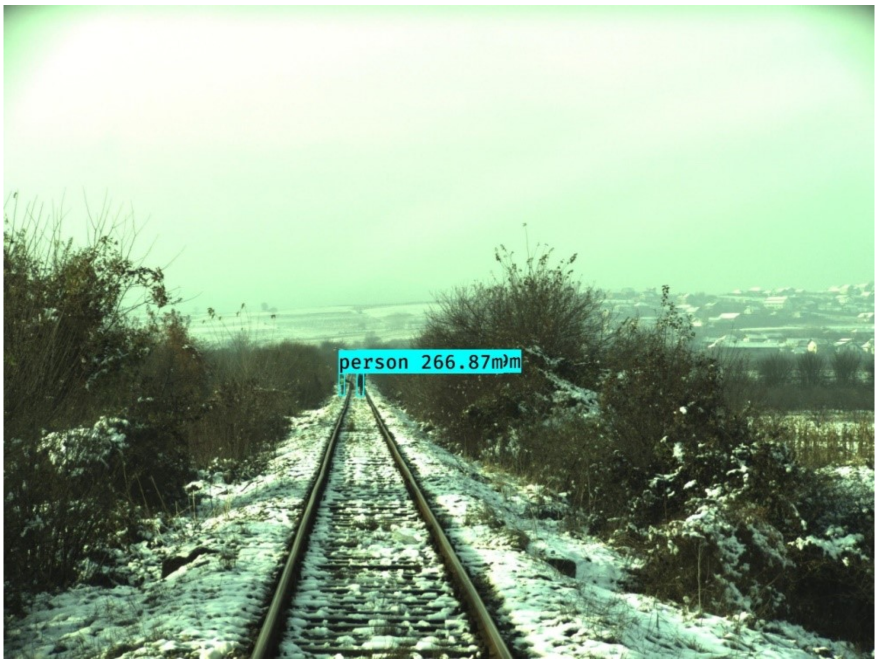

Figure 87. YOLO-D detection result of test image 2 from LRODD dataset

Table 26. Ground truth and estimated distance test image 2 from LRODD dataset

	Person1	Person2
Estimated	266.87m	257.79m
Ground Truth	260m	260m

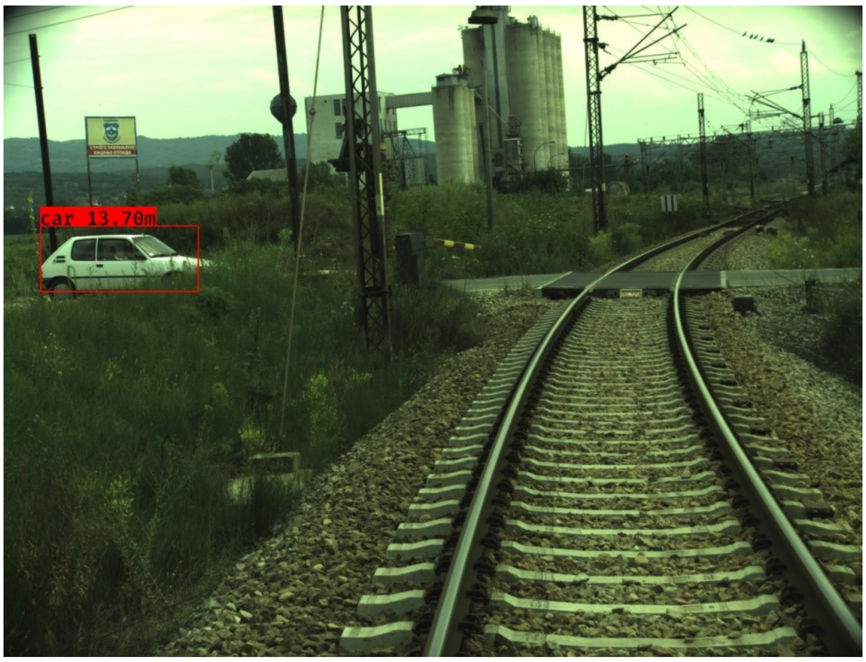

Figure 88: YOLO-D detection result of test image 3 from LRODD dataset

Table 27: Ground truth and estimated distance test image 3 from LRODD dataset

	Car
Estimated Distance	13.7 m
Ground Truth Distance	14.5 m

4.2.6 Discussion

In this chapter, two methods to estimate the distance to the detected objects were presented. The first method is named DisNet, which is a classical artificial neural network-based method that takes as an input hand-crafted features of the detected object to estimate the distance to the detected object. In contrast to DisNet, the second method named as YOLO-D is a deep learning method that does not require manual extraction of features for distance estimation to the detected objects. It works on the principle of end-to-end learning, it estimates distance and detects objects in a given input image. It finds itself the relation to change of distance to the object of a specific class in an image by investigating the visual features.

In this chapter, the methodology, concept, and evaluation results of DisNet and YOLO-D were explained. Both the methods show promising results for distance estimation; however, some limitations and future ideas to improve their performance are important to highlight.

One of the main limitations of both methods is to deal with object occlusion, unreliable distance estimation in case of false and imprecise object bounding box prediction from the object detection model. Furthermore, the methods were evaluated on a limited size dataset, the performance can be improved more with the increase in dataset specifically for YOLO-D which as deep learning-based object detection and distance estimation network required more data to train in comparison to DisNet. The dataset designed explicitly for object detection and distance estimation such as the LRODD dataset can fulfill the requirement for the training of YOLO-D. Additionally, more object classes can be added to the dataset.

In the next section and chapters, the problems encounter is addressed and some new ideas are presented to overcome such problems.

5. A machine learning based distance estimation from multiple cameras

In this chapter, a novel method for distance estimation from multiple cameras to the object viewed with these cameras is presented named Multi-DisNet. Multi-DisNet is a multilayer neural network, which is used to learn the relationship between the sizes of the bounding boxes of the objects in the camera's images and the distance between the object and cameras.

The supervised learning technique was used to train the Multi-DisNet network where the input features were manually calculated parameters of the objects bounding boxes in the camera's images and desired outputs were ground-truth distances between the objects and the cameras. The performance of multi-DisNet was evaluated on images of real-world railway scenes. As a proof-of-concept, the results on the fusion of two sensors, an RGB and thermal camera mounted on a moving train, in the Multi-DisNet distance estimation system are shown. Presented results demonstrate both the good performance of the Multi-DisNet system to estimate the mid (up to 200 m) and long-range (up to 1000 m) object distance and benefit of sensor fusion to overcome the problem of not reliable object detection. The Multi-DisNet was presented by Haseeb et al. in [120].

5.1 Multi-DisNet: a machine learning-based robust distance estimation from multiple cameras

The architecture of the Multi-DisNet-based distance estimation system, with the setup assuming two cameras mounted horizontally parallel, an RGB camera and a thermal camera, is illustrated in Figure 89.

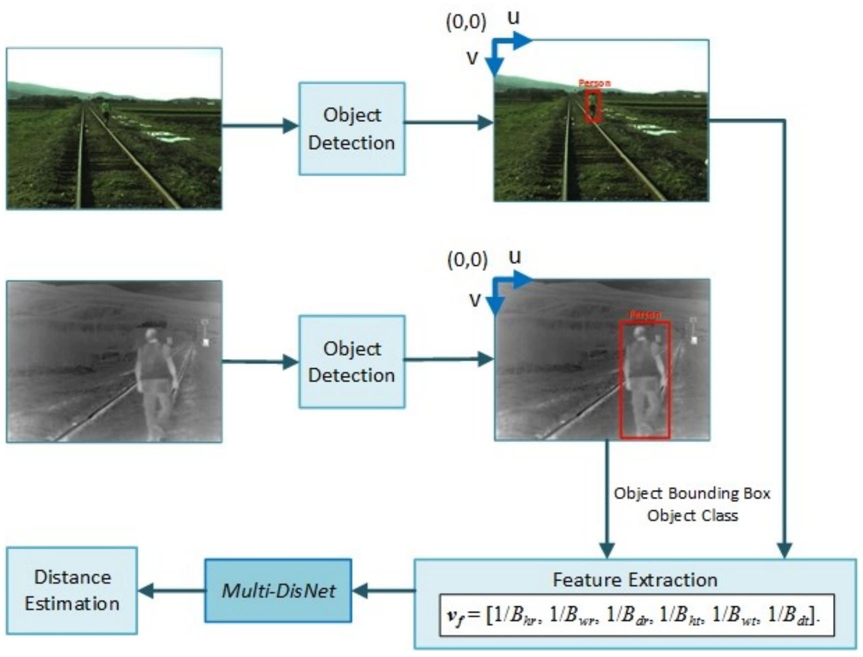

Figure 89. The Multi-DisNet-based system for object distance estimation from a multi-camera system.

Each of two synchronized images of the same scene, captured by RGB and thermal camera sensors, are inputs to an Object Detector module. Different object detectors can be integrated into the system. Independently of the Object Detector type, its outputs must be bounding boxes of detected objects in the image. The resulted corresponding objects bounding boxes are then processed to calculate the features, bounding boxes parameters based on which the trained Multi-DisNet gives as outputs the estimated distance of the object to the multi-camera sensors. In the system architecture illustrated in Figure 89, an example of the estimation of the distance of a person on the rail tracks is shown.

5.1.1 Feature Extraction

In total, 755 bounding boxes of objects were manually extracted from recorded synchronised RGB and thermal camera images using the VGG Image Annotator tool [139]. For each object bounding box extracted from RGB images and for each object bounding box extracted from thermal images, a three-dimensional feature vector v was calculated:

$$\boldsymbol{v} = [1/B_{hi}, 1/B_{wi}, 1/B_{di}], i = r, t \tag{5-1}$$

where indexes r and t indicate features extracted from RGB and thermal images respectively, and the coordinates of vector $\boldsymbol{v}$ are the following features:

Height, B_{hi}=(height of the object bounding box in pixels/image height in pixels)

Width, B_{wi}=(width of the object bounding box in pixels/image width in pixels)

Diagonal, B_{di}=(diagonal of the object bounding box in pixels/image diagonal in pixels)

The ratios of bounding box sizes and image size were used as the features so to enable the use of the generated dataset for any image resolution. The inverse of features, B_{hi}, B_{wi} and B_{di} were finally selected as the best features due to their high correlation with the desired output (distance to the object). Combining the features extracted from both sensor modules, a joint vector, that is a vector of fused data $\boldsymbol{v_f}$ of dimensions 6x1 is obtained.

$$\boldsymbol{v_f} = [1/B_{hr}, 1/B_{wr}, 1/B_{dr}, 1/B_{ht}, 1/B_{wt}, 1/B_{dt}] \tag{5-2}$$

5.1.2 Multi-DisNet Architecture

In order to find the appropriate number of hidden layers and neurons per layer, the best configuration of hidden layers and neurons obtained from the GridSearch estimator [140] was used for Multi-DisNet architecture. As shown in Figure 90, the Multi-DisNet network consists of 6 neurons in the input layer which represents the features extracted from bounding boxes, followed by the 3 hidden layers with 150 neurons in each layer and one neuron in the output layer which represents the distance estimation. For this analysis and proof-of-concept, a reduced dataset was used. Whereas the dataset was split into 3 sets for training 80%, validation 10%, and testing 10%.

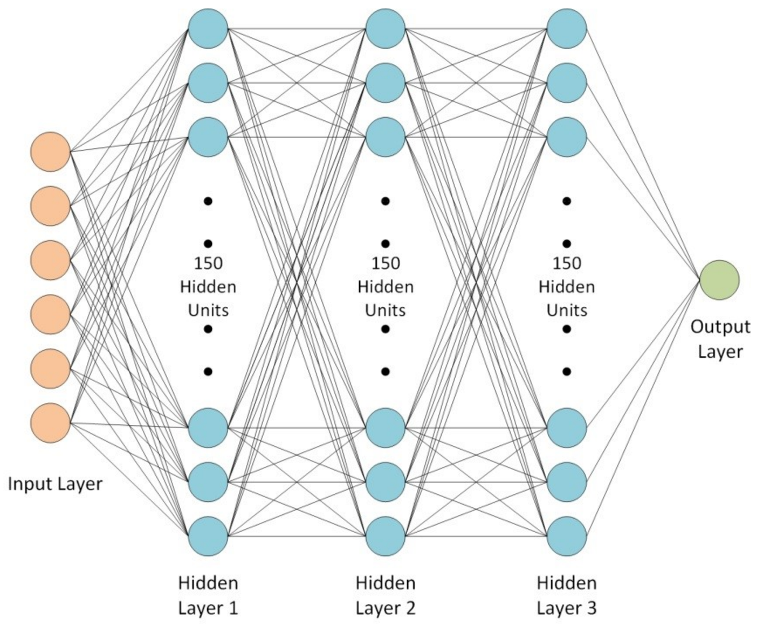

Figure 90. The structure of Multi-DisNet for the estimation of object distance from the multi-sensory system [120]

5.1.3 Performance Evaluation

The Multi-DisNet-based system for object distance estimation was evaluated on images recorded in different field tests. As first, testing data of the generated long-range dataset were processed by Multi-DisNet system and the results on the testing dataset are shown in Figure 91. As can be seen, the estimated object distances vary slightly around the ground truth distance.

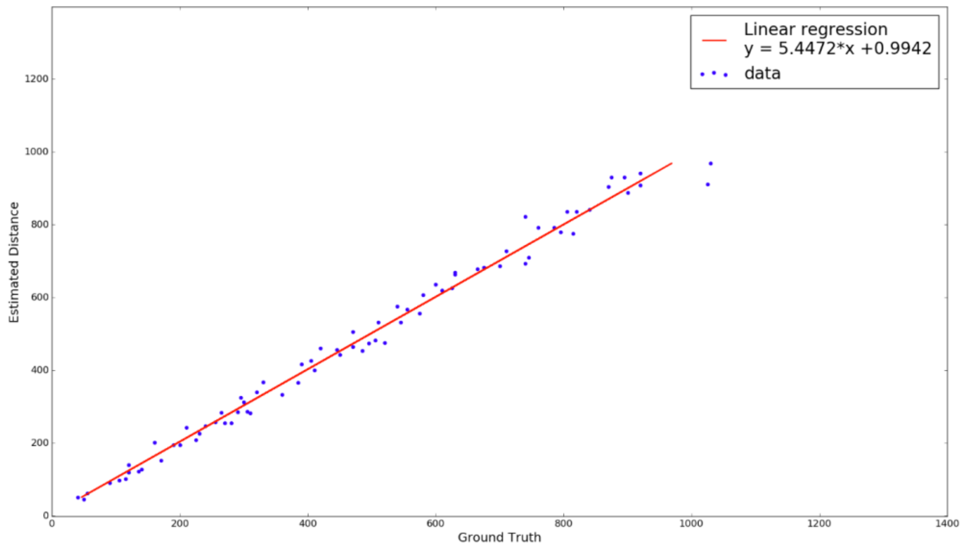

Figure 91. Ground truth vs estimated object distance from testing dataset [120]

The error in distance estimation is rather larger with larger distances and the calculated mean absolute error (MAE) was 22.76 m and root means square error (RMSE) was 34.09 m. These results demonstrate the ability of Multi-DisNet to estimate the long-range distance of up to 1000 m with an acceptable error.

Some of the results of the Multi-DisNet long-range object distance estimation in RGB and thermal images are given in Figure 92. The estimated distances to the objects (persons) detected in the images are given in Table 28. The object bounding boxes in the images were manually extracted so that an ideal object detector, able to extract bounding boxes of distant objects of very small size in the images, was assumed.

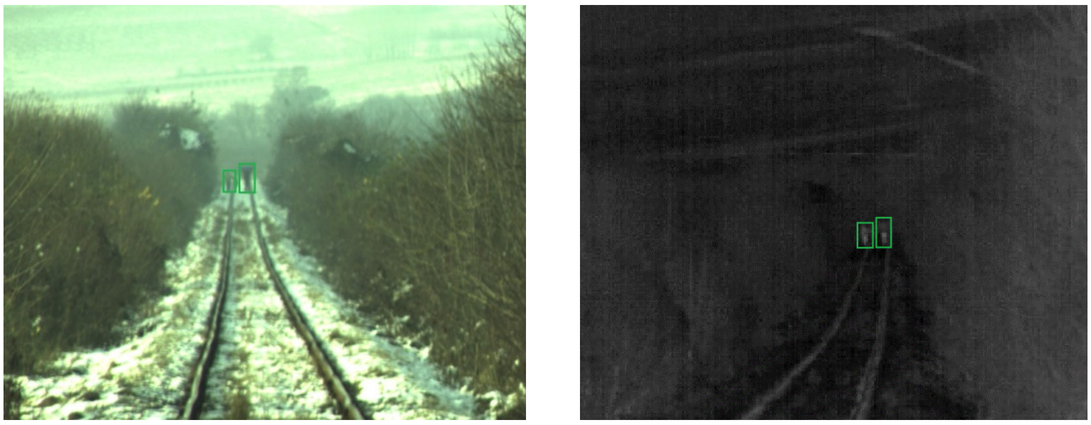

Figure 92. Manually detected objects in magnified RGB (left) and thermal images (right) from the long-range dataset field tests [120]

Table 28. Estimated distances vs Ground truth.

Object	Ground Truth	Multi-DisNet
Person 1	925 m	937.19 m
Person 2		899.25 m

In order to evaluate performances of the Multi-DisNet system with autonomous object bounding boxes extraction, the state-of-the-art computer vision object detector YOLO [70] trained with COCO dataset [89] was implemented in the Object Detector module. The images from the above described explained field tests were processed by YOLO and the resulted in YOLO objects bounding boxes were processed to calculate the Multi-DisNet input features, bounding boxes parameters. Based on the input features, the trained Multi-DisNet gave as outputs the estimated distances of the objects, persons on the rail tracks, to the camera sensors. It is important to note that images processed are those recorded while persons were walking along the rail tracks between the points of signalizations done for data set images recording, as explained in Section 3.1. Some of the results of the Multi-DisNet object distance estimation in RGB and thermal images are given in Figure 93. The estimated distances to the objects (persons) detected in the images are given in Table 29. Shown results illustrate the longest range achieved by YOLO, about 395 m, as YOLO detector failed to produce the object bounding boxes for distances larger than 395 m as the YOLO was trained with the COCO dataset, which contains objects only at a short distance to the camera.

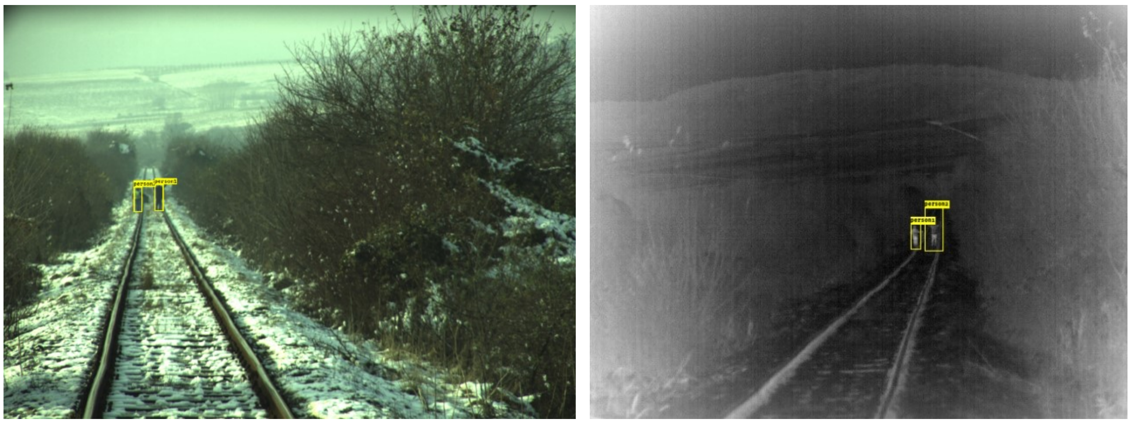

Figure 93. Object detected in RGB and Thermal images using the YOLO object detector [120]

Table 29. Estimated distances vs Ground truth

Object	Ground Truth	Multi-DisNet
Person 1	395 m	352.86 m
Person 2		408.25 m

Further sensor data for the Multi-DisNet evaluation purposes were recorded during the dynamic field tests [141]. The RGB and thermal cameras were mounted onto the moving locomotive Serbia Cargo type 444 pulling the freight train with 21 wagons on the Serbian part of the Pan European Corridor X to Thessaloniki (Greece) in the length of 120 km with a maximal train speed of 80 km/h. The cameras were mounted into specially designed housing as shown in Figure 94.

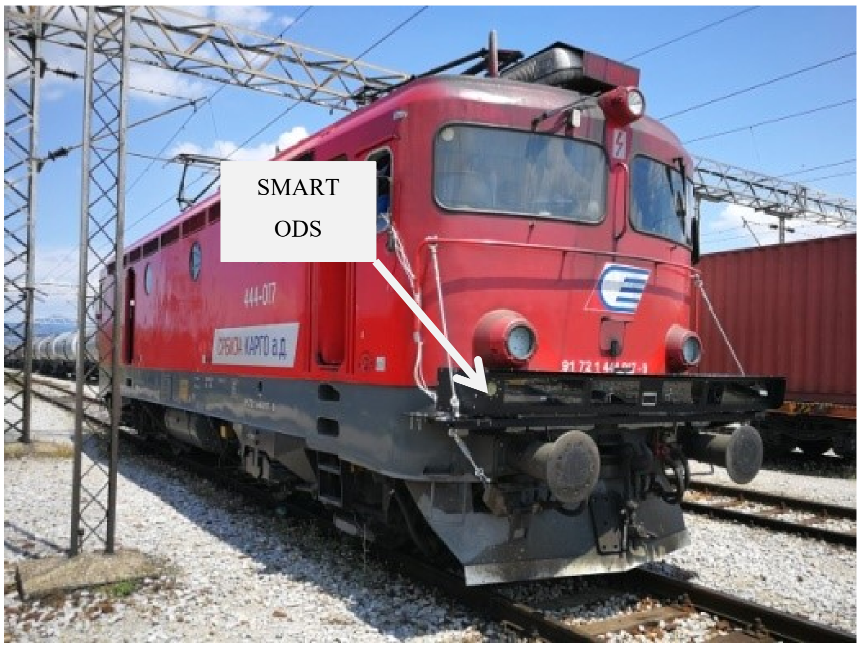

Figure 94. Vision sensors for obstacle detection integrated into sensors' housing mounted on the frontal profile of a locomotive below the headlights [120]

The sensors' housing was vibration isolated to prevent transmitting of vibrations from the locomotive onto the cameras as moving vehicle vibration can severely deteriorate the quality of acquired images. The vibration isolation system was designed with the rubber-metal springs [119] and it was suitable to suppress low-frequency vibrations providing almost 94% isolation efficiency for vehicle primary resonant frequency of 27 Hz. For frequencies above 50 Hz, the isolation efficiency was greater than 98%.

During the train run, onboard cameras recorded the data of the real-world rail tracks scenes in front of the locomotive. Example frames sequence of thermal images is shown in Figure 95. As can be seen, the example frames show the scene when a person accidentally crossed the rail track while the train was approaching. These frames were processed by YOLO object detector for person bounding box extraction. The extracted bounding boxes were processed for the extraction of bounding boxes parameters, inputs to Multi-DisNet, so that trained Multi-DisNet estimated distances to the detected object (person crossing the rail tracks). The distance estimation result is given in Table 30. However, as can be seen from Figure 95c, YOLO failed to detect object bounding boxes in the thermal camera frame. The cause for object detection failure in some of the thermal camera images was low images contrast due to lower camera performances influenced with high outside temperature during the dynamic field test of about 38°C. As the Multi-DisNet assumes input feature vectors of six elements where three elements represent features of the object bounding box in the thermal image it was necessary to estimate the object bounding box in thermal camera based on detected object bounding box in the RGB camera image. This assumption of the bounding box in the thermal image was done based on the relationship between the sizes of the objects bounding boxes in RGB and thermal images learned from the generated dataset. The corresponding object bounding boxes between the cameras highly correlate and show a linear relationship, which allows estimation of the missing bounding box in one camera as corresponding to the bounding box detected in the other camera. The results show how Multi-DisNet addresses the problem of object detection module failure to detect an object in one of the camera images. The trained Multi-DisNet estimated person distances to the cameras, which were mounted on the moving locomotive using the calculated features of originally detected object bounding boxes in RGB images and the features of estimated object bounding boxes in thermal images, from all subsequent cameras frames. The distance estimation result is given in Table 30. For the sake of better understanding of Multi-DisNet distance estimation accuracy, the ground truth distance in dynamic experiments was calculated offline using the relative GPS position of the train and the approximate GPS position of obstacle on Google Maps.

Table 30. Distance Estimation from Multi-DisNet in the dynamic experiment

Frames	Ground Truth (GPS)	Multi-DisNet
(a)	155 m	160.92 m
(b)	146 m	141.80 m
(c)	138 m	135.61 m

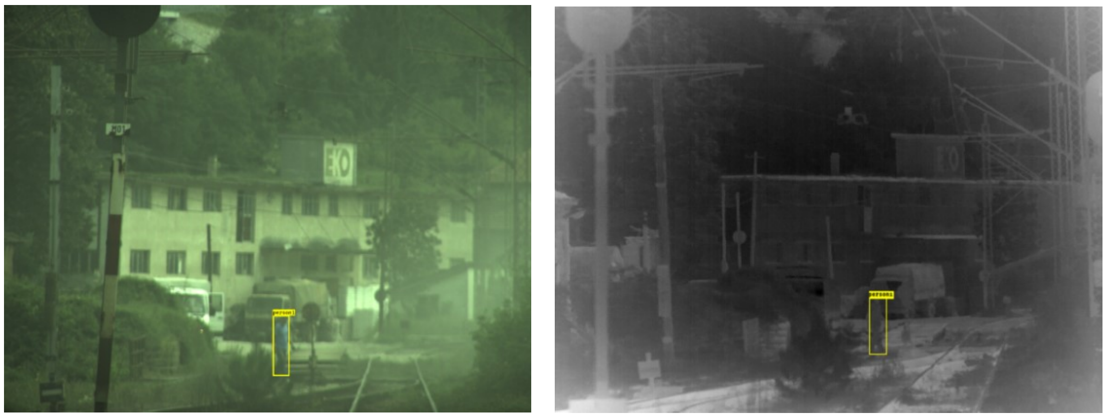

(a) subsequent synchronized frame 1

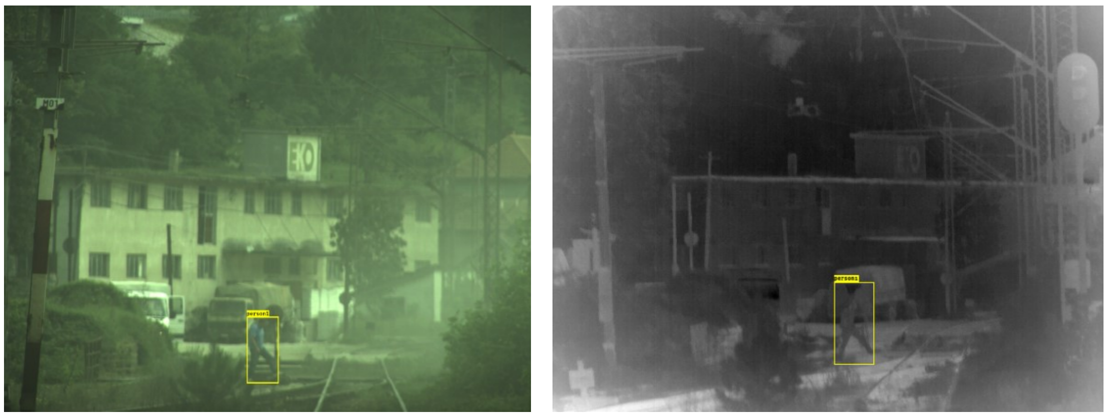

(b) subsequent synchronized frame 2

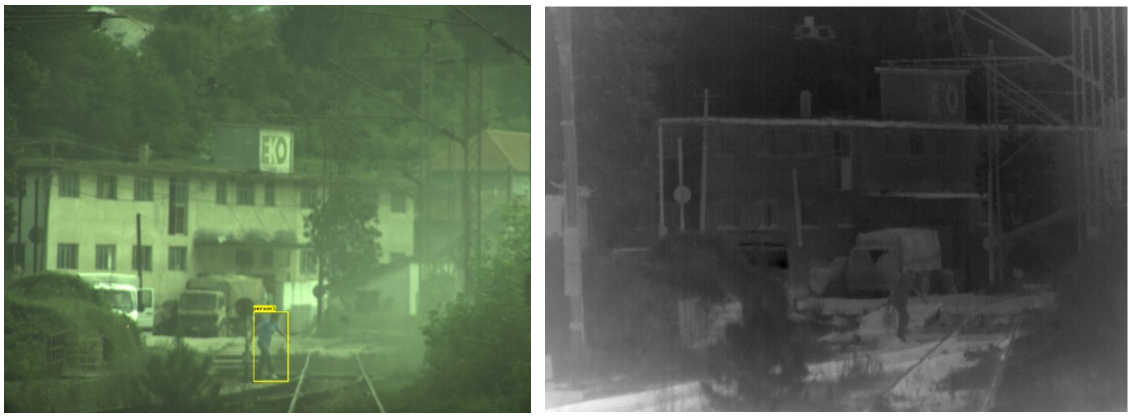

(c) subsequent synchronized frame 3

Figure 95. Three subsequent synchronized frames of RGB and thermal cameras of the scene with a person crossing the rail tracks accidentally, with the YOLO object bounding boxes overlaid. YOLO failed to extract the object bounding box in the last thermal camera frame.

5.1.3 Discussion

In this Thesis, a method for long-range obstacle detection from multiple monocular cameras is presented. The method is based on a novel multilayer neural network named Multi-DisNet that learns the relationship between the distance from the multiple cameras to the detected objects and the corresponding sizes of the objects in both camera images. The presented work is a part of the research and development of a novel integrated onboard obstacle detection system for railway applications. The presented system was evaluated for the setup consisting of an RGB and thermal camera.

This Thesis also presents the generation of the first long-range dataset reflecting the real-life railway applications, which was necessary for supervised training of the Multi-DisNet network to enable learning of the relationship between the sizes of the bounding boxes of the detected object in the camera's images and the distance of the object to the cameras. For the calculation of the object bounding boxes parameters, the Multi-DisNet distance estimation system assumes an Object Detector able to extract object bounding boxes. The evaluation results shown in this Thesis demonstrate the performance of the Multi-DisNet to reliably estimate the long-range distances in case the object bounding boxes are manually extracted. The system achieved long-range object detection of about 1000 m, which is the desired performance in applications such as railway applications. However, the evaluation results in the case of using the YOLO for automatic object detection demonstrated system performance of estimating the distance up to 400 m, as the YOLO object detector failed to extract the bounding boxes in long-range images. These results indicate the need for improvement of the object detection system module and need of training of object detector module with datasets consist of objects at a longer distance (small in size) in the future work, so to achieve reliable autonomous long-range obstacle detection. Nevertheless, the presented system reflects the novelty in long-range obstacle detection as current sensor technology in current land transport research is able to look some 200 m ahead [14] [142]. However, the required rail obstacle detection interfacing with loco control should be able to look ahead up to 1000 m detecting objects on and near track which may potentially interfere with the clearance and ground profile [143].

6. A machine learning based multiple object tracking

The environmental perception system, which performs object detection and tracking task, is the core for autonomous vehicles. Object detection tremendously evolves along with the advancement in sensor technology, and with the development of classical and machine learning-based algorithms, while multiple object tracking seems less developed [144]. Object tracking is essential for many tasks of autonomous driving such as obstacle avoidance and intention prediction [145]. It is a critical task and it becomes more challenging for situations such as objects at far distance, low frame rate video sequence, frequent occlusion, camera vibration or movement, and so on.

Mainly there are four object tracking methods categorized as region-based tracking [146], model-based tracking [147], contour-based tracking [148], and feature-based tracking [149]. All those methods rely on object detection. In general, tracking utilizes the detection information from previous frames to predict the detection in frames where detection is missing.

In [145] a traditional object tracking method based on a monocular camera for autonomous vehicles is present. By using the camera model to map pixel position into the distance, the distance to the vehicles with respect to the vehicle was measured. Further Kalman Filter (EKF) is used to refine distance accuracy and track detected vehicles. The results show that the method is capable to track 3D positions with sufficient accuracy.

Relatively modern machine learning-based methods [150] are introduced for object tracking based on Recurrent Neural Networks (RNNs) followed by long short-term memory (LSTM) and Gated recurrent units (GRU). The RNN based networks are often used for sequential data and thus also applicable for object tracking in video sequences.

6.1 DisNet-RNN Tracker: robust distance estimation and multiple objects tracking from a single camera

In this Thesis, a novel approach for multiple object tracking and distance estimation from an onboard monocular camera, aiming at improvements in the safety and security of railways, is presented. The approach is based on deep learning architecture using a deep Convolutional Neural Network (CNN) object detection followed by a multi hidden-layer Gated Recurrent Neural Network (RNN) referred to as DisNet-RNN Tracker, which consists of two sub-networks for distance estimation and bounding box prediction respectively. The DisNet-RNN Tracker learns and estimates the distance between the detected object and the camera sensor, and predicts the object bounding box based on sequential input from previous and current detection. The presented DisNet-RNN Tracker tracks multiple objects in case where the object detection module fails to detect an object. The presented method is evaluated on the real-world railway dataset recorded with the onboard Obstacle Detection System developed within an H2020 Shift2Rail project SMART - Smart Automation of Rail Transport. The presented work has the potential to benefit other applications where reliable object detection, tracking, and long-range distance estimation are needed such as autonomous cars, transportation, and public security.

The workflow of DisNet-RNN Tracker based object detection, tracking, and distance estimation from a single monocular camera is illustrated in Figure 96. The frames captured by an RGB monocular camera are inputs to Object Detector Module. Different object detectors, which outputs bounding box and class of detected objects, can be integrated into the system. The resulted object bounding boxes from the detection module further feed into the Multiple Objects Mapping (MOM) module. The object mapping module matches previous object detection results to the current detection results for the sake of objects tracking and assigning unique IDs for unmatched or newly detected objects. Further, the Features Calculation module extracts features of the objects bounding boxes and based on those features DisNet-

RNN Tracker estimates object distance at the current frame and predicts object bounding box in the next frame. In the system architecture in Figure 96, an example of the distance estimation and bounding box prediction based on prior detection information for a human walking along the rail tracks is shown.

In this Thesis, the YOLO object classifier [70] trained with the COCO dataset [89] is considered as an object detector module, whereas any other state-of-the-art object detector can be used. However, no matter which state-of-the-art object detection module is used, false detection or unprecise bounding boxes extraction cannot be avoided in cases such as object partially or fully occluded, object shadow, change in image quality due to illumination and the similarity of object texture or colour with the background. This problem is unfavourable for those applications where high reliability is demanded such as obstacle detection systems for autonomous vehicles. DisNet-RNN Tracker, proposed by Haseeb et al. in [151], aims at reliable overall object distance estimation and object tracking in spite of the failure of the intermediate object detector module.

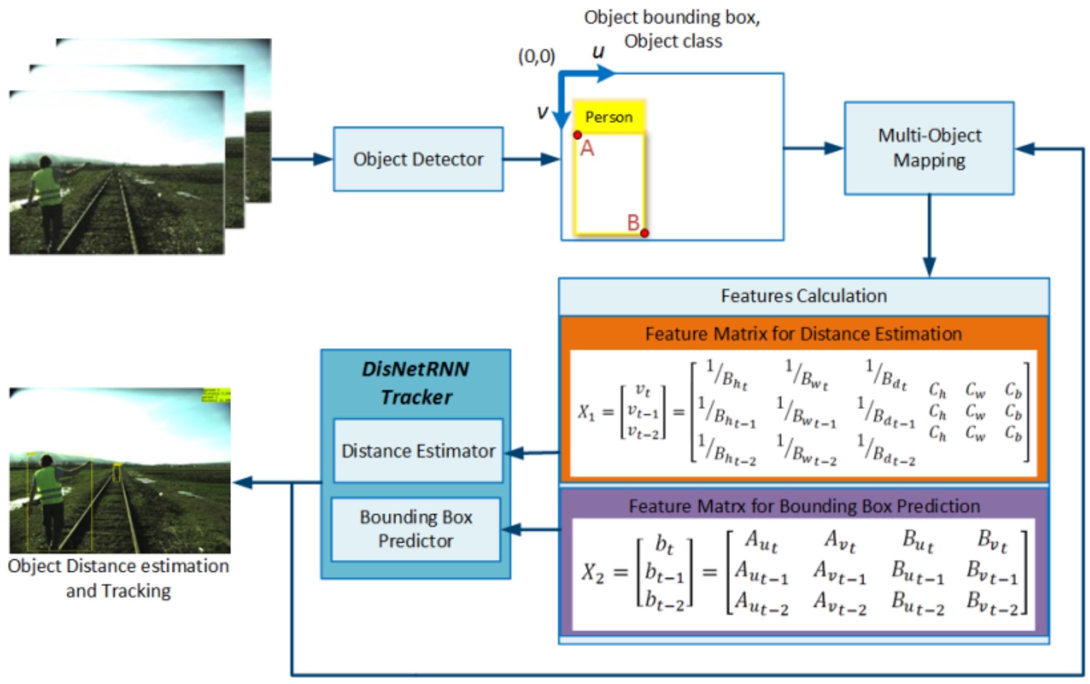
Object bounding box,
Object class
(0,0)
u
v
Person
A
B
Object Detector
Multi-Object Mapping
Features Calculation
Feature Matrix for Distance Estimation
$X_1 = \begin{bmatrix} v_t \\ v_{t-1} \\ v_{t-2} \end{bmatrix} = \begin{bmatrix} 1/B_{h_t} & 1/B_{w_t} & 1/B_{d_t} & C_h & C_w & C_b \\ 1/B_{h_{t-1}} & 1/B_{w_{t-1}} & 1/B_{d_{t-1}} & C_h & C_w & C_b \\ 1/B_{h_{t-2}} & 1/B_{w_{t-2}} & 1/B_{d_{t-2}} & C_h & C_w & C_b \end{bmatrix}$
Feature Matrx for Bounding Box Prediction
$X_2 = \begin{bmatrix} b_t \\ b_{t-1} \\ b_{t-2} \end{bmatrix} = \begin{bmatrix} A_{u_t} & A_{v_t} & B_{u_t} & B_{v_t} \\ A_{u_{t-1}} & A_{v_{t-1}} & B_{u_{t-1}} & B_{v_{t-1}} \\ A_{u_{t-2}} & A_{v_{t-2}} & B_{u_{t-2}} & B_{v_{t-2}} \end{bmatrix}$
DisNetRNN Tracker
Distance Estimator
Bounding Box Predictor
Object Distance estimation and Tracking

Figure 96. DisNet-RNN Tracker based object distance estimation and tracking system from a monocular camera [151]

6.1.1 Deep Learning Network architecture

The DisNet-RNN Tracker consists of two independent sub-networks based on Recurrent Neural Network (RNN) architecture. The reason to use RNN is that due to its unique characteristic of being suitable to work with sequential data and its memory cell able to preserve information from inputs provided in previous time moments [150]. In the scenario considered in this Thesis, two types of object detection failures are possible: the target objects are not detected in some frames, and the bounding boxes of some of the detected objects are not accurate. Using the RNN, which has a memory of previous inputs, can help to predict the object position and estimate distance more reliably. DisNet-RNN Tracker uses the sequential data from previous two-time steps to improve the estimation of the object distance at the current time step and predicts the position and size of the object bounding box in the next time step.

Figure 97 shows the DisNet-RNN Tracker architecture. The architecture consists of two subnetworks represented with two main blocks one under the other in Figure 97. The upper network is used to estimate the object distance named as *distance estimator* and the lower network named as *bounding box predictor* is used to predict the top left corner A, and the bottom right corner B, of the object bounding box. Prediction of these two bounding box corners' points relates to the prediction of the bounding box position and size.

As shown in Figure 97, a three hidden layers network was adopted for the distance estimation. A deep recurrent neural network is stacked with Gated Recurrent Unit (GRU) layers and the output from the last GRU layer is connected to a fully connected output layer to perform final distance estimation. For the bounding box prediction, the network consists of a single hidden layer of GRUs with a fully connected layer as an output layer. A new loss function in training *distance estimator* network was defined and it is given in (6-1). This loss function calculates losses from all distance prediction results from three time-steps and in a similar way, the Mean Absolute Error (MAE) loss function for the *bounding box predictor* network was defined given in (6-2).

$$loss\ function = \frac{1}{3n}\sum_{i=1}^{3}\sum_{j=1}^{n}\left|Y_{ij-true} - Y_{ij-estimated}\right| \qquad (6\text{-}1)$$

$$
\begin{aligned}
&loss\ function \\
&\quad = \frac{1}{3n}\sum_{i=1}^{3}\sum_{j=1}^{n}\left|Au_{ij-true} - Au_{ij-predicted}\right| \\
&\quad + \left|Av_{ij-true} - Av_{ij-predicted}\right| \\
&\quad + \left|Bu_{ij-true} - Bu_{ij-predicted}\right| \\
&\quad + \left|Bv_{ij-true} - Bv_{ij-predicted}\right|
\end{aligned}
\tag{6-2}
$$

where:

- n : training data numbers
- $Y_{ij-true}$: the ground truth distance of j_{th} training data at time step *i*.
- $Y_{ij-estimated}$- the estimated distance of j_{th} training data at time step *i*.
- $Au_{ij-true}$, $Av_{ij-true}$: the top-left corner coordinates of ground truth object bounding box of j_{th} training data at time step *i*.
- $Bu_{ij-true}$, $Bv_{ij-true}$: the bottom-right corner coordinates of ground truth object bounding box of j_{th} training data at time step *i*.
- $Au_{ij-predicted}$, $Av_{ij-predicted}$: the top-left corner coordinates of predicted object bounding box of j_{th} training data at time step *i*.
- $Bu_{ij-predicted}$, $Bv_{ij-predicted}$: the bottom-right corner coordinates of predicted truth object bounding box of j_{th} training data at time step *i*.

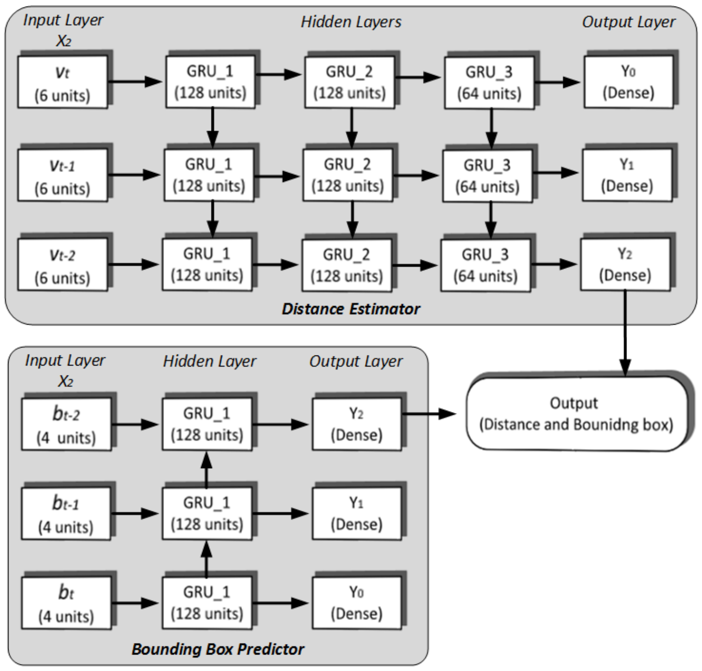

Figure 97. DisNet-RNN Tracker Architecture consists of two sub-networks namely distance estimator on top and bounding box predictor in bottom [151]

6.1.2 Dataset

Recurrent Neural Networks requires a sequential dataset that needs to be prepared before training DisNet-RNN Tracker. As described earlier, DisNet-RNN Tracker consists of two sub independent RNN networks. In order to train and test these subnetworks, manually a dataset of the size of 8000 sequential inputs was created using images recorded in real-world railways scenarios. Each sample of the dataset represents extracted features from three subsequent frames. The annotation tool [14] provides the object bounding boxes coordinates, which were labelled together with ground truth distance. The ground truth for distance estimation network was recorded during the dataset generation using the GPS positioning system which later in the offline phase allows calculating the relative distance between train and objects. Whereas for bounding box prediction, the manually drawn bounding box on the fourth frame is considered as a ground truth as shown in Figure 98.

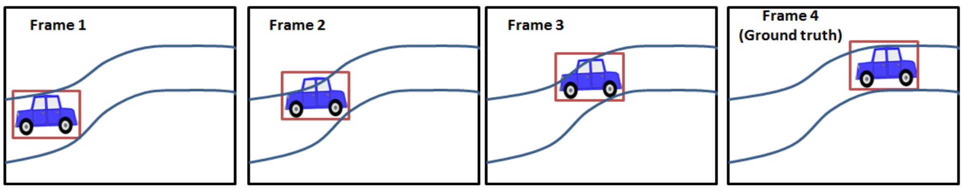

Figure 98. Dataset generation for bounding box prediction [151]

In the next section, it is explained how the features were calculated and the dataset was organized to train the DisNet-RNN Tracker, to learn distance estimation and bounding box prediction.

6.1.3 Features selection

As it is known from the projective transformation, the object's size in the camera image is inversely proportional to the object's distance from the camera. The *distance estimator* network, trained to learn the relationship between the changes in sizes of the objects' bounding boxes in an image with respect to change in the distances between the objects and the camera over time. The dataset for network *Distance Estimator*, organized in the form of a two-dimensional feature matrix X_1 for distance estimation is given in (6-4), where each matrix row represents the six features of the feature vector $\boldsymbol{v}$ of an object at time-steps *t*, *t*-1 and *t*-2 respectively. Vector $\boldsymbol{v}$ was calculated from manually annotated objects' bounding boxes for a class label as:

$$\boldsymbol{v} = [1/B_h \ 1/B_w \ 1/B_d \ C_h \ C_w \ C_b] \quad \text{(6-3)}$$

- B_h: height of the object bounding box in pixels/image height in pixels
- B_w: Width of the object bounding box in pixels/image width in pixels
- B_d: diagonal of the object bounding box in pixels/image diagonal in pixels
- C_h, C_w, and C_b: average height, width and length of each object class in meters

C_h, C_w, and C_b are defined as unique features that actually represent different classes. These features generalize the network to learn distance vs bounding box relation for multiple object classes. For example, the predefined features for object class person are the average height, width, and breadth of the humans, and similarly, these features were predefined for other classes. These features do not have any meaning and contribution to distance learning but help to differentiate different object types.

Similarly feature matrix X_2 was calculated for network *Bounding Box Predictor*. Each row in X_2 matrix represents coordinates of the top left corner *A* and the bottom right corner *B* of an object bounding box at time-steps *t*, *t*-1 and *t*-2 respectively, where (*u*,*v*) are image point coordinates.

$$X_1 = \begin{bmatrix} \boldsymbol{v}_t \\ \boldsymbol{v}_{t-1} \\ \boldsymbol{v}_{t-2} \end{bmatrix} = \begin{bmatrix} {}^{1}/_{B_{h_t}} & {}^{1}/_{B_{w_t}} & {}^{1}/_{B_{d_t}} & C_h & C_w & C_b \\ {}^{1}/_{B_{h_{t-1}}} & {}^{1}/_{B_{w_{t-1}}} & {}^{1}/_{B_{d_{t-1}}} & C_h & C_w & C_b \\ {}^{1}/_{B_{h_{t-2}}} & {}^{1}/_{B_{w_{t-2}}} & {}^{1}/_{B_{d_{t-2}}} & C_h & C_w & C_b \end{bmatrix} \tag{6-4}$$

$$X_2 = \begin{bmatrix} \boldsymbol{b}_t \\ \boldsymbol{b}_{t-1} \\ \boldsymbol{b}_{t-2} \end{bmatrix} = \begin{bmatrix} A_{u_t} & A_{v_t} & B_{u_t} & B_{v_t} \\ A_{u_{t-1}} & A_{v_{t-1}} & B_{u_{t-1}} & B_{v_{t-1}} \\ A_{u_{t-2}} & A_{v_{t-2}} & B_{u_{t-2}} & B_{v_{t-2}} \end{bmatrix} \tag{6-5}$$

In order to make DisNet-RNN Tracker more robust as well as to make it also work in the situations where an object is detected in one or two subsequent frames and not only in three subsequent frames, the dataset shall be augmented and extended with modified feature matrices (6-5). Namely, as mentioned earlier, each row of the matrix X_1relates to time-steps *t*, *t*-1 and *t-2.* By zero-padding of the first and the second row, the modified feature matrices are:

$$X_1 = \begin{bmatrix} & & 0 & & & \\ & & 0 & & & \\ {}^{1}/_{B_{h_t}} & {}^{1}/_{B_{w_t}} & {}^{1}/_{B_{d_t}} & C_h & C_w & C_b \end{bmatrix} \tag{6-6}$$

$$X_1 = \begin{bmatrix} & & 0 & & & \\ {}^{1}/_{B_{h_t}} & {}^{1}/_{B_{w_t}} & {}^{1}/_{B_{d_t}} & C_h & C_w & C_b \\ {}^{1}/_{B_{h_{t-1}}} & {}^{1}/_{B_{w_{t-1}}} & {}^{1}/_{B_{d_{t-1}}} & C_h & C_w & C_b \end{bmatrix} \tag{6-7}$$

In the same way, the extended dataset is generated for the feature matrix X_2. Using the extended datasets means that the network does not need to wait for an object to be detected in three continuous frames in time to predict the distance.

6.1.4 Training and testing phase

The dataset generated contains 8000 samples which were randomly split into training data 80%, validation data 10% and test data 10%. DisNet-RNN Tracker sub-networks were trained with Adam optimizer and with a learning rate of 1e-4. During the training, a mini-batch gradient descent algorithm with a minibatch size of 100 and an Early Stop technique with 20 tolerant epochs has been used. Finally, after 246 training epochs, the mini loss on the test dataset according to equation 6-1 was 1.28.

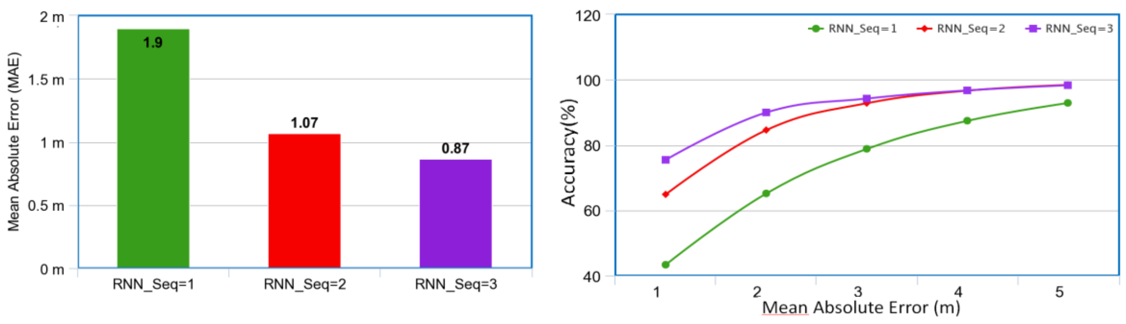

Figure 99. Left: Mean Absolute Error (loss) in distance estimation of DisNet-RNN Tracker for detection in 1, 2, and 3 subsequent frames. Right: Distance Accuracy vs Different mean absolute error [151]

Figure 99 illustrates that with the use of more previous detection results, the mean square error reduces. This assures that the sequential input data really help in the estimation of distance and also shows the performance of a trained model when the object is detected in three subsequent frames, two subsequent frames, and only in one frame refer as RNN_Seq = 3, 2 and 1 respectively.

Besides mean absolute error (loss), another measurement parameter, distance accuracy Acc, is defined in equation (6-8). In Figure 99, the accuracy vs mean absolute error plots help to understand the advantage of using sequential data. An estimation is considered accurate in $Acc_j$when estimation distance is in the range [y_{true-i} -j, y_{true-i}+ j]. Where j is Mean Absolute Error in the range of 1 to 5.

$$Acc_j = \frac{1}{n}\sum_{i=1}^{n}(|y_{true-i} - y_{estimated-i}| \leq j) \qquad (6\text{-}8)$$

From the comparison results Table 31, it is clear that the performance of DisNet-RNN Tracker with more sequential input (previous detection results) is more accurate than using less sequential input. Similar results for the bounding box prediction network were obtained hence not included in this section.

Table 31. Comparison result of DisNet-RNN Tracker Accuracy at different MAE

	Acc1 (%)	Acc2 (%)	Acc3 (%)	Acc4 (%)	Acc5 (%)	MAE (m)
RNN_Seq =1	43.31	65.16	78.82	87.45	92.89	1.90
RNN_Seq =2	64.87	84.59	92.82	96.67	98.43	1.07
RNN_Seq =3	75.45	89.98	94.24	96.74	98.32	0.87

6.1.5 Multiple Object Mapping (MOM)

Another problem needs to be solved before DisNet-RNN Tracker can be used in object tracking. The multiple detected objects in the current frame need to be associated with the multiple detected objects in previous frames to form sequential data (6-6) and (6-7), which is input to DisNet-RNN Tracker. Therefore, a Multiple Object Mapping (MOM) module is introduced to perform object association and generate sequential feature matrices for DisNet-RNN Tracker. The MOM module calculates the Intersection Over Union (IOU) of current detected and previously detected objects and based on high correlation associate the objects. The entire working of the MOM module is shown in Figure 100. If the objects do not correlate then MOM initialises the new tracker for newly detected objects and assigns a unique ID.

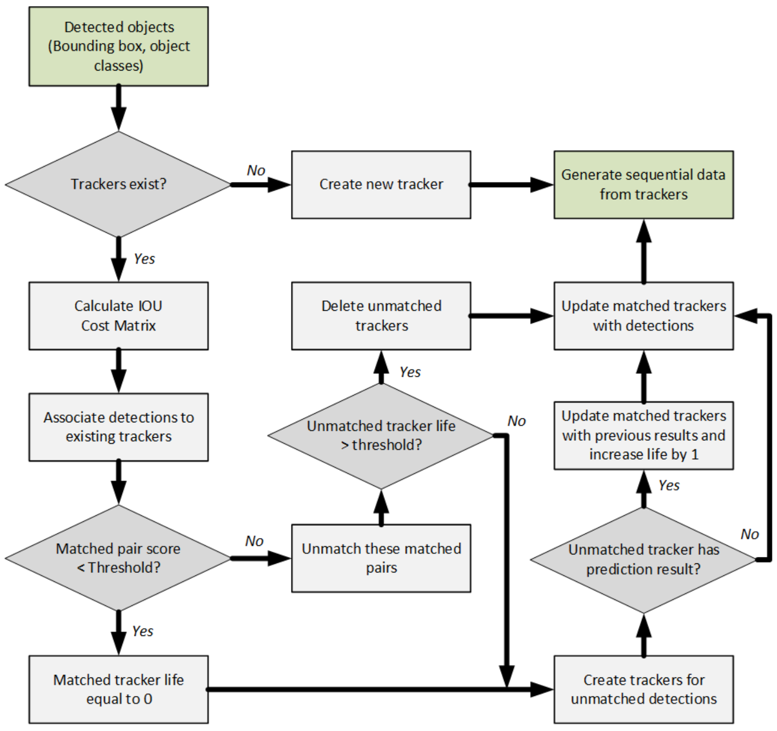
Detected objects (Bounding box, object classes)
Trackers exist?
No
Create new tracker
Generate sequential data from trackers
Yes
Calculate IOU Cost Matrix
Delete unmatched trackers
Update matched trackers with detections
Yes
Associate detections to existing trackers
Unmatched tracker life > threshold?
No
Update matched trackers with previous results and increase life by 1
Yes
Matched pair score < Threshold?
No
Unmatch these matched pairs
Unmatched tracker has prediction result?
No
Yes
Matched tracker life equal to 0
Create trackers for unmatched detections

Figure 100. Multiple Object Mapping based object association of current detected objects and previously detected objects

6.1.6 Evaluation

The DisNet-RNN Tracker based system for distance estimation and object tracking was evaluated on images recorded by an RGB monocular camera mounted on the frontal profile of the moving freight train during the field tests within H2020

Shift2Rail project SMART. The RGB camera from The Imaging Source [152] provides images with the maximum resolution of 2592x1944 at 2 FPS.

Figure 101 shows the performance of DisNet-RNN Tracker on six subsequent frames from a video of a real-world dynamic railway scene with a truck parked in the rail track area (vehicle 3), which is a potential intrusion, and a van (vehicle 4) crossing the unsecured crossing while the train is approaching the crossing. The estimated distance to the vehicle objects from the camera (i.e. from the locomotive), object class, and tracking ID are shown in the left upper corner of each frame. The detection/prediction of the objects is marked by the object bounding boxes. The blue and brown coloured bounding boxes represent the prediction results, achieved by DisNet-RNN Tracker, whereas the red bounding boxes represent the object detection results of the YOLO object detection. As it is evident, the DisNet-RNN Tracker is able to track the object (vehicle 3), to predict its bounding box and to estimate the distance even in the case object is occluded by the other vehicle (frames 2 and 3) and YOLO object detector failed. Moreover, the YOLO object detector failed even in the case of a fully visible object (vehicle 3) in frame 6, whereas the proposed DisNet-RNN Tracker achieved the object bounding box prediction and distance estimation.

During the train run, the ground truth was also measured using relative GPS positions of the objects (from the google maps) and the train (GPS on the train). According to the ground truth distance, the van (vehicle 3) and truck (vehicle 4) were approximately 45 meters apart. The ground truth distances to the van were measured as 135m, 128 m, 123m, 120m, 117m and 108m respectively for six subsequent frames shown in Figure 99. Hence, the estimated distance from DisNet-RNN Tracker in comparison with the ground truth demonstrates also reliability of the proposed method.

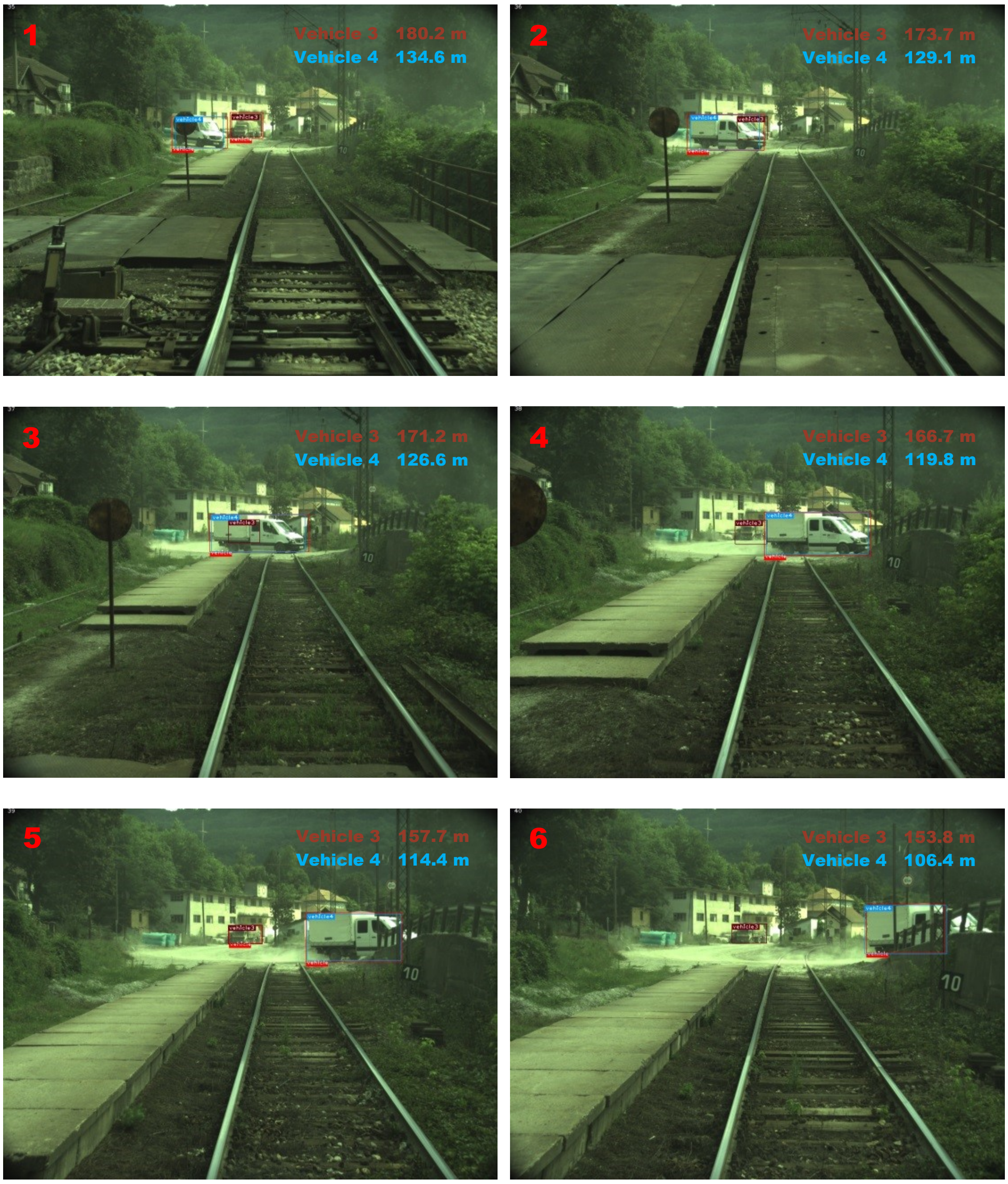

Figure 101. A real-world scene where truck is parked near rail track and the van crossing the rail track while train approaching [151]

6.1.7 Discussion

Object tracking and distance estimation are crucial for safety-critical applications such as obstacles and track intrusion detection in railways. The use of information from previous object detections improves the distance estimation and also enables the tracking of objects by prediction of the object's position in frames in which the object detector fails.

In this Thesis, DisNet-RNN Tracker consists of two sub-independent networks named *distance estimator* and *bounding box predictor* is presented. Gated Recurrent Neural Network architecture is chosen for object distance estimation and object tracking. By using a monocular camera, the presented method can precisely track and estimate the distance to the target objects as shown by the evaluation results from a real-world railway scenario. However, the proposed object distance estimation system still has several limitations such as object occlusion for a longer period introduces an error that increases with time. So dependency on prediction results for a longer period is not recommended, as the error increases with time until the estimation is corrected by the detection.

Some efforts could be made in the following aspects in order to improve the performance and conquer the drawbacks of presented distance estimation and object tracking system. Moreover, for the improvement of distance estimation and object tracking, the dataset needs to be extended, for long.-range detection and tracking of multiple objects.

7. Real-time Performance Evaluation

The basic need to detect and estimate the distance of various obstacles on the rail tracks in real-time is a big challenge. In this chapter, the main development and performance characteristics of proposed object detection, tracking, and distance estimation methods in real-time are presented. The focus is on vision-based obstacle detection system as in the final realization of ODS, vision sensors (cameras) were used for mid- and long-range obstacle detection in the operational environment. Real-time systems (RTS) are defined as hardware and software-based systems that assure the system response within the specified time constraints. The required "event-to-response time", or in other words, "system response time" depends on many factors. For example, in a high-speed machine vision application where the system is physically moving fast or the capturing scene is moving fast, many factors such as processing time and hardware selection, to be taken into account during the development of such systems.

A challenging machine vision application is a highly bandwidth-demanding application which brings a considerable amount of data streams from a vision sensor to the processing unit. The obstacle detection system requires a high-bandwidth and low latency network to connect all cameras to the central processing unit. Based on the nature of the application, during the development of real-time Obstacle Detection System (ODS) for rail transport, both challenges were presumed, high-speed and high-bandwidth. In the next section, the requirements of the ODS system discussed in detail.

7.1 Requirement Analysis

The requirements to make SMART ODS real-time grouped in two main categories: high processing speed and high bandwidth requirements as listed below.

High processing speed:

1. ODS mounted on a moving freight train running at 80 km/h, which is a speed of a conventional freight train.
2. Train-stopping distance of approximately 700 meters for the above-mentioned speed according to the regulations.
3. Moving or continuously changing scene/environment

High bandwidth:

1. Mid-range (up to 200 m) and Long-range (up to 1000 m) obstacle detection requires high-resolution images to enable distant objects' visibility in the image.
2. Simultaneous data acquisition from multiple vision sensors.

Based on the factors mentioned above the minimal required response time and bandwidth analysis were performed as described in the following sections.

Minimum requirement approximation:

In order to estimate the minimum requirement of ODS, let's assume a freight train moving at 80 km/h (22.22 m/s) on a straight rail track. According to railway regulations, the stopping distance of the freight train for speed of 80 km/h is about 700 meters.

The required event-to-response time t_{res} (time required by perception module) should be less than the data acquisition time t_{acq}, which means the system should be able to process the captured data (camera frame) and response before the acquisition of the next subsequent frame:

$$t_{res} < t_{acq} \tag{7-1}$$

$$t_{process} = t_{acq} + t_{res} \tag{7-2}$$

The stopping distance d_{stop} and stopping time t_{stop} of the train equipped with ODS while running with speed v can be calculated as:

$$t_{stop} = t_{process} + t_{braking} + t_{delay} \tag{7-3}$$

$$d_{stop} = v \cdot t_{stop} \tag{7-4}$$

Where $t_{braking}$ refers to the time required to stop the train after the brake engagement fully, t_{delay} refers as driver reaction time after the ODS system warning and $\boldsymbol{t_{process}}$ can be defined as total processing time, i.e. time required by the hardware and software components to deliver output from the moment at which the event occurred.

However, the braking time $t_{braking}$ depends on many physical factors of the train itself [153]:

1. the speed of the train at the time when the brakes are engaged;
2. the deceleration rate available with a full-service brake application, which varies according to the coefficient of friction between wheel and rail;
3. the delay from when the train driver commands the brakes to when they are become effective (brake delay time);
4. the state of the wear of the brake pads and the air pressure available in the brake cylinders;
5. the geography of the track, in particular, the track gradient the train travels over from when the brakes commanded to where the front of the train stops;
6. the mass distribution of the train.

7.2 Hardware

A real-time obstacle detection system for operational trains can be challenging to implement as a PC computer-based system because of the needed potential for high computational cost and algorithm complexity.

Emerging embedded vision system-based solutions for robotics and security applications allow swift processing information and taking appropriate actions. Such systems show high performance, high accuracy while requiring low energy consumptions. Despite high demanding needs, in work for prototyping the ODS, a PC computer-based system was considered for real-time implementation because it was sufficient to meet the prototype system requirement. In order to cope with object detection and distance estimation as a computationally expensive task, hardware-specific optimisations of the proposed algorithms were performed, that allow the algorithms to run in real-time. The hardware contains three parts: Sensors, Network, and Processing Unit which are explained in the next sections.

7.2.1 Sensors

ODS consists of 5 vision sensors including three RGB zooming cameras from the Imaging Source, thermal camera from FLIR, night vision sensor consisting of custom-made night vision lens mounted on a monochrome camera from The Imaging Source (section 3.1.1). Some specifications of sensors given below which also considered during the selection and designing of the network and processing unit.

Table 32. Vision Sensors

Vision Sensor	Resolution (Pixels)	Frequency (Hz)	Size (Megapixels)
RGB	2592x1944	15	5MP
Thermal (TH)	640x512	9	0.328MP
Night Vision (NV)	2592x1944	15	5MP

7.2.2 Network

The minimum requirements estimation and selection of the network hardware is crucial for applications such as SMART ODS which characterised with the extensive size data and high speed. In SMART ODS due to the large size of images, a high bandwidth network was needed. As described in Section 3.1, the original network setup is based on a gigabit network. However, during sub-system conformance testing it was established that a gigabit network is not sufficient to enable real-time sensor connection, and consequently, it was decided to increase the network bandwidth to 10 GB network. This had as a consequence a change of the network switch from originally planned ADVANTECH EKI-9512P to NETGEAR XS708T [154]. The selected industrial 10GB network switch was chosen to overcome the problem of data overflowing and to enable getting the maximum resolution images at high speed.

The SMART networks receive data about 7 Hz at maximum resolution simultaneously from all sensors. However, further the software-based data synchronization lower down the data acquisition to 2 Hz. The hardware or software-based synchronisation is needed to synchronised data captured independently from SMART vision sensors at 7 Hz, in order to process the same scene captured by all vision sensors. This downsampling of acquired data does not affect the real-time performance of SMART ODS and provides enough information.

Considering the train speed of 80 km/h, the data acquisition frame rate was set to 7 FPS (frame per 143 milliseconds) which means that at about every 3 meters travelled distance the new data has been captured. Whereas the actual processing is done on two frames out of seven captured frames meaning that SMART ODS processes an image taken at every 500 milliseconds or in other words at every 11.11 meters travelled distance.

7.2.3 Processing unit

Machine learning-based algorithms for obstacle detection and distance estimation require a high-performance processing unit to enable real-time processing. Because of the different sizes in which objects may appear in the image, the large image search space is involved in object detection algorithms, which increases the complexity and slows down the overall performance of SMART ODS real-time implementation.

SMART PC-computer based processing unit was used for the real-time obstacle detection system prototyping. The processing unit was equipped with INTEL core i9 CPU and two Nvidia GTX 1080 16 GB GPUs (graphics processing units). Parallel GPUs computing enable real-time object detection and distance estimation.

7.3 Software

ODS software architecture developed on the Robot Operating System (ROS) [121] distribution Kinetic Kame operated on a Linux operating system (Ubuntu 16.04 64-bit, http://releases.ubuntu.com/16.04/). During developing hardware and software for SMART the goal was to achieve high reliability, modularity, redundancy, performance, speed and redundancy characteristics for SMART ODS.

The ROS works here as middleware that provides the virtual interface between different software modules such as data acquisition, object detection, distance estimation, visualisation and offline processing modules (Figure 102).

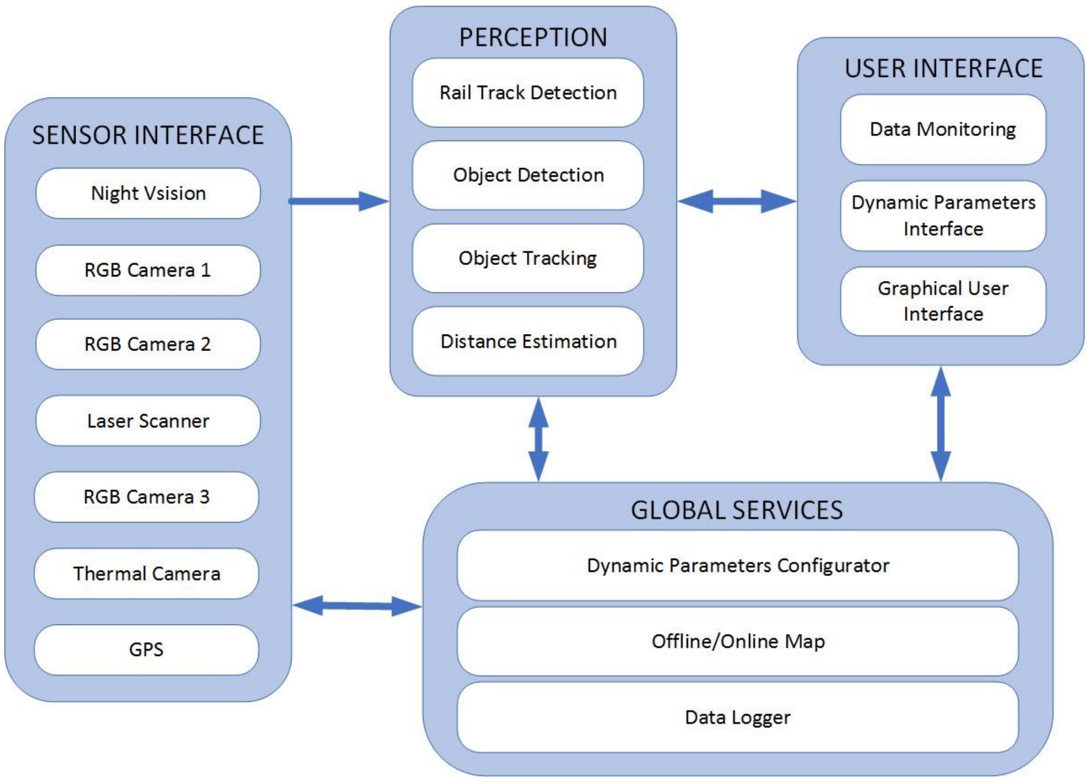

Figure 102. Block-diagram of ROS-based software architecture of SMART ODS

ROS messaging middleware [155] provides an Inter-Process Communication (IPC) or shared memory. The IPC mechanism of subscriber/publisher enables intercommunication between modules and sub-modules.

Sensor interface module: The sensor interface module is responsible for providing data from sensors to other modules. Each sensor has its own dedicated data acquisition interface. Besides providing data from the sensors, the sensor interface modules are also responsible for sensor parameters configuration during pre-run test and during run. This means it is not needed to completely stop the SMART ODS in case changing any sensors parameters, the parameters can be changed while SMART ODS is running and train is moving. The user can change the sensors parameters using Dynamic Parameters Interface as shown in Figure 2. The user interface interacts with dynamic parameters configurator, which further passes user's configuration changes to sensor interface modules. Some of the parameters possible to change are: camera FPS, exposure time, field of view, resolution.

Perception module: the received sensors data after data synchronisation are further processed on machine learning and computer vision-based perception module. The perception module is the core building block of the whole SMART ODS software framework and it is responsible for processing the raw data from sensors and for providing the meaningful information, i.e. rail track detection (ROI), objects detection, recognition, tracking and distance estimation.

Global services module: this module includes data logging module that is capable of recording the raw data from sensors, parameters configuration, sensors parameters and processed data. The recorded data can be retrieved to analysis the performance of SMART ODS for further improvement and development. Further, the global service module includes map, which together with GPS sensor input [118], is used to visualize real-time position of the train on the map. The map can be set up in offline mode that means the pre-saved map can be used if internet service is not available. However, the online mapping can also be done when access to internet is possible.

User interface module: the user interface module includes visualization of all processed information from perception module and real-time positioning of the train on the map. The user interface assists and facilitates the driver by providing information regarding the obstacles on the rail tracks. The information on the user interface is designed to only alert the driver, who is still responsible to make the front-end decision. Further, the user interface provides the control interface for the responsible ODS technician to troubleshoot the problems, configure parameters and monitor sub-system modules.

7.3. Machine learning-based algorithms timing considerations

Machine learning has a fundamental role in SMRT ODS software development. The machine learning algorithms were developed under the Keras API (https://keras.io/) running on top of Tensorflow development kit (https://www.tensorflow.org/). The Tensorflow is one of the widely used frameworks due to its high performance and processing speed in comparison to other available frameworks. Tensorflow based machine learning algorithms were optimized in a way to have high processing rate to achieve real-time processing. The achieved processing rate of Tensorflow based SMART ODS modules run on SMART PC is 8 FPS that means SMART machine learning-based perception module is able to process in 125 ms. Referring to equation (7-1) in Section 7.1

$$t_{res} < t_{acq} \tag{7-5}$$

the processing rate should be larger than the data acquisition rate. In case of SMART ODS, the data acquisition rate is 7 Hz, however after data synchronization the data at 2 Hz are forwarded to processing unit where the SMART perception module is able to process at 8 Hz on SMART PC. The processing rate is four times the actual data acquisition rate. This shows that the algorithms are highly optimized to perform reliably in real-time environment and can perform on higher data acquisition rate as well.

As described in chapter 4, state-of-the-art object detection algorithm YOLO-You Only Look Once was chosen as object detector for SMART *DisNet*-based object detection and distance estimation (Figure 48). YOLO uses a single deep-learning network for both object classification and object localization in an image, and it is considered as real-time fast multi-object detection algorithm with higher accuracy rate.

The *DisNet*-based algorithm was developed for object detection and distance estimation from a monocular camera and can be applied to all three SMART camera types, RGB, Thermal and Night Vision camera. As described in Section 4, the results of obstacle detection from single-camera are satisfactory, but the results could be improved when performing the sensor fusion so that there is interest to process more than one camera image at the time. For the purpose of timing consideration, the calculation of total processing time when only one sensor (RGB camera) used is performed and compared to the total processing time when more than one sensor used, 2 (thermal+ RGB camera) and 5 (all 5 SMART vision sensors, 3 RGB, Thermal and Night Vision). The sensors' data acquisition times are given in Table 32 as well as in Table 33. The time performance table (Table 33) shows that SMART ODS satisfies the minimal requirement approximation. However, the time can be reduced more with the better-performing processing unit.

In Table 33, f refers to frequency and $t_{process}$ is the total time required by the acquisition module and perception module to provide an output in case of a single camera, whereas the data synchronization time is considered instead of data acquisition time in case of multiple cameras.

Table 33. Time performance

Module	Sensor Interface Module		Perception Module	Total Processing Time
Sub Module	Data Acquisition f_{acq}, t_{acq}	Data Synchronization f_{acq}', t_{acq}'	Object detection, tracking and distance estimation f_{res}, t_{res}	$f_{process}, t_{process}$
RGB Camera	15 Hz, 66.6 ms	-	8 Hz, 125 ms	5.21 Hz, 191.6 ms
RGB + Thermal Camera	9 Hz, 111 ms	5 Hz, 200 ms	6.5 Hz, 153.8 ms	2.82 Hz, 353.8 ms
All sensors	7 Hz, 142 ms	2 Hz, 500 ms	2.5 Hz, 400 ms	1.11 Hz, 900 ms

As evident from the time performance table, the total processing time is increasing gradually for cases where more than one camera is used in comparison to a single camera. The results of performance evaluation of SMART ODS (Section 4) show that using one camera at a time gives obstacle detection and distance estimation result that meets the requirements of mid- and long-range object detection (with up to ±10% error). Fusing with thermal camera processing results can lead to better performance (Section 5) while still enabling real-time processing (Table 33). However, for using more than two vision sensors at a time, it is needed to reduce processing time, which could be achieved with a processing unit of higher performances. Nevertheless, the SMART ODS meets the requirements of real-time by delivering the object detection and distance estimation results in a fraction of second.

8. Conclusion and Outlook

8.1 Conclusion

This thesis addresses the problem of long-range environmental perception for the applications where autonomous obstacle detection is safety-critical such as automated vehicles. The particular focus of the thesis is on autonomous obstacle detection for railways bearing in mind that long-range obstacle detection is explicitly required due to longer braking distances for trains. Following the traditional and state-of-the-art approaches for object detection in other applications, the first dataset for long-range obstacle detection and distance estimation (LRODD) was generated in this Thesis as described in chapter 3. The dataset contains images captured by monocular cameras including three RGB cameras set with three different focal lengths to cover the short, mid to long-range, a thermal camera and a night vision camera, short-range distance information from LiDAR and GPS for positioning of ODS. The images were recorded during various static and dynamic experiments conducted within project SMART and contain examples of real-world scenarios that a train driver usually faces every day including potential obstacles on the rail track or near to the rail track. The recorded images, containing potential obstacles, were manually labelled for object bounding boxes, object classes and related object ground truth distance, using an annotation tool to form a dataset LRODD. Further, the labelled dataset was used in the development of algorithms proposed in this thesis.

In chapter 4, the focus is on monocular camera-based distance estimation to the object imaged by the camera. Two different approaches to the estimation of the distance to the object using a single monocular camera have been presented. Both approaches show the potential of using a single camera to object distance estimation without the need for any camera parameters calibration. The first method proposed in chapter 3 is referred to as DisNet, which is an abbreviation for Distance Network, and it is based on a neural network which estimates the distance to the object based on the size of the object bounding box in the image. DisNet expects to receive an input, containing object bounding box and object class, from an object detection module in order to estimate the distance to the object. DisNet can work with any object detection module which produces the object bounding box and object class. DisNet is a single network that works for multiple object classes. However, in some cases, it shows some limitations to accurate distance estimation. For example, it tends to wrongly estimate the object distance when a false or unprecise bounding box, produced by object detection module inputs the DisNet, or objects of the same class appear in different sizes in the image which leads to the understanding to consider object at a different distance than the actual distance. In the same chapter, the second method named YOLO-D, which is derived from the state-of-the-art object detection module You Only Look Once (YOLO) and - *D* is added to represent distance estimation. YOLO is a well-known object detector that localises and classifies the objects in an image. In YOLO-D, the original YOLO architecture, loss function, and training methods were modified so that an additional output was added, which is distance estimation to the detected object. Due to the addition of another output, the original loss function was also modified to adapt to the changes in the network architecture. In comparison to original YOLO, the YOLO-D estimates the distance to the object in the image in addition to object localisation and classification.

Further, for the training of YOLO-D additional information is necessary that is ground truth distance to the object in a training image. That is why YOLO-D was trained in this thesis with novel dataset LRODD containing labelled objects and also the distance to them. Additionally, a transfer learning approach was applied to train YOLO-D further with another state-of-the-art dataset KITTI which also has distance information to the objects in order to improve the accuracy distance estimation by YOLO-D.

In comparison to DisNet, YOLO-D is a single end-to-end network that detects an object and estimates object distance and works with multiple object classes. Both proposed methods in chapter 4 were tested in real-time and real-world applications including railway and road scenarios.

In chapter 5, a machine learning-based sensor fusion method named Multi-DisNet has been proposed to estimate the distance to an object based on the object's appearance in the images captured from two cameras mounted apart from each other. The main principle of this method was inspired by the DisNet method. After the simultaneous object detection on images captured from both cameras, the size of the corresponding object bounding box of the same object in both images is feed to the neural network that estimates distance. However, only an object class 'Person' was investigated in the development of this method.

In chapter 6, the Recurrent Neural Network-based method of multiple object tracking has been presented. The RNN based network architecture tracks and predicts the position of the object in the frames where the object detection module fails to identify the object or the object is occluded. This method further estimates the distance to the object continuously. Additionally, this method also refines the object bounding box position and size based on the previous detection results in a current frame.

In chapter 7, the real-time implementation of the developed algorithms and capabilities to use these algorithms in the real-world application was investigated. The minimum hardware and software requirements for the obstacle detection system for freight trains were also studied considering the physical braking constraints.

8.2 Outlook

The proposed methods in this thesis focusing on long-range detection and distance estimation shows potential to overcome the limitation of commercial off-the-shelf sensors technology to measure long-range distances. The methods shows that distant objects can be detected and distance to them can be estimated by processing the high resolution image obtained from a single camera.

Although the results presented in this Thesis show the reliability of the autonomous multi-sensor long-range obstacle detection, tracking and distance estimation system, there are few open questions are future directions. These are summarized as follows.

One research question is how the information from the autonomous system will be communicated with the driver of the train. An intelligent Human-Computer Interaction (HCI) system will be needed, which will need to ensure that it does not distract the driver but also it is not ignored. Research and decades of commercial development in aviation, that has advanced the interaction between planes and pilots, could guide the development of a successful HCI system for trains.

As it was mentioned before, the developed obstacle detection and distance estimation system could also be applied for short-range detection, not only on autonomous cars but also on autonomous robots. In a laboratory setting, *DisNet* was adjusted to detect and estimate the position of household objects, such as cup and glass, and humans with very promising results [21]. Further research will be needed to enable the employment of DisNet in robotics.

Furthermore, YOLO-D shows potential to be use as a single neural network that can detect object and simultenoulsy estimate distance to it. The performance can be improve by further training with large annotated dataset, more classes and ground truth distance.

Bibliography

[1] Y. J. Li, Z. Zhang, D. Luo and G. Meng, "Multi-sensor environmental perception and information fusion for vehicle safety," in *IEEE International Conference on Information and Automation*, Lijiang, 2015.

[2] H. Nguyen and C. C. Kemp, "Bio-inspired assistive robotics: Service dogs as a model for human-robot interaction and mobile manipulation," in *2nd IEEE RAS & EMBS International Conference on Biomedical Robotics and Biomechatronics,*, Scottsdale, 2008.

[3] J.-K. Oh and C.-H. Lee, "Development of a stereo vision system for industrial robots," in *International Conference on Control, Automation and Systems*, Seoul, 2007.

[4] J. Foucault, S. Lesecq, G. Dudnik, M. Correvon, R. O'Keeffe, V. Di Palma, M. Passoni, F. Quaglia, L. Ouvry, S. Buckley, J. Herveg, A. di Matteo, T. Rakotovao, O. Debicki, N. Mareau, J. Barrett, S. Rea, A. McGibney, F. Birot and de Chaumont, "INSPEX: Optimize Range Sensors for Environment Perception as a Portable System.," *Sensors ,* vol. 19, p. 4350, October 2019.

[5] M. Bernas, B. Płaczek, W. Korski, P. Loska, J. Smyła and P. Szymała, "A Survey and Comparison of Low-Cost Sensing Technologies for Road Traffic Monitoring," *Sensors ,* vol. 18(10), p. 3243, September 2018.

[6] L. Nalpantidis and A. Gasteratos, "Stereo Vision Depth Estimation Methods for Robotic Applications," in *Depth Map and 3D Imaging Applications: Algorithms and Technologies*, IGI Global, 2011, pp. 397-417.

[7] A. Saxena, J. Schulte and A. Ng, "Depth Estimation Using Monocular and Stereo Cues.," in *IJCAI International Joint Conference on Artificial Intelligence*, 2007.

[8] R. Atienza, "Fast Disparity Estimation using Dense Networks," in *International Conference on Robotics and Automation (ICRA)*, Brisbane, 2018.

[9] M. Moukari, S. Picard, S. L. and F. Jurie, "Deep Multi-Scale Architectures for Monocular Depth Estimation," in *25th IEEE International Conference on Image Processing (ICIP)*, Athens, 2018.

[10] W. Maddern, G. Pascoe, C. Linegar and P. Newman, "1 Year, 1000km: The Oxford RobotCar Dataset," in *The International Journal of Robotics Research (IJRR)*, 2016.

[11] Shift2Rail, "Multi-Annual Action Plan," Brussels, 2015.

[12] J. Weichselbaum, C. Zinner, O. Gebauer and W. Pree, "Accurate 3D-vision-based obstacle detection for an autonomous train," *Computers in Industry,* vol. 64, p. 1209–1220, 2013.

[13] A. Berg, K. Oefjaell, J. Ahlberg and M. Felsberg, "Detecting Rails and Obstacles Using a Train-Mounted Thermal Camera," in *Lecture Notes in Computer Science, vol. 9127*, Springer, Cham, SCIA 2015, p. 492–503.

[14] P. Pinggera, U. Franke and R. Mester, "High-performance long range obstacle detection using stereo vision," in *IEEE/RSJ International Conference on Intelligent Robots and Systems (IROS)*, Hamburg , 2015.

[15] N. Fürstenau, Virtual and Remote Control Tower: Research, Design, Development and Validation, 2014.

[16] P. SMART, 07 2020. [Online]. Available: http://www.smartrail-automation-project.net.

[17] J. Brownlee, "A Gentle Introduction to Computer Vision," July 2019. [Online]. Available: https://machinelearningmastery.com/what-is-computer-vision/.

[18] S. Long, X. He and C. Yao, "Scene Text Detection and Recognition: The Deep Learning Era," *Computer Vision and Pattern Recognition,* November 2018.

[19] K. Bobkowska, A. Kaczyńska, A. Kosiński and M. Przyborski, "Digital Photogrammetry in the Analysis of the Ventricles' Shape and Size," in *Baltic Geodetic Congress (BGC Geomatics)*, Gdansk, 2017.

[20] W. Zhao, J. Y, Chang, D. M. Smith and M. D. Ginsberg, "Disparity analysis and its application to three-dimensional reconstruction of medical images," in *Proceedings Fifth Annual IEEE Symposium on Computer-Based Medical Systems*, NC, USA, 1992.

[21] M. Kyrarini, Q. Zheng, M. A. Haseeb and A. Gräser, "Robot Learning of Assistive Manipulation Tasks by Demonstration via Head Gesture-based Interface," in *IEEE 16th International Conference on Rehabilitation Robotics (ICORR)*, Toronto, ON, Canada, 2019.

[22] D. Howard , "Enhanced driver safety with advanced vision systems," in *Pan Pacific Microelectronics Symposium (Pan Pacific)*, Waimea, HI, 2018.

[23] G. Jianju, M. Kyrarini, M. A. Haseeb, D. Ristic-Durrant and A. Gräser, "Safety Surveillance System for Co-operative Robot using 360-Degree Camera," in *Conference: XIV International SAUM Conference on Systems, Automatic Control and Measurements*, Niš, Serbia, 2018.

[24] X. Li, X. Zhao, Y. Fu and Y. Liu, "Bimodal gender recognition from face and fingerprint," in *IEEE Computer Society Conference on Computer Vision and Pattern Recognition*, San Francisco, CA, 2010.

[25] M. Alom, T. Taha, C. Yakopcic, S. Westberg, P. Sidike, M. Nasrin, M. Hasan, B. Van Essen, A. Awwal and V. Asari, "A State-of-the-Art Survey on Deep Learning Theory and Architectures," *Electronics 2019,* vol. 8, p. 292, 2019.

[26] O. Campesato, Artificial Intelligence, Machine Learning, and Deep Learning, San Francisco, CA: Stylus Publishing, LLC, 2020.

[27] M. R. M. Talabis, I. Miyamoto and D. Kaye, Information Security Analytics, R. McPherson and J. L. Martin, Eds., Syngress, 2015.

[28] V. Roman, Jan 2019. [Online]. Available: https://towardsdatascience.com/supervised-learning-basics-of-classification-and-main-algorithms-c16b06806cd3.

[29] J. Brownlee, "Supervised and Unsupervised Machine Learning Algorithms," 16

March 2016. [Online]. Available: https://machinelearningmastery.com/supervised-and-unsupervised-machine-learning-algorithms/.

[30] J.-N. Vittaut, M.-R. Amini and P. Gallinari, "Learning Classification with Both Labeled and Unlabeled Data," in *Learning Classification with Both Labeled and Unlabeled Data*, 2002.

[31] A. Orhan E, "Computational Basis of Neural Elements," in *Artificial Neural Network for Drug Design, Delivery and Disposition*, Elsevier , 2016, pp. 29-82.

[32] G. Shenk, August 2019. [Online]. Available: https://www.functionize.com/blog/machine-learning-humans-behind-screen/.

[33] M. R. Tarabay, August 2020. [Online]. Available: http://rafietarabay.blogspot.com/2019/05/pytorch-and-deep-learning.html.

[34] J. Duchi, E. Hazan and Y. Singer, "A Survey of Optimization Methods from a Machine Learning Perspective," *Journal of Machine Learning Research,* vol. 12, p. 2121–2159, 2011.

[35] S. Raschka, August 2020. [Online]. Available: http://rasbt.github.io/mlxtend/user_guide/general_concepts/gradient-optimization/.

[36] A. Bhande, "What is underfitting and overfitting in machine learning and how to deal with it," July 2020. [Online]. Available: https://medium.com/greyatom/what-is-underfitting-and-overfitting-in-machine-learning-and-how-to-deal-with-it-6803a989c76.

[37] J. Bergstra and Y. Bengio, "Random Search for Hyper-Parameter Optimization," *Journal of Machine Learning Research,* vol. 13, pp. 281-305, 2012.

[38] E. Ndiaye, T. Le, O. Fercoq, J. Salmon and I. Takeuchi, "Safe Grid Search with Optimal Complexity," in *International Conference on Machine Learning*, 2019.

[39] J. Walsh, N. O' Mahony, S. Campbell, A. Carvalho, L. Krpalkova, G. Velasco-

Hernandez, S. Harapanahalli and D. Riordan, "Deep Learning vs. Traditional Computer Vision," in *Computer Vision Conference (CVC)*, Las Vegas, 2019.

[40] Z. Zhou, . N. V. Chawla, . Y. Jin and G. J. Williams, "Big Data Opportunities and Challenges: Discussions from Data Analytics Perspectives [Discussion Forum]," *IEEE Computational Intelligence Magazine,* vol. 9, no. 4, pp. 62-74, November 2014.

[41] H. D. Hlynsson, N. Alberto, B. Escalante and W. Laurenz, "Measuring the Data Efficiency of Deep Learning Methods," in *8th International Conference on Pattern Recognition Applications and Methods*, 2019.

[42] Y. LeCun, L. Bottou, Y. Bengio and P. Haffner, "Gradient-Based Learning Applied to Document Recognition," in *Proceedings of the IEEE*, 1998.

[43] A. R., Brodtkorb, T. R., Hagen, S. Christian and H. Geir, "GPU computing in discrete optimization. Part I: Introduction to the GPU," *EURO Journal on Transportation and Logistics,* vol. 2, p. 129–157, 2013.

[44] nvidia. [Online]. Available: https://www.nvidia.com/en-us/self-driving-cars/drive-platform/.

[45] Y. Liu, "Feature Extraction and Image Recognition with Convolutional Neural Networks," *Journal of Physics: Conference Series,* vol. 6, September 2018.

[46] A. Dertat, 02 2020. [Online]. Available: https://towardsdatascience.com/applied-deep-learning-part-4-convolutional-neural-networks-584bc134c1e2.

[47] "Convolutional Neural Networks (CNNs / ConvNets)," Stanford CS class, [Online]. Available: https://cs231n.github.io/convolutional-networks/.

[48] A. Krizhevsky, I. Sutskever and G. E. Hinton, "ImageNet Classification with Deep Convolutional Neural Networks," in *Neural Information Processing Systems*, 2012.

[49] M. D Zeiler and R. Fergus, "Visualizing and Understanding Convolutional Networks," 2013.

[50] K. Simonyan and A. Zisserman, "Very Deep Convolutional Networks for Large-Scale Image Recognition," 2014.

[51] C. Szegedy, W. Liu, Y. Jia, P. Sermanet, S. Reed, D. Anguelov, D. Erhan, V. Vanhoucke and Rabinovich, " Going deeper with convolutions," in *In Proceedings of the IEEE Conference on Computer Vision and Pattern Recognition*, Boston, MA, USA, 2015.

[52] K. He, X. Zhang, S. Ren and J. Sun, " Deep residual learning for image recognition," in *In Proceedings of the IEEE*, Las Vegas, NV, USA, 2016.

[53] J. Deng, W. Dong, R. Socher, L. Li, K. Li and L. Fei-Fei, "ImageNet: A Large-Scale Hierarchical Image Database," [Online]. Available: http://www.image-net.org/papers/imagenet_cvpr09.bib.

[54] X. Han, Y. Zhong, L. Cao and L. Zhang, "Pre-Trained AlexNet Architecture with Pyramid Pooling and Supervision for High Spatial Resolution Remote Sensing Image Scene Classification," *Remote Sens,* vol. 9, 2017.

[55] G. Huang, Z. Liu, L. Van Der Maaten and K. Weinberger, "Densely connected convolutional networks," in *In Proceedings of the IEEE conference on computer vision and pattern recognition* , 2017.

[56] G. Larsson, M. Maire and G. Shakhnarovich, "Fractalnet: Ultra-deep neural networks without residuals," in *arXiv preprint arXiv:1605.07648*, 2016.

[57] S. Sabour, N. Frosst and G. Hinton, "Dynamic routing between capsules," in *Advances in neural information processing systems* , 2017.

[58] K. Zhang, W. Zuo, S. Gu and L. Zhang, "earning deep CNN denoiser prior for image restoration," in *Proceedings of the IEEE conference on computer vision and pattern recognition*, 2017.

[59] M. Alom, M. Hasan, C. Yakopcic, T. Taha and V. Asari, "Improved inception-residual convolutional neural network for object recognition," *Neural Computing and Applications,* vol. 32, no. 1, pp. 279-293, 2020.

[60] S. Gao, Z. Miao, Q. Zhang and Q. Li, "DCRN: Densely Connected Refinement

Network for Object Detection," *Journal of Physics: Conference Series,* vol. 1129, no. 1, 2019.

[61] J. Long, E. Shelhamer and T. Darrell, "Fully convolutional networks for semantic segmentation," in *In Proceedings of the IEEE Conference on Computer Vision and Pattern Recognition*, Boston, MA, USA, 2015.

[62] V. Badrinarayanan, A. Kendall and R. Cipolla, "SegNet: A Deep Convolutional Encoder-Decoder Architecture for Image Segmentation," *IEEE Transactions on Pattern Analysis and Machine Intelligence,* vol. 39, no. 12, pp. 2481-2495, December 2017.

[63] G. Lin, A. Milan, C. Shen and I. Reid, "Refinenet: Multi-path refinement networks for high-resolution semantic segmentation," in *In Proceedings of the 2017 IEEE Conference on Computer Vision and Pattern Recognition CVPR*, , Honolulu, HI, USA, 2017.

[64] H. Zhao, J. Shi, X. Qi, X. Wang and J. Jia, "Pyramid scene parsing network," in *In Proceedings of the IEEE Conference on Computer Vision and Pattern Recognition (CVPR)*, Honolulu, HI, USA, 2017.

[65] L. Chen, G. Papandreou, I. Kokkinos, K. Murphy and A. Yuille, "Deeplab: Semantic image segmentation with deep convolutional nets, atrous convolution, and fully connected," in *IEEE Trans. Pattern Anal. Mach. Intell.*, 2018.

[66] R. Girshick, J. Donahue, T. Darrell and J. Malik, " Rich feature hierarchies for accurate object detection and," in *In Proceedings of the IEEE Conference on Computer Vision and Pattern Recognition CVPR*, Columbus, OH, USA, 2014.

[67] T.-Y. Lin, P. Goyal, R. Girshick, K. He and P. Dollár, "Focal Loss for Dense Object Detection," in *Computer Vision and Pattern Recognition (CVPR)*, 2018.

[68] R. Girshick, "Fast R-CNN," in *International Conference on Computer Vision (ICCV)*, 2015.

[69] K. He, G. Gkioxari, P. Dollár and R. Girshick, "Mask R-CNN," in *IEEE International Conference on Computer Vision (ICCV)*, Venice, 2017.

[70] J. Redmon, S. Divvala, . R. Girshick and A. Farhadi, "You Only Look Once: Unified, Real-Time Object Detection," in *IEEE Conference on Computer Vision and Pattern Recognition (CVPR)*, Las Vegas, NV, 2016.

[71] W. Liu, D. Anguelov, D. Erhan, C. Szegedy, S. Reed, C.-Y. Fu and A. C. Berg, "SSD: Single Shot MultiBox Detector," *Lecture Notes in Computer Science, Springer International Publishing,* p. 21–37, 2016.

[72] P. Viola and M. Jones, "Rapid Object Detection Using a Boosted Cascade of Simple Features," in *IEEE Computer Society Conference on Computer Vision and Pattern Recognition. CVPR* , Kauai, HI, USA, 2001.

[73] D. Lowe, "Distinctive image features from scale-invariant keypoints," *International Journal of Computer Vision,* vol. 60, p. 91–110, 2004.

[74] H. Bay, T. Tuytelaars and L. Van Gool, "Surf: Speeded up robust features," in *In European Conference on Computer Vision, Springer* , Berlin, Germany, 2006.

[75] K. Mikolajczyk and C. Schmid, "A Performance Evaluation of Local Descriptors," *IEEE TRANSACTIONS ON PATTERN ANALYSIS AND MACHINE INTELLIGENCE,* vol. 27, no. 19, pp. 1615-1630, October 2005.

[76] N. Dalal and B. Triggs, "Histograms of Oriented Gradients for Human Detection," in *In Proceedings of the IEEE Conference on Computer Vision and Pattern Recognition*, San Diego, CA, USA, 2005.

[77] J. Redmon and A. Farhadi, "YOLO9000: Better, Faster, Stronger," in *IEEE Conference on Computer Vision and Pattern Recognition (CVPR)*, Honolulu, HI, 2017.

[78] J. Redmon and A. Farhadi, "YOLOv3: An Incremental Improvement," in *ArXiv abs/1804.02767*, 2018.

[79] R. Girshick, "Fast R-CNN," in *IEEE International Conference on Computer Vision (ICCV)*, Santiago, 2015.

[80] J. Hui, August 2019. [Online]. Available:

https://medium.com/@jonathan_hui/real-time-object-detection-with-yolo-yolov2-28b1b93e2088..

[81] L. Van Gool and A. Neubeck, "Efficient Non-Maximum Suppression," in *18th International Conference on Pattern Recognition*, Hong Kong, 2006.

[82] J. Redmon. [Online]. Available: http://pjreddie.com/darknet/, 2013{2016.

[83] N. Developer, August 2020. [Online]. Available: https://developer.nvidia.com/about-cuda.

[84] August 2020. [Online]. Available: https://github.com/Cartucho/mAP.

[85] M. E. Aidouni, October 2019. [Online]. Available: https://manalelaidouni.github.io/manalelaidouni.github.io/Evaluating-Object-Detection-Models-Guide-to-Performance-Metrics.html.

[86] M. Johnson, "How much data is enough? Predicting how accuracy varies with training data size," 2017.

[87] H. Caesar, V. Bankiti, A. Lang, S. Vora, V. Liong, Q. Xu, A. Krishnan, Y. Pan, G. Baldan and O. Beijbom, "nuScenes: A multimodal dataset for autonomous driving," in *Proceedings of the IEEE/CVF Conference on Computer Vision and Pattern Recognition*, 2020.

[88] A. Patil, S. Malla, H. Gang and Y. Chen, "The H3D Dataset for Full-Surround 3D Multi-Object Detection and tracking in crowded urban scenes," in *2019 International Conference on Robotics and Automation (ICRA)*, 2019.

[89] T. Lin, M. Maire, S. Belongie, J. Hays, P. Perona, D. Ramanan, P. Dollár and C. Zitnick, "Microsoft COCO: Common Objects in Context," *ECCV 2014, Lecture Notes in Computer Science,* vol. 8693, 2014.

[90] A. Geiger, P. Lenz and R. Urtasun, "Are we ready for autonomous driving? The KITTI vision benchmark suite,," in *IEEE Conference on Computer Vision and Pattern Recognition*, Providence, RI, 2012.

[91] A. Kashani, M. Olsen, C. Parrish and N. Wilson, "A Review of LIDAR

Radiometric Processing: From Ad Hoc Intensity Correction to Rigorous Radiometric Calibration," *Sensors ,* vol. 15, pp. 28099-28128, 2015.

[92] J. Hecht, "Lasers for Lidar: FMCW lidar: An alternative for self-driving cars," 2019.

[93] Y. Wang, C. Peng, A. Ravankar and A. Ravankar, "A single LiDAR-based feature fusion indoor localization algorithm," *Sensors,* vol. 18, no. 4, p. 1294, 2018.

[94] T. Gee, J. James, W. Van Der Mark, P. Delmas and G. Gimel'farb, "Lidar guided stereo simultaneous localization and mapping (SLAM) for UAV outdoor 3-D scene reconstruction," in *2016 International Conference on Image and Vision Computing New Zealand (IVCNZ)*, 2016.

[95] B. Schwarz, "Mapping the world in 3D," *Nature Photonics,* vol. 4, no. 7, pp. 429-430, 2010.

[96] W. Ali, S. Abdelkarim, M. Zidan, M. Zahran and A. El Sallab, "Yolo3d: End-to-end real-time 3d oriented object bounding box detection from lidar point cloud," in *Proceedings of the European Conference on Computer Vision (ECCV)*, 2018.

[97] D. Ristić-Durrant, G. Gao and A. Leu, "Facta Universitatis, Series: Automatic Control and Robotics," *Low-level sensor fusion-based human tracking for mobile robot,* vol. 1, no. 1, pp. 17-32, 2016.

[98] J. Hecht, "Lidar for self-driving cars," *Optics and Photonics News,* vol. 29, no. 1, pp. 26-33, 2018.

[99] N. Qian, "Binocular disparity and the perception of depth," *Neuron,* vol. 18, no. 3, pp. 359-368, 1997.

[100] L. Matthies, R. Szeliski and T. Kanade, "Incremental estimation of dense depth maps from image sequences," in *CVPR*, 1988.

[101] N. Short, "3-D Point Cloud Generation from Rigid and Flexible Stereo Vision Systems," 2020.

[102] M. Bertozz, A. Broggi and A. Fascioli, "Stereo inverse perspective mapping: theory and applications," *Image and vision computing,* vol. 16, no. 8, pp. 585-590, 1998.

[103] J. Zhu and e. al, "Learning Object-specific Distance from a Monocular Image," in *International Conference on Computer Vision (ICCV)*, Seoul, Korea, 2019.

[104] Z. Sadreddini, T. Çavdar and H. Jond, "A distance measurement method using single camera for indoor environments," in *2016 39th International Conference on Telecommunications and Signal Processing (TSP)*, 2016.

[105] A. Ali, A. Hassan, A. Ali, H. Khan, W. Kazmi and A. Zaheer, "Real-time vehicle distance estimation using single view geometry," in *The IEEE Winter Conference on Applications of Computer Vision*, 2020.

[106] "Lyft Level 5 Dataset," [Online]. Available: https://self-driving.lyft.com/level5/data/.

[107] J. Xiao, J. Hays, K. A. Ehinger, A. Oliva and A. Torralba, "SUN database: Large-scale scene recognition from abbey to zoo," in *IEEE Computer Society Conference on Computer Vision and Pattern Recognition*, San Francisco, CA, 2010.

[108] M. Everingham, S. Eslami, L. Van Gool, C. Williams, J. Winn and A. Zisserman, "The PASCAL Visual Object Classes Challenge: A Retrospective," in *International Journal of Computer Vision*, 2015.

[109] O. Russakovsky, J. Deng, H. Su, J. Krause, S. Satheesh, S. Ma, Z. Huang, A. Karpathy, A. Khosla, M. Bernstein and A. Berg, "Imagenet large scale visual recognition challenge," *International Journal of Computer Vision,* vol. 115, pp. 211-252, 2015.

[110] P. Dollár, C. Wojek, B. Schiele and P. Perona, "Pedestrian Detection: A Benchmark," in *IEEE Conference on Computer Vision and Pattern Recognition*, Miami, FL, 2009.

[111] S. Ren, K. He, R. Girshick and J. Sun, "Faster r-cnn: Towards real-time object

detection with region proposal networks," *IEEE Transactions on Pattern Analysis and Machine Intelligence,* vol. 39, no. 6, pp. 1137-1149, June 2017.

[112] Y. Li, H. Qi, J. Dai, X. Ji and Y. Wei, "Fully Convolutional Instance-Aware Semantic Segmentation," in *IEEE Conference on Computer Vision and Pattern Recognition (CVPR)*, 2017.

[113] "The Imaging Source Europe GmbH," July 2020. [Online]. Available: https://www.theimagingsource.com/products/zoom-autofocus-cameras/gige-color-zoom-cameras/dfkz12gp031/.

[114] F. Systems, July 2020. [Online]. Available: https://www.flir.com/products/tau-2/.

[115] D. Ristić-Durrant, M. A. Haseeb, M. Banić and I. Ćirić, "D1.1 Obstacle Detection System Requirements and Specification," Bremen, 2019.

[116] M. A. H. M. B. a. D. R. Danijela Ristić-Durrant, "D2.1 - Report on selected sensors for multi-sensory system for obstacle detection," Bremen, 2017.

[117] "3D LiDAR sensors LD-MRS / LD-MRS 4-Layer / Outdoor," SICK, [Online]. Available: https://www.sick.com/ag/en/detection-and-ranging-solutions/3d-lidar-sensors/ld-mrs/ld-mrs400001s01/p/p251942.

[118] "USB GPS Module," [Online]. Available: https://www.hardkernel.com/shop/usb-gps-module/.

[119] "SMART - Smart Automation of Rail Transport," [Online]. Available: http://www.smartrail-automation-project.net/.

[120] M. Haseeb, D. Ristic-Durrant, A. Gräser, B. M. and S. D., "Multi-DisNet: Machine Learning-Based Object Distance Estimation from Multiple Cameras," in *International Conference on Computer Vision Systems*, 2019.

[121] M. Quigley, K. Conley, B. Gerkey, J. Faust, T. Foote, J. Leibs, R. Wheeler and A. Ng, "ROS: an open-source Robot Operating System," in *ICRA workshop on open source software*, 2009.

[122] "Approximate Time," ROS, [Online]. Available: http://wiki.ros.org/message_filters/ApproximateTime.

[123] B. Russell, A. Torralba, K. Murphy and W. Freeman, "LabelMe: a database and web-based tool for image annotation," *International journal of computer vision,* vol. 77, no. 1-3, pp. 157-173, 2008.

[124] M. Haseeb, J. Guan, D. Ristic-Durrant and A. Gräser, "Disnet: A novel method for distance estimation from monocular camera," in *10th Planning, Perception and Navigation for Intelligent Vehicles (PPNIV18), IROS*, 2018.

[125] M. Haseeb, D. Ristić-Durrant and A. Gräser, "Long-range obstacle detection from a monocular camera," in *ACM Computer Science in Cars Symposium (CSCS 2018), ECCV*, 2018.

[126] "Tuning the hyper-parameters of an estimator," scikit learn, [Online]. Available: https://scikit-learn.org/stable/modules/grid_search.html#grid-search.

[127] D. Kingma and J. Ba, "Adam: A method for stochastic optimization," in *arXiv preprint arXiv:1412.6980*, 2014.

[128] T. Tieleman and G. Hinton, "Lecture 6.5-rmsprop, coursera: Neural networks for machine learning," University of Toronto, Technical Report, 2012.

[129] "Layer weight initializers," Keras, [Online]. Available: https://keras.io/api/layers/initializers/.

[130] S. Chatterjee and A. Hadi, Regression analysis by example, John Wiley & Sons, 2015.

[131] R. Tibshirani, "Regression shrinkage and selection via the lasso," *Journal of the Royal Statistical Society: Series B (Methodological),* vol. 58, no. 1, pp. 267-288, 1996.

[132] J. Wang, A. Hertzmann and D. Fleet, "Gaussian process dynamical models," *Advances in neural information processing systems,* pp. 1441-1448, 2006.

[133] J. Suykens and J. Vandewalle, "Least squares support vector machine

classifiers," *Neural processing letters,* vol. 9, no. 3, pp. 293-300, 1999.

[134] D. Lee, J. In and S. Lee, "Standard deviation and standard error of the mean," *Korean journal of anesthesiology,* vol. 68, no. 3, p. 220, 2015.

[135] A. Leu, D. Aiteanu and A. Gräser, "High speed stereo vision based automotive collision warning system," *Applied Computational Intelligence in Engineering and Information Technology,* pp. 187-199, 2012.

[136] A. Leu, D. Bacără, D. Aiteanu and A. Gräser, "Hardware acceleration of image processing algorithms for collision warning in automotive applications," in *Methods and Applications in Automation: 32nd – 33rd Colloquium of Automation*, Salzhausen/Leer, Germany, 2012.

[137] August 2020. [Online]. Available: https://www.itread01.com/content/1541167345.html.

[138] Z. E. and Z. Y., "Average Precision," *Encyclopedia of Database Systems,* 2009.

[139] A. Dutta and A. Zisserman, "The VIA annotation software for images, audio and video," in *Proceedings of the 27th ACM International Conference on Multimedia*, 2019.

[140] F. Pedregosa, G. Varoquaux, A. Gramfort, V. Michel, B. Thirion, O. Grisel, M. Blondel, P. Prettenhofer, R. Weiss, V. Dubourg, J. Vanderplas, A. Passos, D. Cournapeau, M. Brucher, P. M. and E. Duchesnay, "Scikit-learn: Machine Learning in Python," *Journal of Machine Learning, Research,* 2011.

[141] D. Ristić-Durrant, M. A. Haseeb, M. Banić, S. D., S. M., Ć. I., N.-k. V., N. D. and R. D., "SMART: a novel on-board integrated multi-sensor long-range obstacle detection system for railways," in *RAILCON*, 2018.

[142] L. Duvieubourg, F. Cabestaing, S. Ambellouis and P. Bonnet, "Long distance vision sensor for driver assistance," *IFAC Proceedings Volumes,* vol. 40, no. 15, pp. 330-336, 2007.

[143] "Shift2Rail Joint Undertaking, Multi-Annual Action Plan," Brussels, 2015.

[144] Y. Zhang, Y. Huang and L. Wang, "Multi-task deep learning for fast online multiple object tracking," in *2017 4th IAPR Asian Conference on Pattern Recognition (ACPR)*, 2017.

[145] A. Kuramoto, M. Aldibaja, R. Yanase, J. Kameyama, K. Yoneda and N. Suganuma, "Mono-camera based 3d object tracking strategy for autonomous vehicles," in *2018 IEEE Intelligent Vehicles Symposium (IV)*, 2018.

[146] Y. Huang, T. Huang and H. Niemann, "A region-based method for model-free object tracking," in *Object recognition supported by user interaction for service robots*, 2002.

[147] H. Cho, S. Song, J. Kim and J. Cho, "Simple object coordination tracking based on background modeling," in *2015 Signal Processing: Algorithms, Architectures, Arrangements, and Applications (SPA)*, 2015.

[148] M. Yokoyama and T. Poggio, "A contour-based moving object detection and tracking," in *Visual Surveillance and Performance Evaluation of Tracking and Surveillance*, 2005.

[149] L. Fan, "A feature-based object tracking method using online template switching and feature adaptation," in *2011 Sixth International Conference on Image and Graphics*, 2011.

[150] H. Hsu and J. Ding, "FasterMDNet: Learning model adaptation by RNN in tracking-by-detection based visual tracking," in *2017 Asia-Pacific Signal and Information Processing Association Annual Summit and Conference (APSIPA ASC)* , 2017.

[151] M. Haseeb, D. Ristić-Durrant and A. Gräser, " A deep learning based autonomous distance estimation and tracking of multiple objects for improvement in safety and security in railways," in *BMVC 2019 workshop on Object Detection and Recognition for Security Screening (ODRSS2019)*, Cardiff, 2019.

[152] "The imaging Source - Technology based on standards," [Online]. Available:

https://www.theimagingsource.com/.

[153] D. Barney, D. Haley and G. Nikandros, "Calculating train braking distance," in *Conferences in Research and Practice in Information Technology Series*, 2001.

[154] "10-Gigabit Smart Managed Pro Switch Series," [Online]. Available: https://www.netgear.com/business/products/switches/smart/XS708T.aspx.

[155] S. Cousins, "Welcome to ros topics [ros topics]," *IEEE Robotics & Automation Magazine,* vol. 17, no. 1, pp. 13-14, 2010.

[156] S. Pendleton, H. Andersen, X. Du, X. Shen, M. Meghjani, Y. Eng, D. Rus and M. Ang, "Perception, Planning, Control, and Coordination for Autonomous Vehicles," *Machines ,* vol. 6, no. Mechatronics: Intelligent Machines, 2017.

[157] A. Geiger, P. Lenz, C. Stille and R. Urtasun, "Vision meets robotics: the KITTI dataset," *The International Journal of Robotics Research,* vol. 32, pp. 1231-1237, 2013.

[158] J. Hui, "Real-time Object Detection with YOLO, YOLOv2 and now YOLOv3," 17 March 2018. [Online]. Available: https://medium.com/@jonathan_hui/real-time-object-detection-with-yolo-yolov2-28b1b93e2088.

[159] "Choosing a Convolutional Neural Network Architecture for Real-Time Object Tracking (Part 1)," 1 December 2017. [Online]. Available: https://blog.kickview.com/choosing-a-convolutional-neural-network-architecture-for-real-time-object-tracking-part-1/.

[160] A. Rosebrock, "Intersection over Union (IoU) for object detection," 7 November 2016. [Online]. Available: https://www.pyimagesearch.com/2016/11/07/intersection-over-union-iou-for-object-detection/.

[161] Y. Liu, "The Confusing Metrics of AP and mAP for Object Detection / Instance Segmentation," 25 October 2018. [Online]. Available: https://medium.com/@yanfengliux/the-confusing-metrics-of-ap-and-map-for-object-detection-3113ba0386ef.

[162] J. Hui, "mAP (mean Average Precision) for Object Detection," 6 March 2018. [Online]. Available: https://medium.com/@jonathan_hui/map-mean-average-precision-for-object-detection-45c121a31173.

[163] "Most popular metrics used to evaluate object detection algorithms," Python Awesome, 21 July 2018. [Online]. Available: https://pythonawesome.com/most-popular-metrics-used-to-evaluate-object-detection-algorithms/.

[164] A. Geiger, P. Lenz, C. Stiller and R. Urtasun, "Vision meets robotics: The kitti dataset," *International Journal of Robotics Research,* vol. 32, no. 11, pp. 1231-1237, 2013.

Appendix A: Publications by the author

This appendix lists the publications by the author, which have been produced throughout this thesis, and they are the basis of this thesis.

Related Publications to the PhD thesis

[1] Ristic-Durrant, D., **Haseeb, M.A.,** Franke, M., Banić, M., Simonović, M. and Stamenković, D., 2020. Artificial intelligence for obstacle detection in railways: Project SMART and beyond. In *1st International Workshop on Artificial Intelligence for RAILwayS (AI4RAILS), Dependable Computing - EDCC 2020 Workshops, Springer,* Munich, Germany

[2] **Haseeb, M.A.,** Ristic-Durrant, D., Gräser, A., Banić M. and Stamenković D., 2019. Multi-DisNet: Machine Learning-Based Object Distance Estimation from Multiple Cameras. In *International Conference on Computer Vision Systems (ICCV)*, pp. 457-469. Springer, Cham., Thessaloniki*,* Greece*,* doi: 10.1007/978-3-030-34995-0_41

[3] **Haseeb, M.A.,** Ristic-Durrant, D., Gräser, A., 2019. A deep learning based autonomous distance estimation and tracking of multiple objects for improvement in safety and security in railways. In *British Machine Vision Conference (BMVC) - Workshop on Object Detection and Recognition for Security Screening (ODRSS2019),* Cardiff, UK

[4] **Haseeb, M.A.,** Guan, J., Ristic-Durrant, D. and Gräser, A., 2018. Disnet: A novel method for distance estimation from monocular camera. *10th Planning, Perception and Navigation for Intelligent Vehicles (PPNIV18), IROS, Madrid, Spain.*

[5] **Haseeb, M.A.**, Ristić-Durrant, D. and Gräser, A., 2018. Long-range obstacle detection from a monocular camera. In *ACM Computer Science in Cars Symposium (CSCS 2018), ECCV,* Munich, Germany

[6] Ristić-Durrant, D., **Haseeb, M.A.**, Emami, D., Gräser, A., 2018. Multimodal Sensor Fusion for Reliable Detection of Obstacles on Railway Tracks. *Journal of Mechatronics, Automation and Identification Technology*, 3(2), pp. 1-7, Novi Sad, Serbia

[7] Ristić-Durrant, D., **Haseeb, M.A.**, Banić M., Stamenković, D., Ćirić, I., Simonović, M., Nikolić, V., Nikolić, D. and Radovanović, D., 2018. SMART:

a novel on-board integrated multi-sensor long-range obstacle detection system for railways. *RAILCON*, Nis, Serbia.

[8] Ristić-Durrant, D., **Haseeb M. A.**, Emami, D., Gräser A., 2018, SMART concept of an integrated multi-sensory on-board system for obstacle recognition in *7th Transport Research Arena (TRA)* , Vienna, Austria

[9] Ristić-Durrant, D., **Haseeb, M.A.**, Emami, D., Gräser, A., Ćirić, I., Simonović, M., Nikolić, V., Nikolić, D., Eßer, F.P., Schindler, C., 2017. Reliable Obstacle Detection for Smart Automation of Rail Transport. In *1st International Railway Symposium Aachen (IRSA),* Aachen, Germany. doi: 10.18154/RWTH-2018-222952

Other Publications

[1] Kyrarini M., **Haseeb M.A.**, Ristić-Durrant D., Gräser A., 2019. Robot Learning of Industrial Assembly Task via Human Demonstrations. *Autonomous Robots*, 43(1), pp. 239-257. doi: 10.1007/s10514-018-9725-6

[2] Kyrarini M., Zheng Q., **Haseeb M.A,** Gräser A., 2019. Robot Learning of Assistive Manipulation Tasks by Demonstration via Head Gesture-based Interface. In *International Conference on Rehabilitation Robotics (ICORR)*, Toronto, Canada, pp.210-216. IEEE. doi: 10.1109/ICORR.2019.8779521

[3] **Haseeb M.A,** Kyrarini M., Jiang S., Ristić-Durrant D., Gräser A., 2018. Head Gesture-based Control for Assistive Robots. In *11th ACM International Conference on Pervasive Technologies Related to Assistive Environments (PETRA)*, Corfu Greece, pp. 379-383. ACM. doi: 10.1145/3197768.3201574

[4] Guan J., Kyrarini M., **Haseeb M.A,** Ristić-Durrant D., Gräser A., 2018. Safety Surveillance System for Co-operative Robot using 360-Degree Camera. In *XIV International SAUM Conference on Systems, Automatic Control and Measurements*, Niš, Serbia

[5] Kyrarini M., **Haseeb M.A.**, Ristić-Durrant D., Gräser A., 2017. Robot Learning of Object Manipulation Task Actions from Human Demonstrations. *Facta Universitatis, series: Mechanical Engineering (FU Mech Eng)*, 15(2), pp. 217-229. doi: 10.22190/FUME170515010K

Abbreviations

ANN	Artificial Neural Network
CNN	Convolutional Neural Network
DisNet	Distance Network
DisNet-RNN-Tracker	Distance Network and Reccurent Neural Network based object Tracker
DL	Deep Learning
GRU	Gated Recurrent Unit
LRODD	Long-Range Obstacle Detection and Distance Estimation Dataset
LSTM	Long Short-Term Memory
MAE	Mean Absolute Error
ML	Machine Learning
MOM	Multiple Object Mapping
MSE	Mean Square Error
Multi-DisNet	Multiple cameras – Distance Network
ODS	Obstacle Detection System
RGB	Red-Green-Blue
RMSE	Root Mean Square Error
RNN	Recurrent Neural Network
RTS	Real Time Systems
YOLO	You Only Look Once
YOLO-D	You Only Look Once – Distance Estimation

Table of Figures